공학박사학위논문

# Formation of Tyrosine Mediated 2D Peptide Nano-micro Structures and Their Catalytic Applications in Cross Coupling Reactions

타이로신 기반의 2차원 나노/마이크로 구조체의 형성
및 교차 짝지음 반응 촉매로의 응용

2013년 8월

서울대학교 대학원

화학생물공학부

장 형 석

타이로신 기반의 2차원 나노/마이크로 구조체의 형성 및 교차

짝지음 반응 촉매로의 응용


Formation of Tyrosine Mediated 2D Peptide Nano/micro Structures and
Their Catalytic Applications in Cross Coupling Reactions


지도 교수: 이 윤 식


이 논문을 공학박사 학위논문으로 제출함
2013년 8월


서울대학교 대학원
화학생물공학부
장 형 석


장형석의 공학박사 학위논문을 인준함
2013년 8월


위 원 장 _____ (인)

부위원장 _____ (인)

위     원 _____ (인)

위     원 _____ (인)

위     원 _____ (인)

`

# Abstract

# Formation of Tyrosine Mediated 2D Peptide Nano-micro Structures and Their Catalytic Applications in Cross Coupling Reactions

Hyung-Seok Jang

School of Chemical and Biological Engineering

The Graduate School

Seoul National University

Proteins and peptides are easy to form complex functional systems or self-assembly of monomeric units by multiple non-covalent interactions. They fold into specific three-dimensional structures by specific sequences of amino acids. Tyrosine is one of the most significant amino acids, which can store the mechanical energy by protein folding and also facilitate proton-mediated electron transport in photosystem II. In two-dimensional (2D) interfacial assembly, there is interplay between molecular ordering and interface geometry, which determines the final morphology and order of an entire system. In this thesis, an interfacial phenomenon of spontaneous facet formation of a water droplet driven by designed peptide assembly is presented. The identified peptides can flatten the rounded top of a hemispherical droplet into a plane by forming a macroscopic 2D crystal structure. Such ordering is driven by the amphiphilicity of the peptide, π-π interactions of tyrosine and cross-linked stabilization by cysteine. In addition, by tuning the peptide sequence, a wrinkled form with multi-faceted and single-faceted interfaces was provided by guiding differently oriented π-π interactions. The key sequence motifs were discovered and their sequence-specific assembly was studied. The well-ordered, densely packed, redox active tyrosine units in the YYACAYY film can trigger or enhance chemical/electrochemical reaction, and can potentially serve as a platform to fabricate a molecularly

`

tunable, self-repairable, flat peptide or metal hybrid film of a large length (>100 cm$^2$). The tyrosine based peptide film can serve as a redox active scaffold for developing an enzyme mimetic catalyst. From the results of oxidative pyrrole polymerization on tyrosine peptide film, we propose the tyrosine radicals (Tyr●) can be easily generated in our peptide film and able to trigger or enhance the chemical reaction in a manner similar to that observed for many other biological systems such as ribonucleotide reductase and galactose oxidase. We have found that tyrosine peptide film can induce the palladium nanoparticle formation on tyrosine peptide-polypyrrole hybrid, which is easily formed on tyrosine peptide film by polymerization of pyrrole. Finally, this tyrosine peptide-polypyrrole supported palladium catalysts (Tyr Peptide@PPy@Pd catalysts) have good catalytic acitivy on C-C cross-coupling reaction in water. Even aryl chlorides which are much difficult to be coupled than aryl iodides and bromides can proceed C-C cross-coupling reaction by Tyr Peptide@PPy@Pd catalyst in high yield and they can be reusable more than five times.

`

# Contents

## 1. Introduction

## 2. Experimental Section

## 3.  Results and Discussion

`

`

# List of Figures

`

`

`

## List of Tables

# 1. Introduction

## 1.1. Protein Based Self-assembly for Nano Structures

Biomimetic self-assembly is a spontaneous process and reversible organization of disordered system of biological moleculars into ordered structure by non-covalent interactions without external forces. Protein assembly offers a powerful approach for designing and fabricating versatile supramolecular architectures, and detailed understanding of biological concepts and three-demensional arrangement of protein segments are playing a crucial roles[1,2]. For example, well-defined nano structures are prepared by biomineralization of spherical viruses[3](Fig. 1), cage like proteins[4-6] and closely packed photosystem I protein[7,8]. Amyloid proteins such as huntingtin, amyloid β protein (Aβ), α-synuclein, and prion protein are related to Huntington's, Alzheimer's, Parkinson's, and Creutzfeldt-Jakob diseases (Fig. 1b). These bio-stable amyloid fibrils are produced via a process called 'amyloidogenesis' that soluble proteins turn to insoluble protein aggregates in highly ordered structure of β-sheet conformation[9-14]. Despite of their diverse and structurally different amyloidogenic proteins, all amyloid fibrils share similar biophysical/chemical properties including specific interaction of dyes such as thioflavin-T and congo red for β-sheet structures[9,15-17]. On the basis of experiments and theory, common molecular mechanism for amyloid formation can be expected while the proteins are distinctive from each other at their monomeric units (Fig. 2).

1
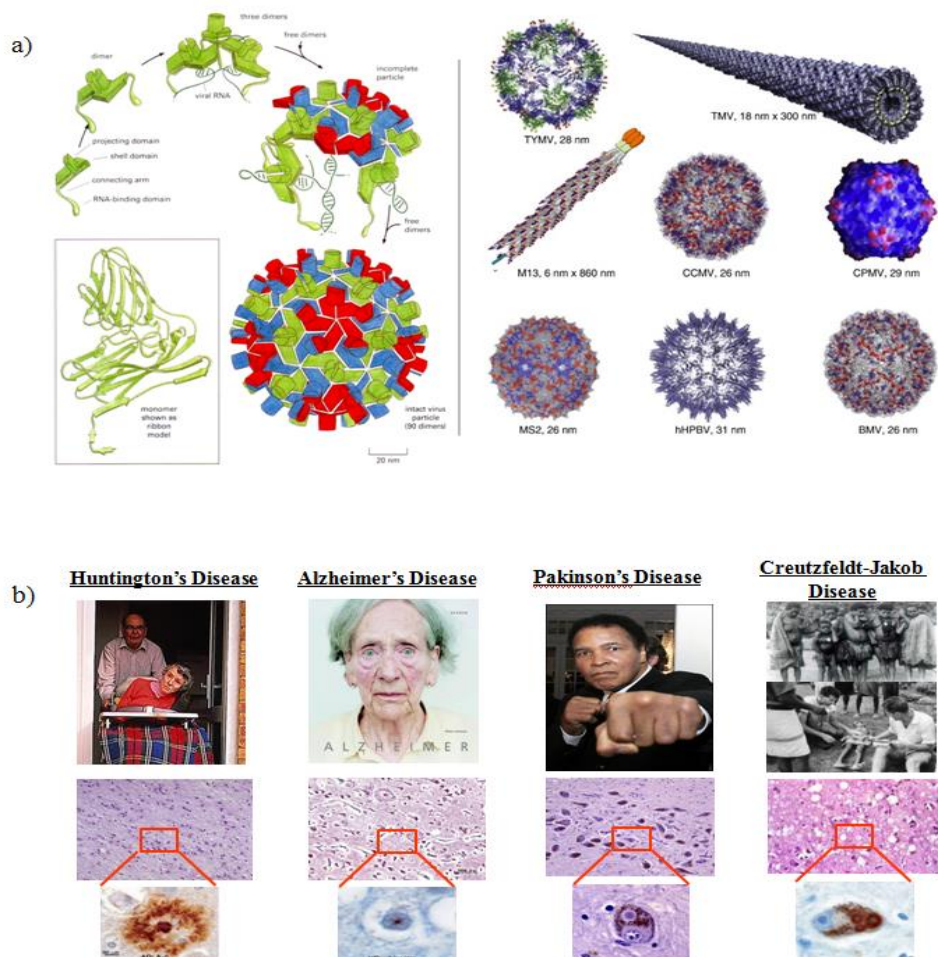
**Figure 1. Self-assembly of various proteins into nano structures**[1-14]**.** a) Turnip yellow mosaic virus (TYMV), tobacco mosaic virus (TMV), M13 bacteriophage (M13), cowpea chlorotic mosaic virus (CCMV), cowpea mosaic virus (CPMV), MS2 bacteriophage (MS2), human hepatitis B virus (hHPBV), b) Amyloid related diseases and protein aggregates.
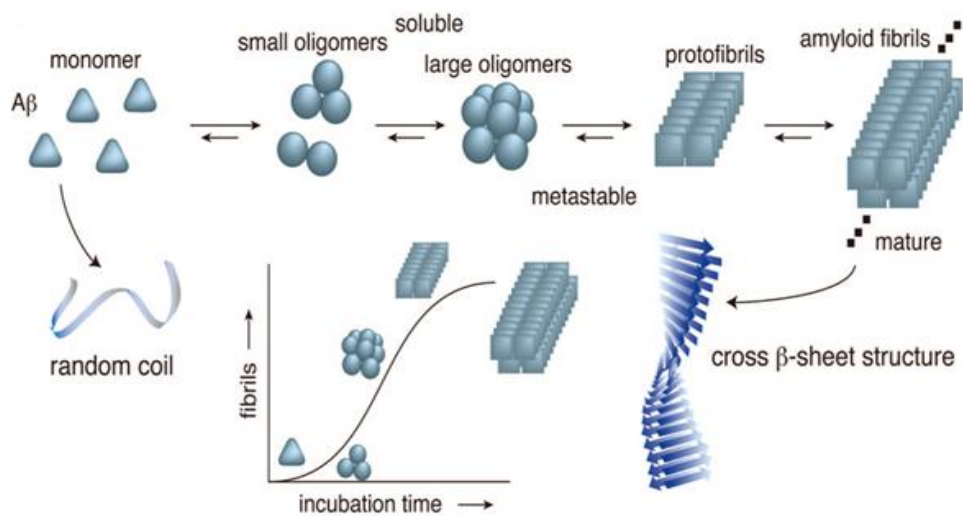
**Figure 2. Amyloid fibril formation of monomeric units to mature level with cross β-sheet conformation.**

## 1.2. Peptide Based Self-assembly for Nano Structures

The peptide self-assembled structures give excellent physical and chemical properties in the field of bio and nano materials. The advantage of peptide-based approaches is the ability to encode the necessary information to address geometrical parameters and to control the physical/chemical properties[18,19]. Various peptides and their derivatives have been identified in achieving various hierarchical architectures, including tubes[20,21], fibers[22,23], planes[24-26], ribbons[23,27], and 3D networks[28,29]. In fibrous peptide, numerous β-strands are organized to form well ordered fibril structures. Generally, β-sheets caused by hydrogen bonding, and control of hydrogen bonds between peptide-peptide and peptide-water molecules are an important factor in peptide assembly. Zhang and coworkers have designed various β-sheets peptides and introduced alternative patterns of hydrophobic and hydrophilic moiety with ionic residues [30-33]. Mihara group, also designed amphiphilic β-sheets peptides, and selectively controled the morphology by changing each amino acid [34] (Fig. 3).
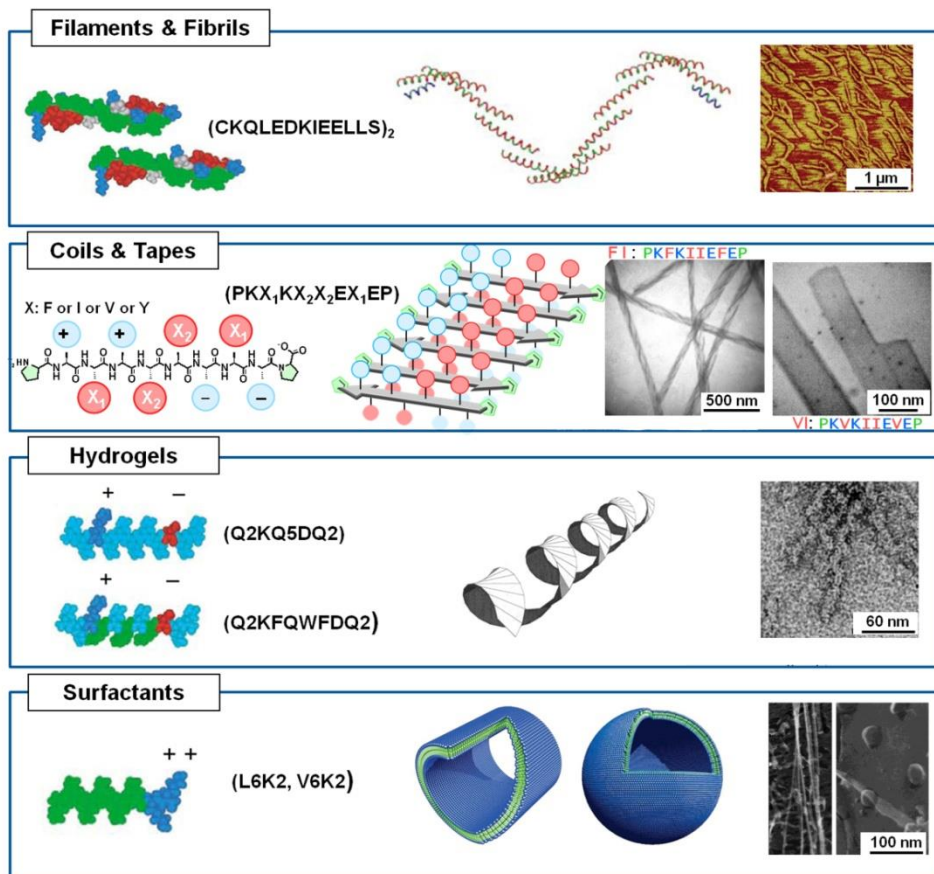
**Figure 3. Various self-assembled peptide nano structures.** a) The filaments and fibril assembled structures with helical peptide[35]. b) The coils and tape type structures with β-sheet peptide[34]. c) Hydrogel type with alternatively charged peptide[36]. d) The vesicle type structurs with amphiphilic peptide[37].

The first reported peptide sequence of self-assembled nano structures are diphenylalanine derivative. They consist of two covalently linked phenylalanine units (diphenylalanine), which plays an important role in the process of molecular recognition and assembly that leads a amyloid fibril formation, as one of the key motifs for synthesis of novel functional nanomaterials (Fig. 4). Various diphenylalanine assembled structures were reported such as wires[22,23,38,39], tubes[40-44], spheres[45], ribbons[27], organogels[46,47] and hydrogels[48,49]. They were all constructed by self-assembly of diphenylalanine units, in which many chemical interactions including hydrogen bonding, aromatic stacking, and electrostatic interaction are involved[50]. These self-assembled structures have simple, stable, and unique mechanical[41], electrochemical[42], and optical properties[43,51]. Therefore, diphenylalanine structures have a wide range of applications such as sensor, bio-imaging, and encapsulated drug delivery system. In particular, Görbitz *et. al.* provided the evidence of aromatic stacking of diphenylalanine units[50]. He found the array of diphenylalanine stabilized by surrounding water. Gazit *et. al.* also investigated the molecular dynamics of diphenylalanine nanotubes assembly by NMR spectroscopy[52]. They showed diphenylalanine molecules migrated out of water suspension shells to form aggregates, which was confirmed by the decrease of diphenylalanine peaks and the increase of water signal[53,54] (Fig. 5).
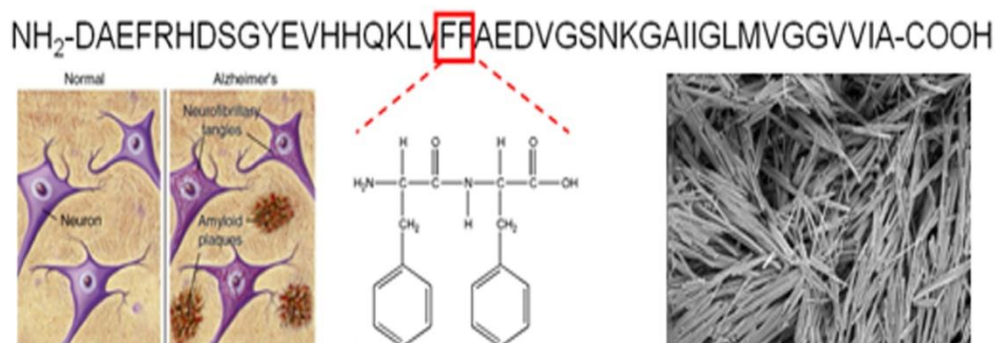
**Figure 4. The main constituent of peptide sequence (Phe-Phe) which exist in amyloid plaques in Alzheimer's disease patients[21].** The image shows the nano wire formation by diphenylalanine residues..
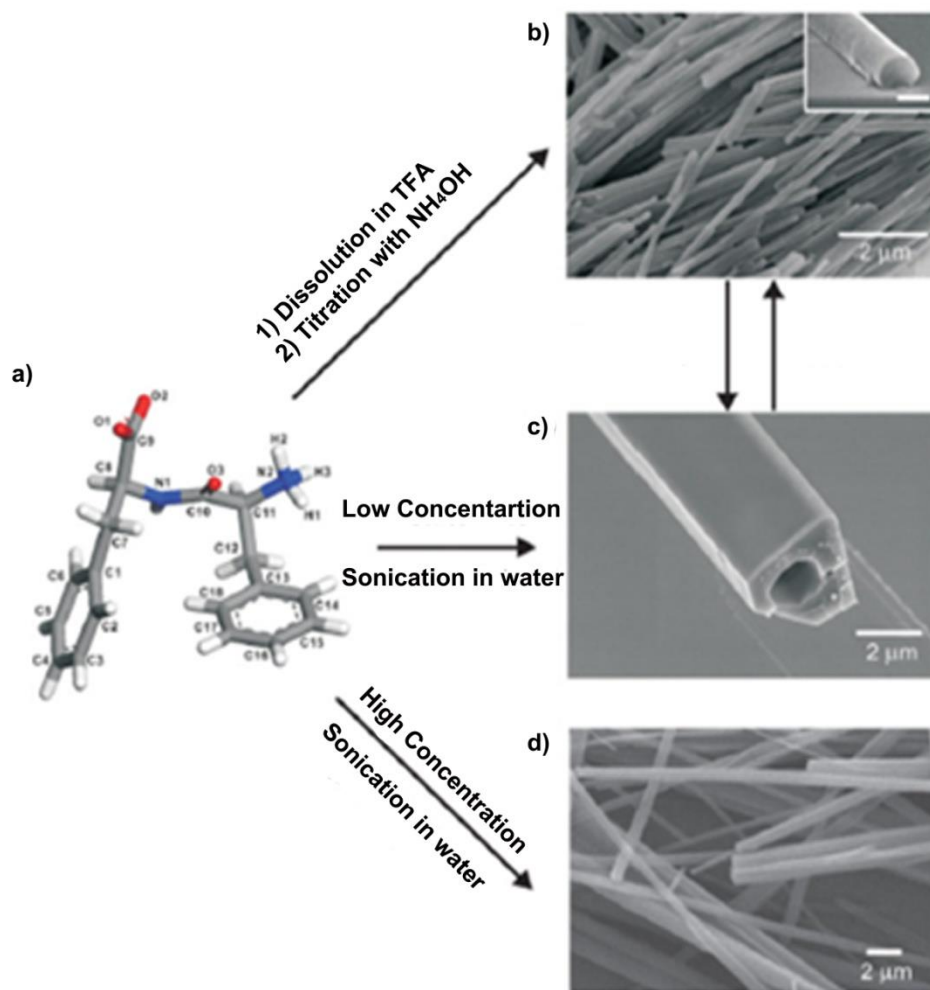
**Figure 5. Schematic mechanism of diphenylalanine(Phe-Phe) nano wires and tubes.** a) Molecular structure of diphenylalanine. b) Dipheylalanine nanofibers dissolved in trifluoroacetic acid (TFA). c) Diphenylalanine nanotube by sonication of diphenylalanine nanofiber in water[54].

## 1.3. The Role of Tyrosine in Nature

  Tyrosine is one of the most significant amino acids that determine the folding geometry[55] in multi-protein organization and facilitate proton-mediated electron transport[56]. Protonation and deprotonation of hydroxyl group of tyrosine can be coupled with photo-excitation in chlorophyll, that allow for the efficient electron transport in photosystem II[57] (Fig. 6) and induce abrupt folding change in photoactive yellow proteins. In addition, a flea can leap 100 times its own height. This high elasticity arises from the crosslinking of multiple tyrosine residues and from the ordering of hydrophobic domains (Fig. 7). For example, in a family of elastic proteins such as resilin[58] and gluten[59], the chemical crosslinks between tyrosine residues induce a protein network, providing high stiffness and efficient energy storage.
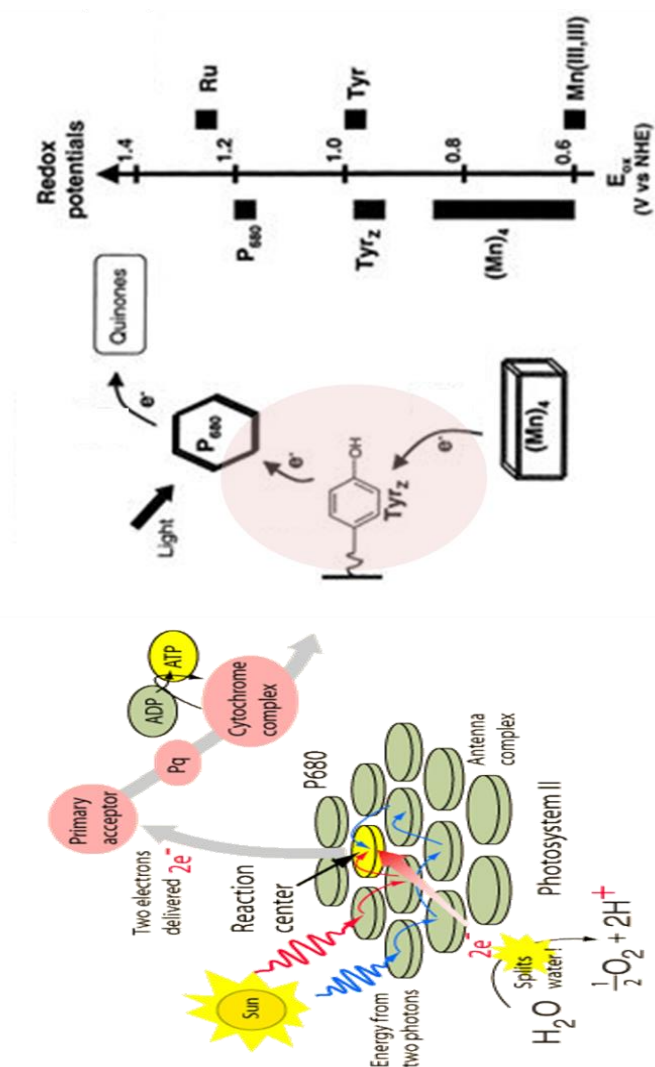
**Figure 6. Tyrosine mediated electron transfer in photosynthesis.** a) Electron transfer route in Photosystem II. b) Redox potential level of tyrosine and mechanism of electron transfer in Photosystem II[60].

In addition, tyrosines are transformed to various structures and show significant role in several enzymes such as galactose oxidase, amnine oxidase, cytochrome c oxidase, catalase, and lysyl oxidase[61] (Fig.7) For example, tyrosine radicals can cooperate with a neighboring cysteine, as exemplified by ribonucleotide reductase and galactose oxidase. A class I ribonucleotide reductase produces sequential radicals of multiple tyrosine groups with Mn(IV) or Fe(IV) ions[62] and oxidizes cysteine residues, generating a sulfhydryl radical[63] to reduce deoxyribonucleotides to ribonucleotides. Galactose oxidase converts primary alcohols to aldehydes via a tyrosyl radical generated by a Cu(II) ion[64,65] with the reduction of oxygen to hydrogen peroxide[66,67]. In the active site of the galactose oxidase, copper ion is ligated by two histidines, one tyrosine at axial position, and other tyrosine at equatorial position, crosslinked by cysteine residue[68-70]. In addition, tyrosine residues act as a key amino acid in the enzymatic reactions such as amine oxidase[71], cytochrome c oxidase[72,73], catalase[74], and lysyl oxidase[75].

Recently, sheet-forming propensities of all possible 7-mer sequence domains occurring in an amyloidogenic protein, $\beta_2$-microglobulin ($\beta_2$m), were studied and an important role in tyrosine-rich regions was discovered[76] (Fig. 8). Interestingly, this study showed that the sequences containing more tyrosine residue exhibited higher Tango score. This observation suggests the important role of tyrosine in self-assembly process. Therefore, we systematically introduced repeating tyrosine units into peptides of various lengths to study the effect of the peptide sequence on self-assembly.

11
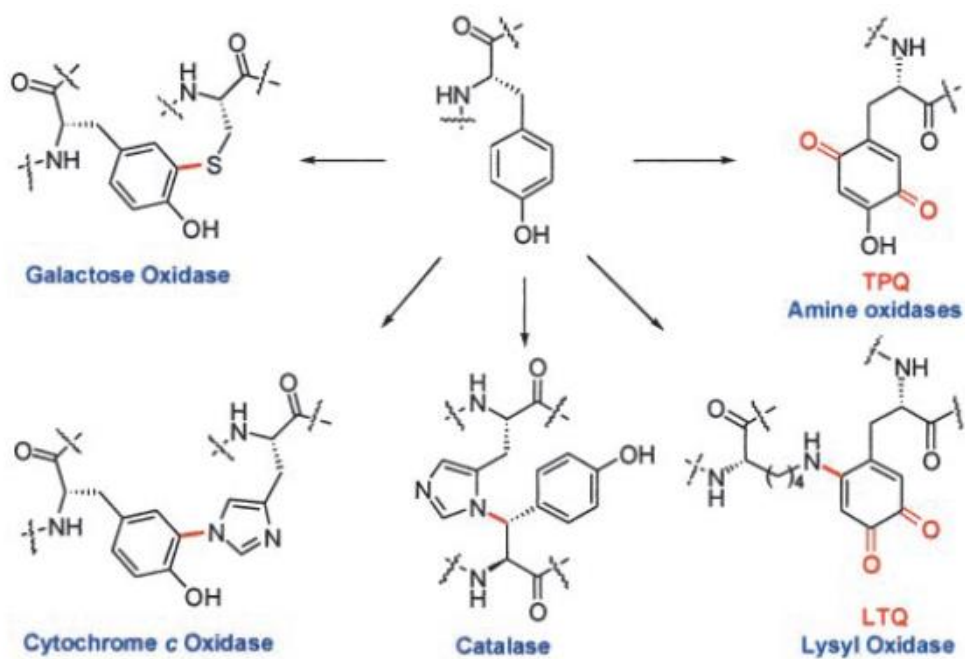
**Figure 7. The structures of post-modified tyrosine resides in various enzymes.**
Red line shows newly formed chemical bonds[61].

**a)**

```
      1              11                 21                 31                 41
IQRTPKIQV■  SRHPAENGKS  NFLNC■VSGF  HPSNIEVDLL  KNGERLEKVE

     51              61                 71                 81                 91
HSDLSFSKDW  SFYLL■■TEF  TPTEKDE■AC  RVNHVTLSQP  KIVKWDRDM
```

**b)**

| Position | $\beta_2$m amino acid sequence | Tango score |
|----------|-------------------------------|-------------|
| 59-65 | DWSFYLL | 232.7 |
| 60-66 | WSFYLLY | 218.7 |
| 61-67 | SFYLLYY | 481.3 |
| 62-68 | FYLLYYT | 432.9 |
| 63-69 | YLLYYTE | 133.7 |
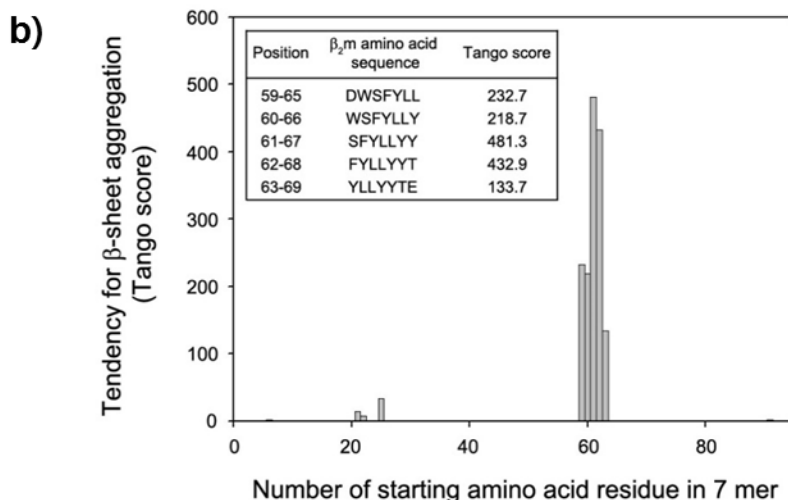
**Figure 8. Identification of aggregative peptide segments within β₂-microglobulin (β₂m).** a) Amino acid sequence of human β₂m. Numbers above the letters indicate the position of amino acid in the protein. Tyrosine residues were highlighted by black boxes. b) Tango prediction was performed for β₂m with a window size of 7-amino acid residues by using the algorithm provided at www.tango.crg.es. The sequences that had an intense Tango score were summarized in the inset table.

13

## 1.4. Cross-coupling Reactions by Heterogeneous Palladium Catalyst

Palladium which is a representative catalyst of cross-coupling reactions such as Suzuki, Heck, Negishi, and Sonogashira reaction is useful for the synthesis of important bioactive molecules (Fig. 9). The successful results of cross-coupling reactions have been achieved with various homogeneous palladium catalys. However, the homogeneous catalysts possess separation problem of expensive transition metal catalysts for recycling. In general, solid supported catalysts, immobilized on carbon materials[77-80], polymers[81-83], silica compounds[84-86], and metal oxide particles[87-92] provide a vehicle to separate and reuse of the catalysts. Cross-coupling reactions combine two molecular fragments and lead to the formation of new bonds such as C-C, C-N, and C-O, and catalyzed by transition metal catalysts. So far, many works have been aimed for improving the catalytic activities and reaction conditions for cross-coupling reactions. However, not only the performance of catalytic properties, but also environmentally friendly, economically cheap, non-toxic reaction conditions, especially reaction in aqueous phase, still remain a challenge. For example, various additives including cetyltrimethylammonium bromide (CTAB)[93], tetrabutylammonium bromide (TBAB)[94-96], phosphine ligands and other bulky ligands have been used as solution for reactions in aqueous media. A typical mechanism for Suzuki cross coupling reactions are summarized in Figure 10. A zerovalent of palladium stabilized by electron donating bulky ligands

undergoes oxidative addition of aryl halides. And reductive elimination occurs to couple two aryl groups and zerovalent transition metals are regenerated. The recent issue in cross coupling reaction is the use of aryl chlorides for selective and effective reactions because they are readily available and inexpensive. However, the activation of aryl chlorides are much difficult to activate than aryl iodides and bromides. Eventhrough there were many reports on heterogeneous palladium catalysts, however, few examples were successful in aryl chloride activation during cross-coupling reactions [96-98], and even non additive process has never been reported yet.
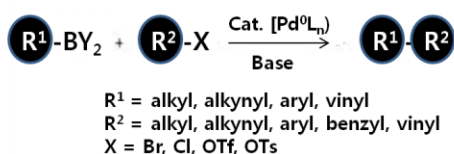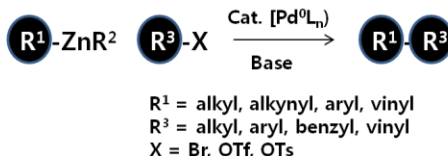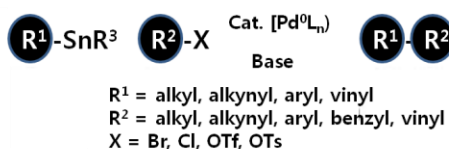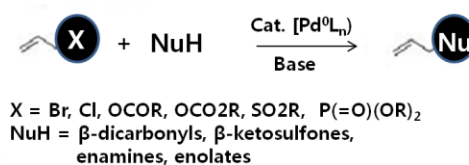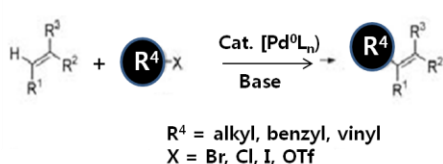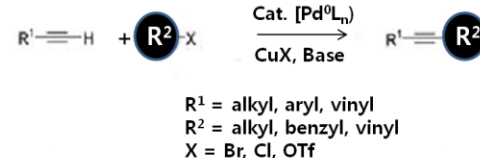
**Figure 9. Examples of various solid supported Pd catalyzed cross-coupling reactions:** Suzuki, Nigishi, Stille, Tsuji-Trost, Heck and Sonogashira reaction.
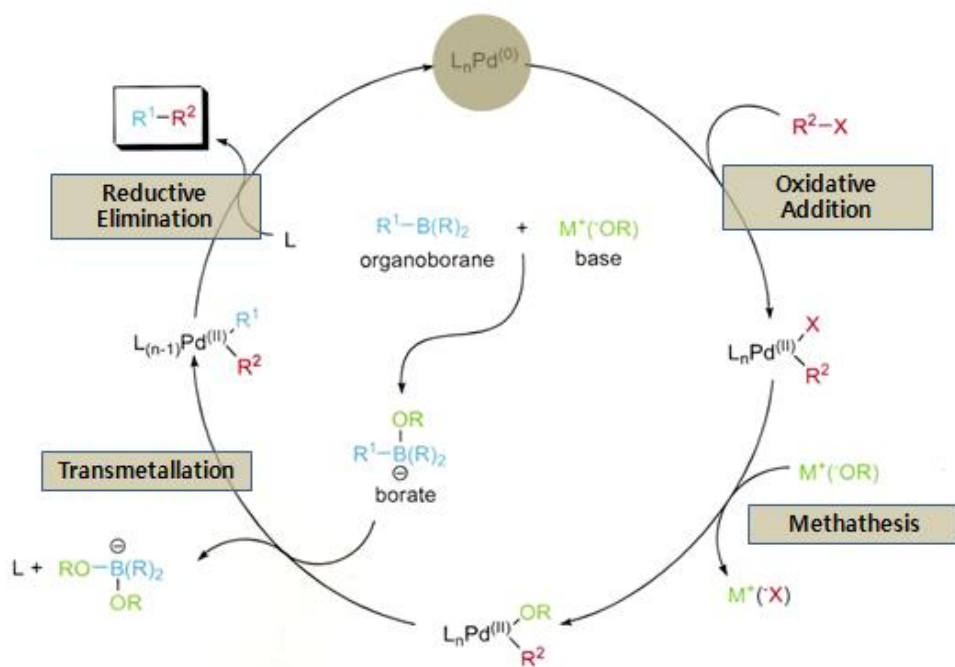
**Figure 10. Catalytic cycle of transition metal catalyzed cross-coupling reactions.**

## 1.5. Bio-catalysts for Various Organic Reactions

It is interesting to borrow the ideas from various enzymes to create new catalytic system for various chemical reactions[99]. Recently, enzyme-like catalytic systems for synthesizing metal ion included tertiary structures, and controlled assembly of multiple peptide chains are designed by computational methods[100-105]. The self-assembled peptide can induce specific binding of metal ions, and the peptide nano materials are good candidates as a templates and support for catalysts because these bio-inspired peptide scaffolds can afford a nucleation site of metal ions and assemble into peptide based metal complexes[106]. The biomimetic nano catalysts were also designed using palladium and ruthenium binding histidine, phenylalanine, tyrosine, and dihydroxyphenylalanine (dopa) containing peptides[106-111]. Knecht group found the specific sequence of palladium binding peptide, TSNAVHPTLRHL, by phase display, and the peptide strongly captured palladium ion with histidine residues, and the resulting catalyst gave good catalytic activity in Still cross-coupling reaction (Fig. 11a). Park and Kim group grow diphenylalanine rods on a silicon oxide surface, and then introduced palladium nanoparticles by using atomic layered deposition (ALD) method to the peptide rods and performed Suzuki cross-coupling reaction in micro fluidic system (Fig. 11b). Dihydroxyphenylalanine (Dopa) is a readily available molecule that can capture metal ions for use as a catalyst (Fig. 11c). However, with regard to synthetic systems, it is a challenge to understand the precise mechanism of dynamic complexation and assembly of metal ion and peptide fragments at the molecular level.

18
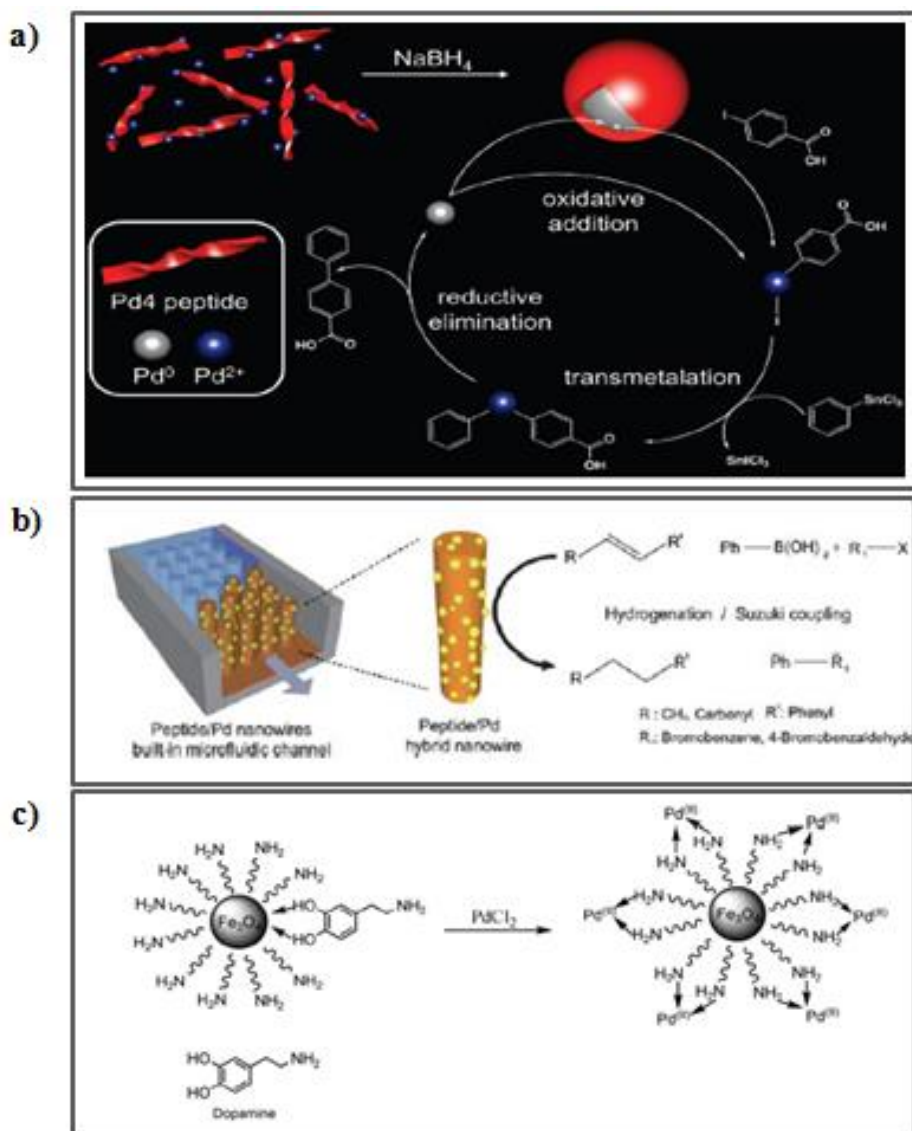
**Figure 11. Various biomimetic catalysts[106-111].** a) Palladium specific binding peptide containing biomimetic catalyst. b) Palladium nanoparticle deposited diphenylalanine nano rods. c) Dihydroxyphenylalanine induced magnetic palladium nano catalyst.

## 1.6. Research Objectives

Biomimetic chemistry is a powerful tool to create diversity and functionality for new materials of versatile superstructures. Nature provides various nano- and micro systems as templates as in the cases of bacteria, enzymes, viruses, antibodies, diatoms and others.

In this thesis, we have focused on the use of tyrosine, one of significant amino acids in biological processes. They can store the mechanical energy by protein folding and also facilitate proton-mediated electron transport in enzymes and photosystem II. To mimic the roles of tyrosine in nature, we systematically introduced repeating tyrosine units into peptides of various lengths to study the impact of the peptide sequence on self-assembly. We identify several tyrosine mediated peptides that can selectively control the air/water interface and, consequently, flatten the rounded top of a hemispherical droplet into a plane by forming a macroscopic two-dimensional (2D) crystal structure. Such faceting is a fascinating example to demonstrate how the balance between interface tension and molecular ordering controls morphology. To the best our knowledge, however, faceted morphology has never been observed in peptide assembly. Therefore, we have developed a peptide-based, sequence-specific method that allows for the precise tuning of molecular structures, site-selective functionalization and control of intermolecular force. In addition, the which faceted YYACAYY film has redox-active property due to tyrosine residues can easily generate tyrosyl radical. For example, when we add $CuCl_2(II)$, the pyrrole monomer polymerize to polypyrrole

sheets on the surface of YYACAYY film. In addition, YYACAYY peptide film can reduce metal ions to metal nanoparticles. We confirm gold and palladium ion can be reduced to nanoparticles by using YYACAYY film as a 2D template. We expect that this metal containing tyrosine 2D scaffold has good catalytic activity.

# 2. Experimental Section

## 2.1. Materials

2-Chlorotrityl chloride (CTC) (100-200mesh, 1.26 mmol/g) resin, filtered polypropylene reactors (Libra tube RT-20M, 20 ml), 2-(1*H*-benzotriazole-1-yl)-1,1,3,3-tetramethyluronium hexafluorophosphate (HBTU), hydroxybenzotriazole (HOBt) and Fmoc-protected amino acids were purchased from BeadTech (Seoul, Korea). *N,N*-Diisopropylethylamine (DIPEA), triisopropylsilane (TIPS), 3,6-dioxa-1,8-octanedithiol (DODT), 4-(3,6-dimethyl-1,3-benzothiazol-3-ium-2-yl)-*N,N*-dimethylaniline chloride (thioflavin-T), β-mercaptoethanol, HEPES buffer, uranyl acetate, and anisole were purchased from Aldrich (St. Louis, MO, USA). Dichloromethane (DCM), *N,N*-dimethylformamide (DMF), methanol, piperidine, diethyl ether and trifluoroacetic acid (TFA), sodium hydroxide (NaOH) and hydrochloric acid (HCl) are obtained from Dae-Jung Chemicals (Korea). Hydrogen peroxide ($H_2O_2$, 30%) was purchased from Junsei (Japan).

## 2.2.　Experimen tal Methods

### 2.2.1. Peptide Synthesis

The peptides were synthesized on a 2-chlorotrityl chloride (CTC) resin (1.26 mmol/g) with Fmoc/tBu chemistry in a filtered reactor. After loading the first amino aicd (0.3~0.5 mmol/g), each coupling step was performed with 2 eq. of Fmoc-amino acid, 2 eq. of HBTU, 2 eq. of HOBt and 4 eq. of DIPEA for 2 hours until the Kaiser-test was turned out negative. DCM and DMF in a raito of 1:1 was used as the solvent. The deprotection step of Fmoc group proceeded for 20 min by 20% piperidine/DMF. Cleavage of the final peptides from the CTC resin was conducted in 93% TFA, 2% TIPS, 2% DODT and 3% anisole for 90 min. The cleavage mixture was filtered and washed with DCM and methanol, and the filtrate was concentrated in vacuum. The resulting residue was precipitated with cold diethyl ether, centrifuged, and dried in vacuum. The peptides were purified with reverse phase HPLC, when necessary, and identified by MALDI TOF and ESI mass spectrometer. The purity of all the peptides was above 95%.

## 2.2.2. Peptide Film & Facet Formation

To identify the key amino acids in facet formation, a number of peptide sequences were synthesized. The conditions for facet formation were tested by varying the dissolution method, temperature, pH, drop size of peptide solution, and peptide concentration. The most effective conditions were chosen based on these preliminary experimental results. Typically, the peptide was completely dissolved in 50 mM HEPES (pH 7.4) by briefly sonicating for 10 min and was then heated at 90°C for 30 min in a closed system. The 30-minute heating at 90°C helped to achieve complete dissolution of peptides in the aqueous solution. An aliquot (100 μl) of the peptide solution was placed on a surface of siliconized glass (Hampton Research, HR3-231) using a pipette. Facet formation was observed on a droplet of peptide solution up to 1 ml, but the maximum volume limit was not identified. When the peptide solution was placed in a Petri dish, a large film formed at the air/water interface, eventually fully covering the surface of the petridish. The diameter of the largest films was 10 cm. Faceting took place along with film formation at peptide concentrations higher than 0.33 mM (0.3 mg/ml). No faceting was observed below 0.33 mM. Faceting was observed over a wide range of pH (3 ~8).

### 2.2.3. Atomic Force Microscopy

A drop of peptide solution was placed on a siliconized glass, and s incubated for 30 min at room temperature to make a facet at water-air interface. The planar part at the top of the droplet was transferred onto a clean silicon wafer or a mica surface. The samples adsorbed on the surface were washed with distillated water to remove salt, and then air-dried for 10 min. AFM images were obtained with Dimension 3100 (Veeco Instruments, Woodbury, NY) in tapping mode. Measurements were carried out using silicon cantilevers with a spring constant of 21-78 N/m (Nanoscience) and the resonance frequency of 260-410 kHz. The operating conditions for AFM were 0.5 Hz of scan rate.

### 2.2.4. Transmission Electron Microscopy

An aliquot (20 μl) of the peptide film solution was deposited on a carbon-coated copper grid (200 mesh) and air-dried for 5 min. The remaining liquid was removed with filter paper. For negative staining, the peptide was stained with 2% aqueous uranyl acetate (Electron Microscopy Sciences), and centrifuged at 13,200 rpm for 2 min. Then, the remaining staining solution was also removed with filter paper. The prepared TEM grids were kept in a desiccator before TEM imaging to ensure the removal of moisture. Then, the microscopic images were observed at 80 kV using a JEOL JEM-1010 transmission electron microscope.

### 2.2.5. Fluorescence Imaging

The peptide film was stained with thioflavin-T. The peptide (2.2 mM) was dissolved at 90°C for 30 min in 20 mM HEPES buffer (pH 7.4) containing 250 μM thioflavin-T. Aliquot (100 μl) of the solution was dropped onto a siliconized glass and was air-dried for 2 hours to induce the film formation. After the facet was transferred onto a pre-cleaned microscope slide, the sample was covered with a coverslip and the remaining solution was removed by using a filter paper. The dye-bound peptide film was subjected to fluorescence imaging analysis at $470 \pm 30$ nm with excitation at $430 \pm 10$ nm. The fluorescence images were obtained by using a Deltavision RT (AppliedPrecision, USA) microscope with an Olympus IX70 camera.

### 2.2.6. Matrix-assisted Laser Desorption/ionization Time-Of-Flight Mass Spectrometry

The matrix solution was prepared by dissolving 10 mg of 2,5-dihydroxy benzoic acid (DHB) in 1 ml of a 3:7 mixture of deionized water and acetonitrile containing 0.1% TFA. Then, an aliquot (0.5 μl) of peptide or peptide film containing solution was dried, dissolved with 0.5 μl of 20 mM dithiothreitol(DTT), followed by addition of 8 mM of aqueous, and incubated $NH_3$ for 5 min. The reaction was quenched by adding 0.5 μl of the matrix solution. All data were acquired with an Autoflex MALDI-TOF mass spectrometer (Bruker Daltonics) equipped with a

Smartbeam laser controlled by FlexControl software (Bruker Daltonics). Mass spectra were acquired in the positive reflector mode using a 140-ns pulsed ion extraction and 1,000 mV digitizer sensitivity.

### 2.2.7. Electrospray Ionization Mass Spectrometery

The peptide film was dissolved in 0.5% acetic acid/MeOH. Mass data was confirmed by the analytical high performance liquid chromatography electrospray ionization mass spectrometry (Thermo - Finnigan LCQ deca XP MS ESI-MS) and Phenomenex C4 reverse-phase column (4 μm, 100 × 3 mm). The gradient was 10-65% acetonitrile in $H_2O$ containing 0.5% formic acid over 21 min.

### 2.2.8. X-ray Diffraction Analysis

The X-ray diffraction data were measured over the scattering angle ranging from 3˚ to 60˚ at 2θ step of 0.02˚ using $CuK_\alpha$ radiation with a secondary graphite monochromator in the reflection geometry at room temperature (Rigaku, D/max2200VK). Si (NIST SRM 640c) powder was used as an external standard to correct the zero-point shift for the measured diffraction data.

### 2.2.9. Fourier Transform Infrared Spectroscopy

Fourier-transform infrared spectra of YYACAYY (monomer or peptide films) were analyzed with a Thermo Nicolet 6700 FT-IR spectrometer equipped with an attenuated total reflection (ATR) accessory. The film on the droplet was transferred to a clean silicon wafer, air-dried for 24 hr and placed on a ZnSe/diamond. The peptide film from a single batch gave an insufficient signal, and thus, films from twelve batches under the same conditions were transferred to the same silicon wafer for analysis. The scanned wave numbers ranged from 300 $cm^{-1}$ to 4,000 $cm^{-1}$ at a resolution of 1.93 $cm^{-1}$. The spectra were scanned eight times.

### 2.2.10. Raman Spectroscopy

Raman spectra of YYACAYY (monomer or peptide films) were analyzed with Horiba Jobin-Yvon/LabRam Aramis Raman spectrometer (diode laser 785nm, power = 1mW). The film on the droplet was transferred onto a clean gold coated silicon wafer and air-dried for 24 hr. The single transfer of film did not give significant signals. Therefore, multiple transfers of the films were necessary on the substrate. The scanned wave numbers ranged between 200 $cm^{-1}$ and 3000 $cm^{-1}$ with 300 sec scanning in average.

## 2.2.11. Zeta Potential Measurement

The surface charge of YYACAYY nanofiber/film in aqueous solution was measured with Malvern Zetasizer, (Model Nano ZS, Malvern Instruments Ltd., UK) with a He-Ne (633 nM) laser (4.0 mW). The zeta potential data were collected with an Avalanche photodiode with Q.E. > 50% at 633 nM using the M3-PALS measurements technique.

## 2.2.12. Computational Modeling Study

All computational modeling was performed using the Standard Dynamics Cascade Protocol in Discovery Studio modeling program (Version 3.1, Accelrys Inc., San Diego, CA). Each system was pre-applied with a CHARMm (Chemistry at Harvard Macromolecular Mechanics) force field. The initial structures were first minimized by the steepest descent method, followed by conjugate gradient minimization to an RMS gradient of 0.01. The distance constraints were then applied, and the minimization steps were repeated. The structures were heated and equilibrated over 10 ps from 5 to 1,000 K, with velocities assigned every 0.001 ps. To randomize the structures, distance constraints were not used in the first step. Molecular dynamics simulations were run for 5 ns, with distance constraints applied with a force constant of 0.06 kcal mol$^{-1}$ Å$^{-2}$. Next, the force constants were scaled to 120 kcal mol$^{-1}$ Å$^{-2}$ over 7 ps in a series of 0.4 ps molecular dynamics runs. The system was allowed to evolve for 6 ps and was then cooled to 300 K after 7 ps. At this temperature, the force constants were reduced to their final values of 60 kcal

mol$^{-1}$ Å$^{-2}$ over 4 ps in a series of 0.4 ps molecular dynamics runs. The system was allowed to equilibrate for 5 ps, followed by a final molecular dynamics run for 15 ps. The coordinates of the final 5 ps of the 15 ps molecular dynamics were calculated by averaging and minimized by 1,000 steps of the steepest descent method followed by conjugate gradient minimization to a RMS gradient of 0.01, with distance constraints set to 60 mol$^{-1}$ Å$^{-2}$.

### 2.2.13. Tyr Peptide-Polypyrrole Supported Palladium(II) Catalyst (Tyr peptide@PPy@Pd NP)

The tyrosine peptide (YYACAYY) was completely dissolved in 10mM HEPES (pH 7.4) by brief sonication for 10 min and heating at 90˚C for 30 min in a closed system. After heating, sodium tetrachloropalladate(II) hydrate (1.3~2.6 mg, 2-4 equiv). was addd directly to the peptide solution. The peptide solution containing palladium ion was placed on a siliconized glass surface (Hampton Research, HR3-231) using a pipette. And, 1ml of neat pyrrole monomer drop was placed near the peptide-palladium ion solution. On the surface of peptide drop pyrrole monomer started to polymerize in few minutes. We can observe the peptide drop was slightly covered by polypyrrole. After 2 hours, the polypyrrole coated peptide film containing palladium nanoparticle was collected and washed by water to obtain Tyr peptide-polypyrrole supported palladium catalysts.

# 3. Results and Discussion

## 3.1. Preparation of Tyrosine Peptide Derivatives and Their Assembly

### 3.1.1. Tyrosine Peptide Based Assembled Nano Structures

Repeating tyrosine units were systematically introduced into peptides of various lengths to study the effect of peptide sequence on self-assembly. Cysteine was added to confer folding stability through disulfide bridges[18]. Alanine and phenylalanine were inserted at specific sites on the peptide sequences to understand the self-assembly mechanism. The peptides were dissolved in 50 mM HEPES buffer (pH 7.4) and placed on a siliconized glass. As listed in Table 1, the arrangement of each amino acid and its composition were the main determinants of peptide nanostructures. Dityrosine (YY) and trityrosine (YYY) formed long nanofibers with 15 nm in diameter in the aqueous solution. The more hydrophobic tetratyrosine (YYYY) tended to bundle into random aggregates. YCY and CYYCYYC aggregated randomly. However, we observed the faceting phenomenon and planer structures from several sequences that are symmetric and have cysteine at the center. YYCYY was the first sequence in our study that was found to form a facet within 10-minutes under the experimental conditions. CYY also has a thiol group to form a disulfide bond, however, it did not assemble into planar structure, but only fibers. While searching for other sequences, we found that when alanines were inserted

between cysteine and tyrosine (YYACAYY), facets were formed within one minute, showing the highest facet-forming capability and quality. YYAEAYY and YYAKAYY assembled into 2D structures, however, they did not form any facet. It means that the physical properties of the structure were not strong enough to overcome the high surface tension of the water droplet. Interestingly, YYY assembled into nanofibers and nanospheres similar as triphenylalanine[112](Fig. 12). FYCYF can form 2D films that result in a facet, but at the same time, coiled nanofibers co-exist in solution. When each of the four tyrosine positions was replaced by alanine, the resulting YYACAYA, YYACAAY, YAACAYY and AYACAYY peptide sequences could not form facets. These results suggest that all four tyrosine groups in YYACAYY are involved in film growth. Additionally, we observed that YYCYY, YYYCYYY, YYAACAAYY, YYGCGYY, YFCFY and FYCYF induced facet formation. When we replaced tyrosine with phenylalanine at each terminal position of the peptides, such as in FYCYF and FFCFF, the activity of faceting was inhibited. Therefore, among the eight sequences that were able to form facets, YYACAYY was chosen for the detailed mechanism study (Table 1).

**Table 1. Summary of Tyrosine Containing Peptides Studied for the Assembly**

| Facet-forming peptides | | Non-facet-forming peptides | |
|---|---|---|---|
| Sequence | Kinetics of facet formation[a] | Sequence | Observed structures[c] |
| [1]YYCYY | Fast | [9]YCY | Random aggregates |
| [2]YYYCYYY | Very fast[b] | [10]CYY | Nanofiber |
| [3]YYACAYY | Very fast | [11]YY | Nanofiber |
| [4]YYAACAAYY | Very fast | [12]YYY | Nanofiber |
| [5]YYGCGYY | Very slow | [13]YYYY | Random aggregates |
| [6]YFCFY | Fast | [14]YYAYY | Planar structure |
| [7]FYCYF | Slow | [15]CYYCYYC | Random aggregates |
| [8]FFCFF | Very slow | [16]YYAKAYY | Planar structure |
| | | [17]YYAEAYY | Planar structure |

[a]We defined the facet formation time as the point when the diameter of a facet reaches 2 mm. The kinetics of facet formation was described by the following criteria.

| | |
|---|---|
| "Very fast" | Formation within 1 min |
| "Fast" | Between 1 min and 30 min |
| "Slow" | Between 30 min and 60 min |
| "Very Slow" | More than 60 min, small facet |

[c]For the peptide sequences that cannot drive facet formation, the assembled peptide structures were analyzed by TEM.
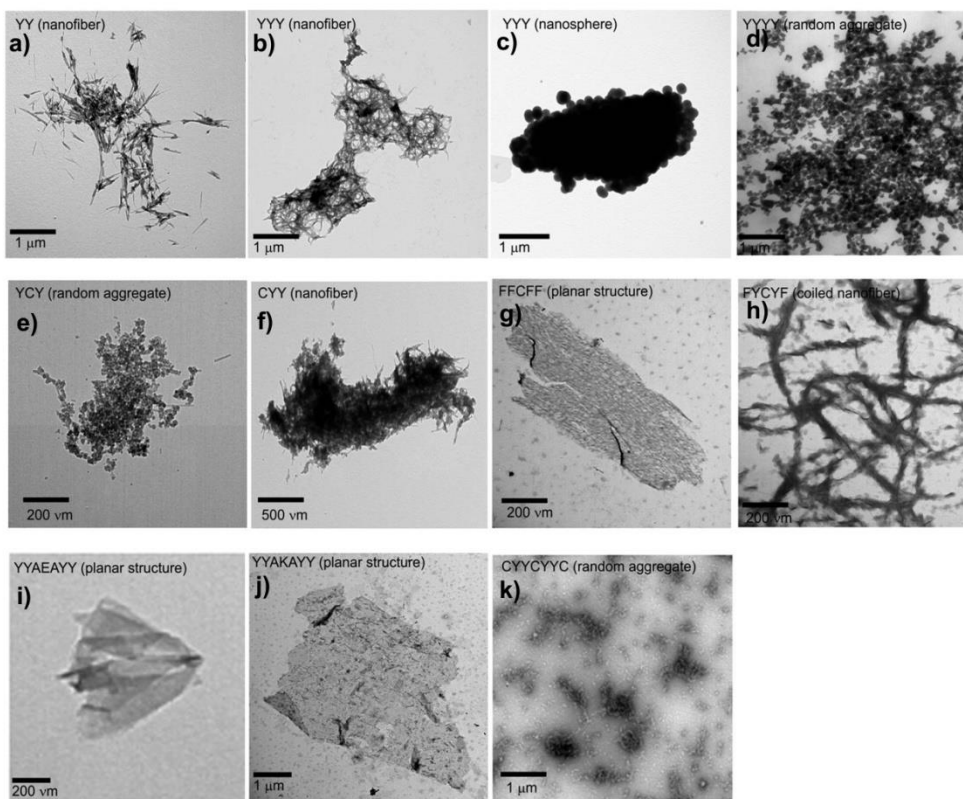
**Figure 12. Transmission electron microscopy (TEM) images of various structures of peptide library.** a) YY (Nanofiber); b) YYY (Nanofiber); c) YYY (Nanosphere); d) YYYY (Random aggregates); e) YCY (Random aggregate); f) CYY (Nanofiber); g) FFCFF (planer structure); h) FYCYF (Coiled nanofiber); i) YYAEAYY (Planer structure); j) YYAKAYY (Planer structure); k) CYYCYYC (Random aggregate).

The relative rate of the facet formation was determined at various peptide concentrations (0.33, 0.55, 1.10, 1.65, and 2.20 mM in 50 mM HEPES, pH 7.4) with different sequences (YCY, YYCYY, and YYYCYYY). The relative rate of facet formation were normalized based on the rate of YYCYY (1.1 mM). YCY did not form any facet regardless of the concentration due to the lack of $\pi$-$\pi$ interacting sites (Fig. 13a). The facet formation was dependant on the concentration of peptide. We can observe the initiation of facet formation at 0.3mM. The facet formation was accelerated until the concentration of peptide reached to 2.2mM (Fig. 13a). Interestingly, adding just one tyrosine residue to both ends of YYCYY (YYYCYYY) resulted in wrinkled multiple facets. We speculate that additional tyrosine for $\pi$-$\pi$ stacking might change their morphology from single facet to multiple facets (Fig. 13c).
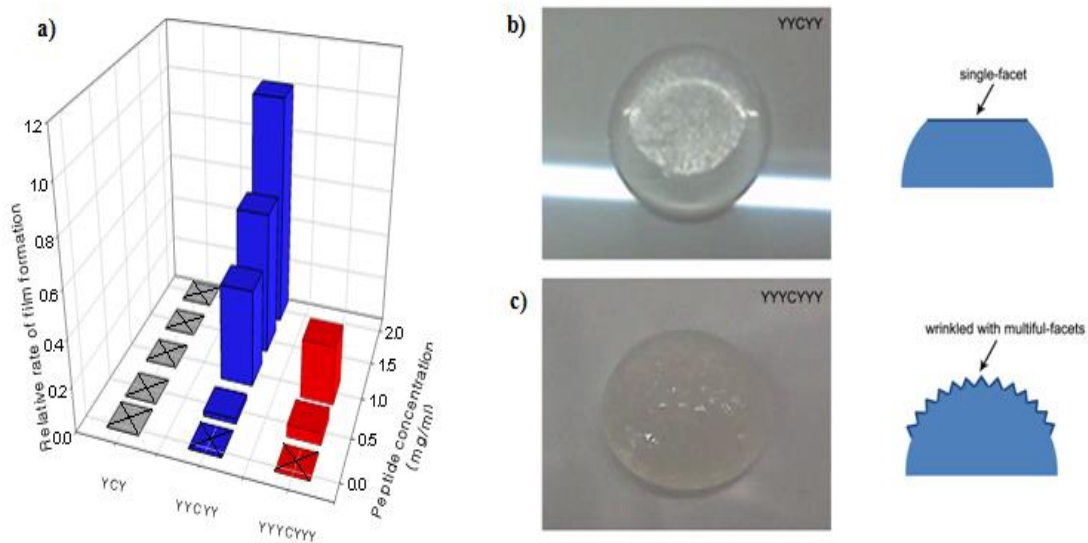
**Figure 13. The influence of the number of tyrosine residues on faceting behavior.** a) The graph of relative rate of the facet formation at various peptide concentrations. b) The single facet formation at YYCYY sequence. c) The multiple facet formation at YYYCYYY sequence.

### 3.1.2. Film and Facet Formation at Air/water Interface

We identify several specific peptides that can selectively control the air/water interface and, consequently, flatten the rounded top of a hemispherical droplet into a plane by forming a macroscopic two-dimensional (2D) crystal structure. The shape evolution of the droplet was monitored from a side view. A bright region in the middle of a droplet is due to the backlight transmission (Fig. 14a). A total of 80 μl of YYACAYY solution was placed on a glass slide. After 2 min, a facet appears on the top surface and grows continuously. We also found a large and thick peptide film formed on the whole air/water interface. When a petridish was filled with 5 ml of YYACAYY peptide solution (Fig. 14d). The TEM images showed uniform and laterally extended peptide films were formed on air/water interface (Fig. 14c). There is a continuous interplay between the 2D crystal lattice structure and the geometry of the interface on which it is placed[113]. In most cases, the interface tension is high, and the overall shape of the 2D-assembled structure follows the shape of the interface. At the microscopic level, two-dimensional ordering on a curved surface typically generates topological defects[114-118], such as disinclination and dislocation, or induces symmetry-breaking instability[119] because the local ordering favored by molecular interactions cannot propagate laterally throughout an entire system on a curved surface. For example, hexagonal close packing of spherical particles cannot perfectly tile a curved surface without heptagonal or pentagonal packing[115-117]. The geometric constraint imposed by curvature, nevertheless, can be overcome, and planar facets can appear when the elastic modulus of a 2D crystal is sufficiently

large or the interface tension is weak. For example, faceted surfaces can be found in viral capsids formed by the crystalline packing of proteins[120], hydrophobin protein film[121], vesicles assembled from block copolymers[122], wax colloidal disks packed with surfactants[123] or smectic A droplet on a flat substrate[124]. Here, we developed a peptide-based, sequence-specific method that allows for the precise tuning of molecular structures, site-selective functionalization and control of intermolecular forces. As a result, the assembly process is controllable in an entire droplet and scalable to a large length ($>100$ cm$^2$). We also found that oxygen is needed for facet formation. When 80 μl of the YYCYY solution was dropped on a glass plate and incubated in an oxygen free desicator for 60 min, facet formation did not occur (Fig. 15C). We suppose that oxidative environment is essential in faceting, which can accelerate the disulfide bond formation between the peptide monomers. After the film was transferred on a carbon coated grid, the sample was negative-stained with 2% aqueous uranyl acetate for TEM analysis (Fig 15b).
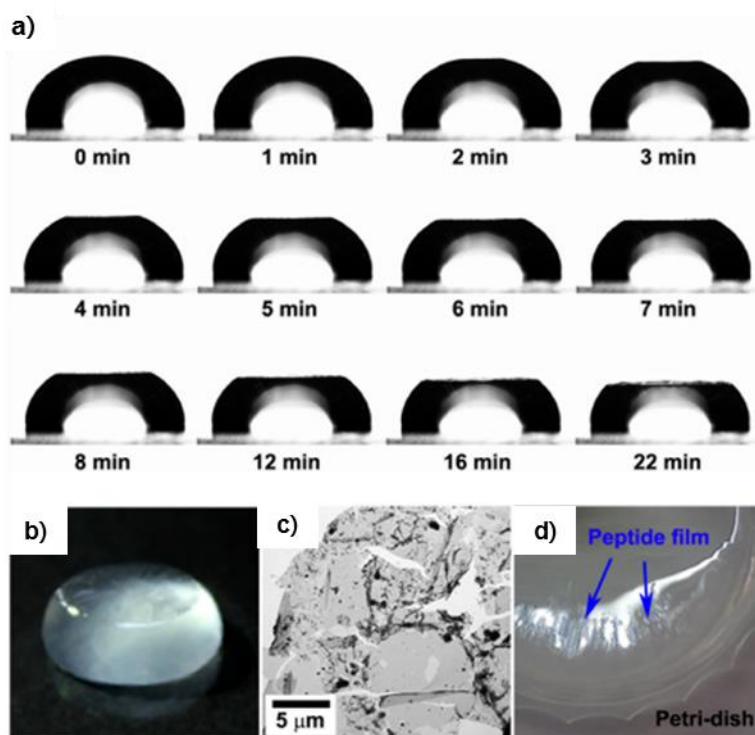
**Figure 14. Faceting and large 2D peptide film formation on air/water interface with YYACAYY.** a) The time dependency of facet formation. b) The photographic images of YYACAYY peptide drop. c) TEM image of YYACAYY peptide film. d) Large size peptide film formed at air/water interface.
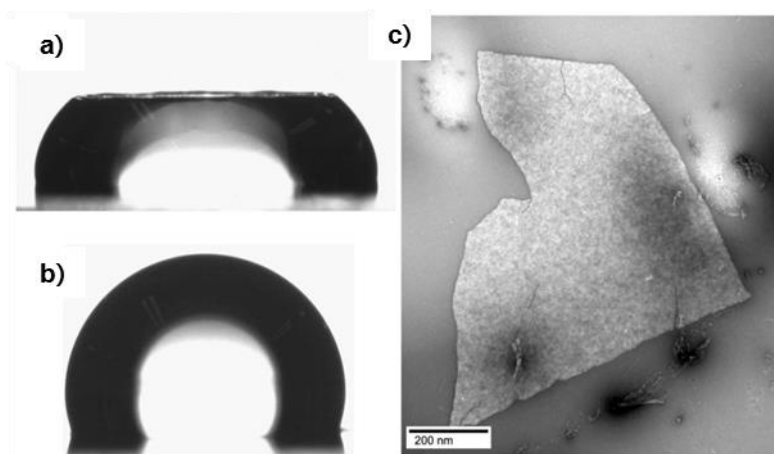
**Figure 15. The effect of oxygen on faceting.** a) The facet formation with YYCYY after 20min. b) The faceting did not occur in oxygen free condition. C) TEM images of YYCYY peptide film.

## 3.2. Characterization of Tyrosine Peptide Derivaties and Their Assembly

### 3.2.1. Kinetics of Facet Formation

Faceting started from the center of the droplet within 1–2 min after dropping and grew continuously to the lateral direction. After approximately 20 min, when the size of the facet was close to the circumference of the water/glass boundary, lateral growth stopped. Faceting of droplet was dependent on the size of the droplet. The kinetics became faster as the droplet size decreased (Figure 16). It was assumed that the decrease of droplet size would accelerate the evaporation of water molecules at the interface and would result in the acceleration of the facet formation. With the size less than 20 μl, however, the facet formation was significantly delayed because of its high surface tension. Facet formation was observed at a wide range of pH (between 3 and 8), but the kinetic activity was the highest at pH 5.5, which is close to the isoelectric point of YYACAYY. Facets were formed more quickly at 4°C than at room temperature or at 60°C. The facet formation time was defined as a time when the facet size reached 2 mm in a 80 ul water droplet. Below pH 3, the peptide could not be dissolved and formed white aggregates. Above pH 8, the facet did not form. As shown in Ffigure 17a, the facet can form most effectively at pH 5. According to the computation analysis (http:// web.expasy.org/compute_pI), the pI value of YYACAYY is 5.8. From zeta potential analysis, the isoelectric point (pI) of the peptide supposed to be around pH 5.3. At pH 3, the Zzeta potential was 3.38 ± 0.14 mV, and at pH 8. The Zeta potential had a negative value of -25.28 ± 0.09 mV

(Fig. 17b). As the facet formation needed to overcome the surface tension of the water droplet, the facet-forming kinetics became much slower for a droplet with a high curvature. When a droplet was placed on a hydrophobic Teflon surface, the curvature increased at the given volume. As a result, the facet formed more slowly, with a smaller final facet size (Fig. 18). After 50 μl of YYACAYY solution (1.1 mM) was dropped on a hydrophobic Teflon surface and incubated for 83 min at room temperature, the side-view of the droplet was observed by the optical microscope. Although the faceting kinetics was slower than that of peptide solution on a glass plate, the peptide was assembled on even a highly curved interface (blue arrows).
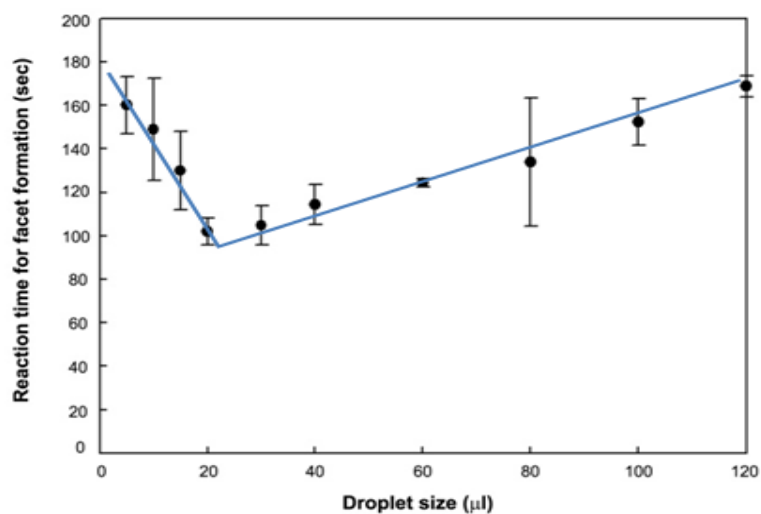
**Figure 16. Kinetics of facet formation obtained from various sizes of droplet.** The kinetics became faster as the droplet size decreased.
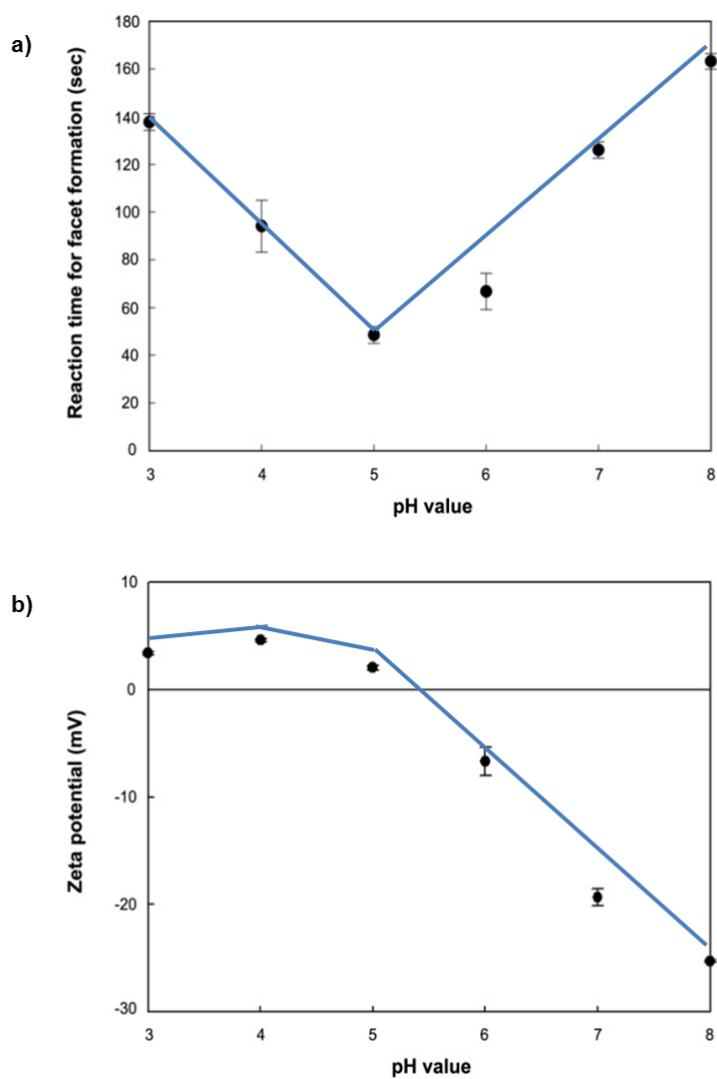
**Figure 17. pH Dependency of facet formation and zeta potential of YYACAYY.**
a) The reaction time of faceting at various pH. b) The Zeta potential of YYACAYY at various pH.
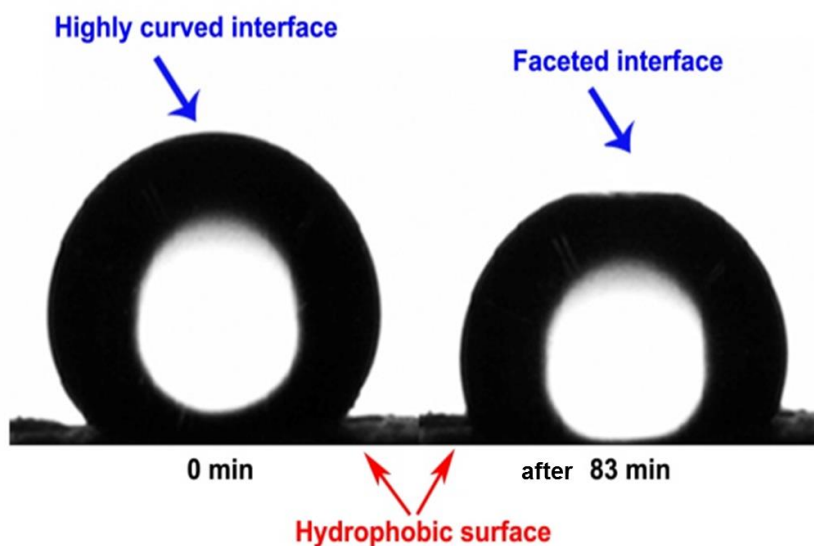
**Figure 18. Faceting of the peptide droplet with a high curvature on a hydrophobic surface.** YYACAYY (50 μl , 1.1 mM) was used for the droplet on Teflon film.

### 3.2.2. TEM Images of Film Structure Prepared from Various Concentration

We have observed that the minimal peptide concentration for facet formation was 0.22 mM, but only small pieces of scattered, thin nanosheets were formed at this concentration. The size and thickness of the films increased as the peptide concentration increased (Fig. 19). The microscopy images illustrate a tendency of increasing the film size as the peptide concentration increases. TEM images were obtained after the facets were fully developed (30 min). The films grew laterally and became thicker as the concentration increased to 1.1 mM. At 1.1mM, the film grew large enough to cover the entire area (97 μm x 97 μm) of grid.
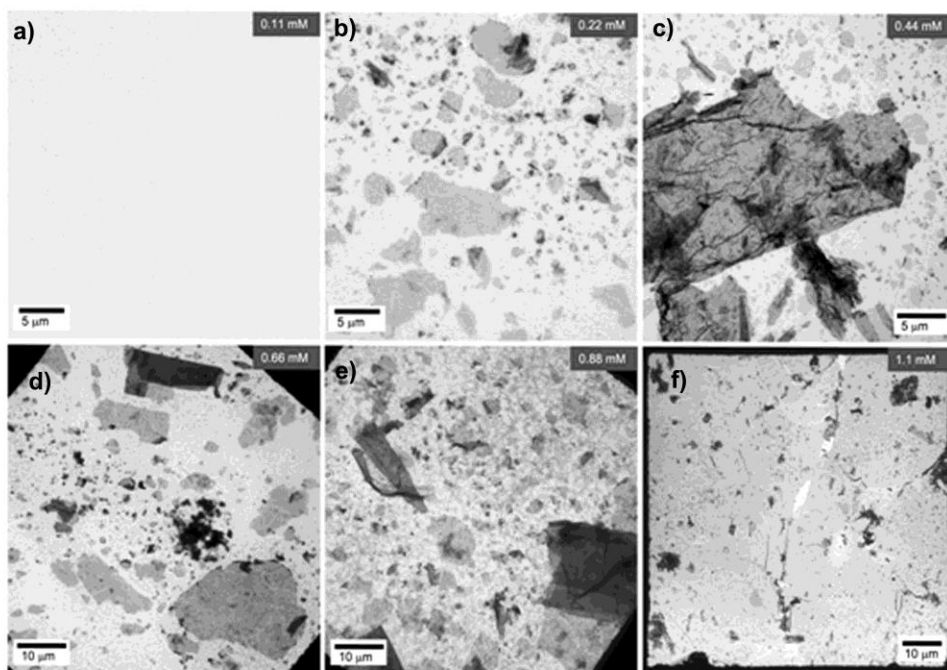
**Figure 19. TEM images of YYACAYY peptide film prepared from different concentration.** The faceted film was prepared from a) 0.11 mM, b) 0.22 mM, c) 0.44 mM, d) 0.66 mM, e) 0.88 mM, and f) 1.11 mM.

### 3.2.3. Peptide Nanofibers in Bulk Phase of Water Droplet

  Film formation of YYACAYY occurs only at the air/water interface, and might compete with fiber assembly inside the droplet. When TEM samples were prepared from a bulk YYACAYY solution that had already formed a film at the air/water interface, fibril nanostructures of ~15 nm in width were observed, indicating that nanofibers coexisted with the film. Tthe appearance-frequency of the film and the fiber according to the peptide concentration were shown in Figure 20c. The images were captured at various concentrations; 0.33, 1.1, and 1.43 mM, respectively. Based on these results, we could draw a simple plot for the appearance-frequency of the film and the fiber. The films were initially formed at 0.22 mM and its appearance-frequency increased as the peptide concentration increased. Above 0.44 mM, the film formation resulted in the faceting of the water droplet. The nanofibers were observed at the bulk phase of the droplet above 0.33 mM (Fig. 20b). It is supposed that the peptide has two pathways to be thermodynamically stabilized; film-prone pathway and nanofiber-prone pathway. The environmental condition seems to alter the conformation of the peptide, which is a key factor in determining the position-dependent polymorphism. At the interface, the hydrophobic tyrosine residues were forced to come together on one side of plane by forming helical conformation due to the presence of the air phase, and assembled into the film structure. At bulk phase, however, the peptides were assembled into nanofiber by forming β-sheet, because the tyrosine groups are differently oriented in the bulk phase. The nanofibers were initially observed at peptide concentration of 0.33 mM,

and their population increased as the concentration was increased.
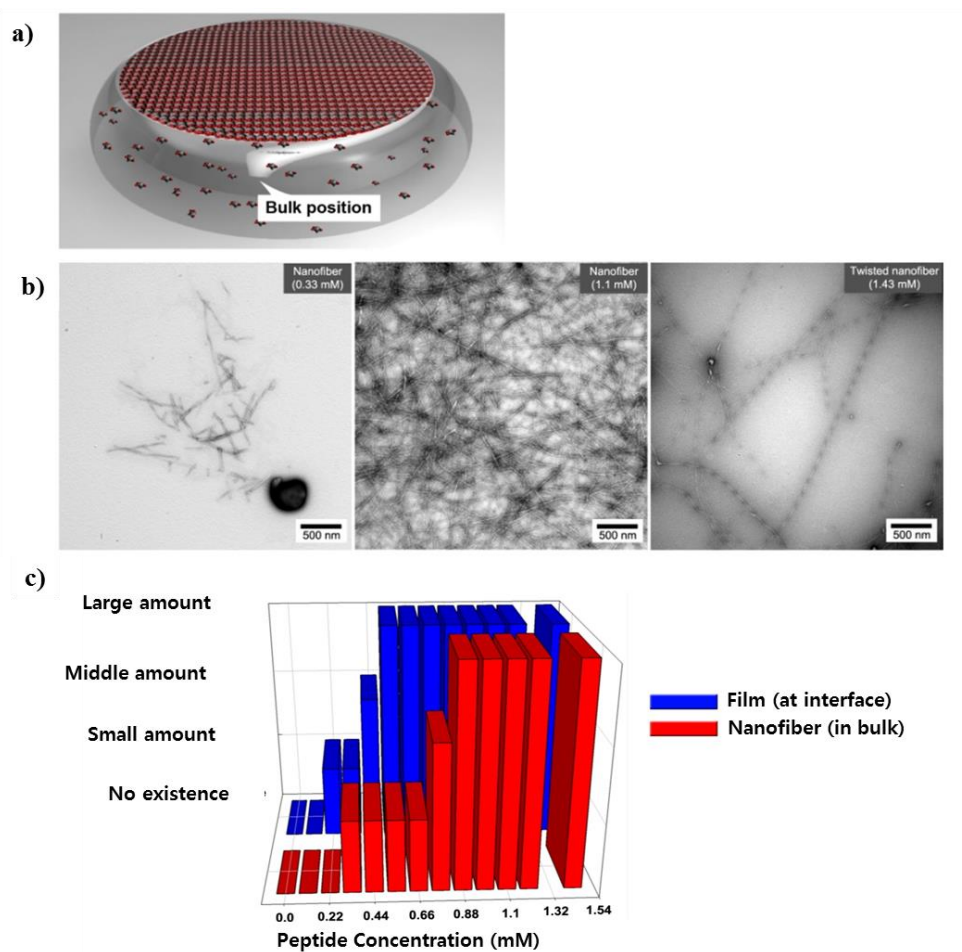
**Figure 20. Nanofibers at bulk phase of YYACAYY droplet.** a) Nanofibril formation at bulk phase. b) TEM of nanofibril from bulk position. c) Tendency of film/nanofiber formation according to the peptide concentration.

### 3.2.4. Atomic Force Microscopy Image of Peptide Film

Faceting was the result of peptide film assembly at the air/water interface, as shown by atomic force microscopy (AFM). The AFM data showed that the film was very flat and uniform (Fig. 21) The peptide film is uniform and smooth with a typical thickness of between 320 nm and 365 nm. As the time went by, the thickness of the film increased to ~400 nm . For the AFM imaging, 80 µl of peptide solution was dropped on a siliconized glass and incubated for 30 min. After the facet formation, the film at the interface was carefully transferred to a mica, and washed with distilled water to remove the buffer salts for clear images.

Individual YYACAYY peptide films were composed of multiple vertically stacked thin nanosheets. AFM analysis along the film edges showed evidence of nanosheet stacking (Fig. 22c) and grow thicker with time dependency (Fig. 22d). A minimum thickness of single sheet is 1.4 nm (Fig. 22a); these 1.4 nm-thick nanosheets were also observed at an early stage of film growth at low peptide concentrations(1.5mM) (Fig. 22b). We expect that the presence of facet and sharp edges might indicate a very high degree of molecular ordering occured.
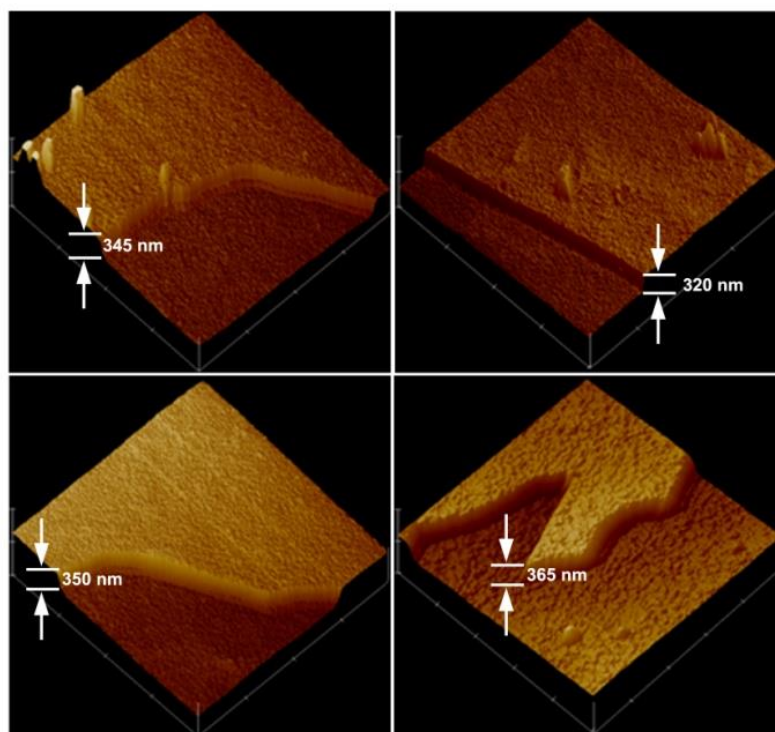
**Figure 21. Atomic force microscopy (AFM) image of YYACAYY facet.**
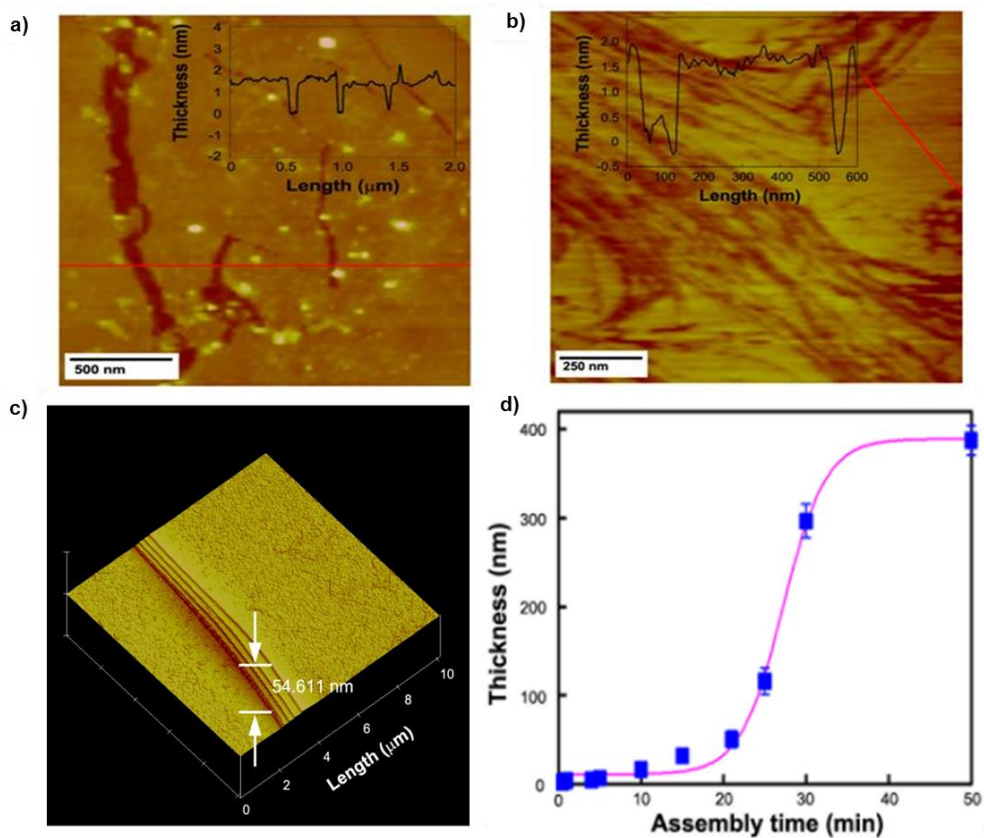
**Figure 22. AFM images of thin sheets of YYACAYY film and their stacking.** a) AFM image of single peptide sheet which clearly shows the thickness of 1.4 nm. b) The thickness of single peptide sheet at low concentration. c) The images of peptide films stacking. d) The plot of the peptide film thickening as a function of assembly time.

### 3.2.5. Fluorescence Image of Peptide Film

Distinct film structures can be observed by ThT staining as shown in Figure 23. Fluorescent image shows the result of peptide film assembly, which leads to faceting at the air/water interface, covering the whole area. The actual stained film was cut into multiple pieces during the transfer process to the slide glass (Fig. 23).
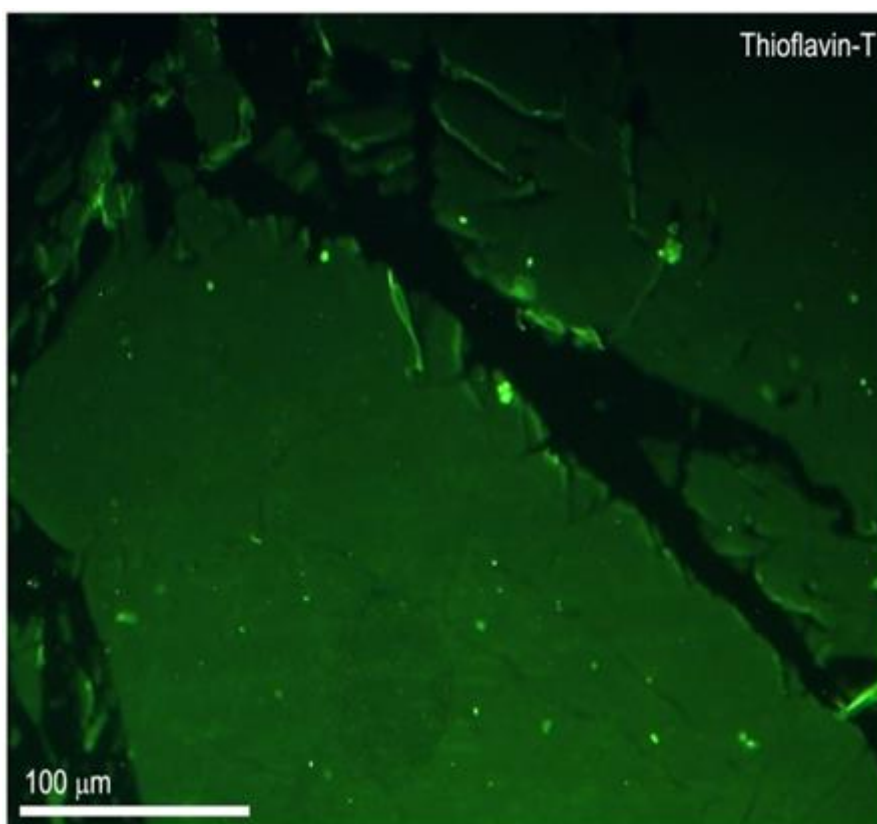
**Figure 23. Fluorescence image of YYACAYY film stained by thioflavin-T (ThT).**

### 3.2.6. Self Repairing Properties of Peptide Film

  The peptide film presented in this study exhibits self-repairing properties (Fig. 24). Due to the high surface tension of a water droplet, the facet was broken during the film forming process as shown in the image at 17 min (Fig. 24a). The damaged region was quickly repaired as the self-assembly proceeded, and the facet was fully recovered as shown in 26 min image (blue dashed circles) (Fig. 24a). When artificial defect was made by a needle, the facet was self-repaired within 10 min. As can be seen in Figure 24b, the defects or cracks introduced intentionally by a needle was also repaired spontaneously in 10min.
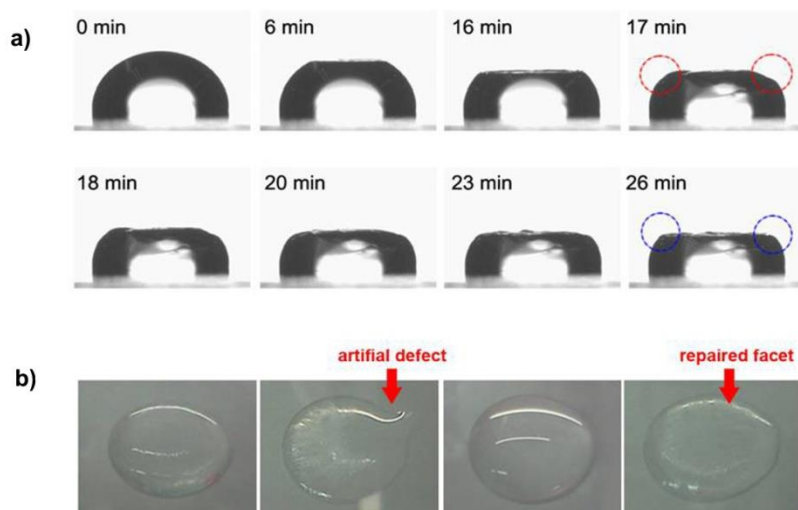
**Figure 24. Self-repairing property of YYACAYY film during facet formation.** a) The broken facet was repaired spontaneously. b) The artificially broken facet was repaired spontaneously.

### 3.2.7. Circular Dichroism and FT-IR Spectra of Peptide Film

The circular dichroism (CD) (Fig. 25a) and FT-IR (Fig. 25b) data confirmed that it has a helical conformation. Peptide monomer (black line) exhibited a broad peak at 225 nm indicating a helically folded structure when poly-tyrosine exists in a short peptide sequence[125]. No difference was observed between peptide monomer (black line) and film (red line). We guess that it might be resulted from a reversible dissociation of the peptide from order-packed facet at a low concentration for CD analysis. According to a Fourier transform infrared (FT-IR) analysis, the film formation of YYACAYY was accompanied by a conformational change. In particular, the bands at 3148, 1373, 1240 and 1172 cm$^{-1}$ were decreased and red shifted, indicating that the electrons of the phenyl group were delocalized. This result reflects $\pi$-$\pi$ stacking between adjacent tyrosine residues during film formation. The increased peak intensities at 2928, 2868, 1450 and 1286 cm$^{-1}$ indicated that the side chain of alanine residues and the peptide backbone were screened from the polar solvent environment when the peptides were aligned into an ordered architecture. The monomers exhibited a band at 1651 cm$^{-1}$, indicating an helical conformation[126] (Table 2).
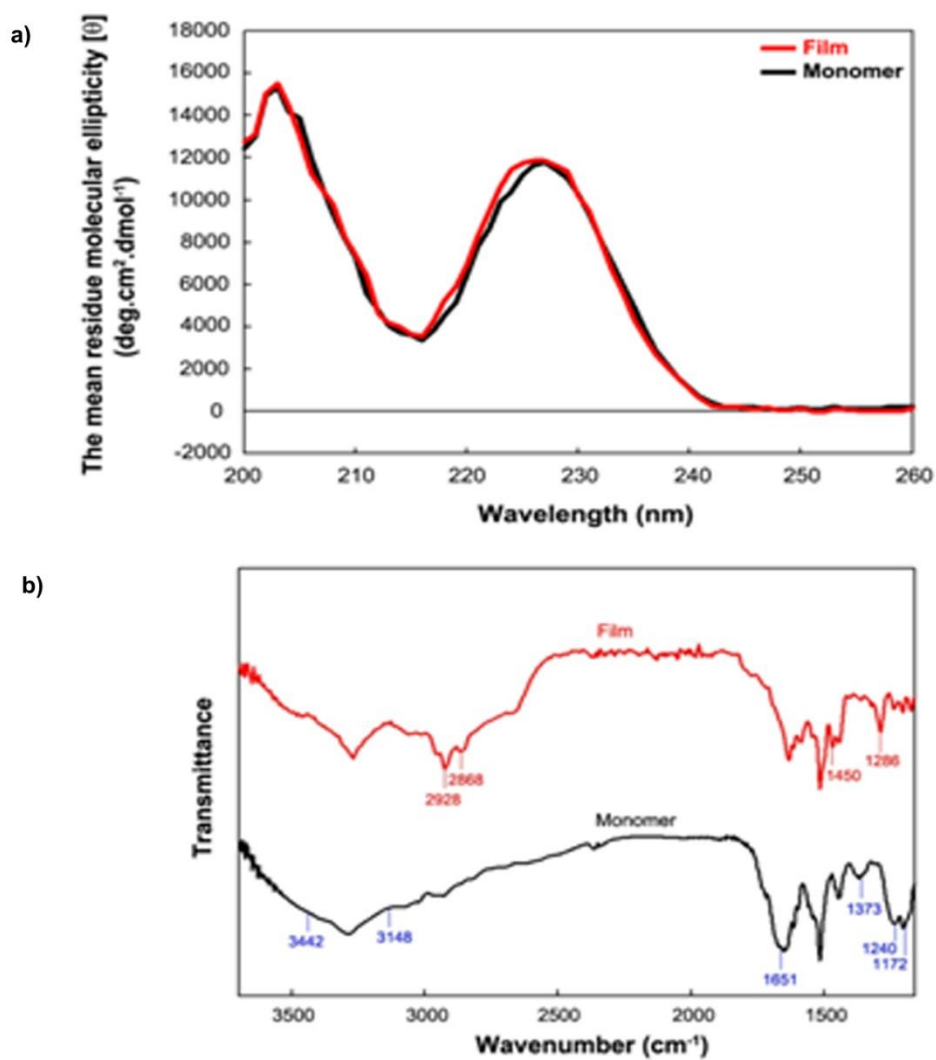
**Figure 25. Circular dichroism (CD) and FT-IR spectra of YYACAYY peptide monomer and peptide film.**

**Table 2. Assignments of the Bands in the Fourier Tansform Infrared (FT-IR) Spectroscopy Data of Peptide Film[127-133]**

| No. | Wavenumber (cm$^{-1}$)$^a$ | Vibrational assignments$^b$ | Spectral transition for film formation |
|---|---|---|---|
| 1 | 3600-3000 vb | ν(H-bonded OH of phenyl) | Decrease |
| 2 | 3148 m | ν(C-H of phenyl) | Decrease |
| 3 | 2928 s | ν(C-H of alanine) | Increase |
| 4 | 2868 s | ν(C-H of alanine) | Increase |
| 5 | 1690 s | Amide I, antiparallel β-sheet | Increase |
| 6 | 1651 s | Amide I, ν(C=O) | Decrease |
| 7 | 1580 w | C=C aromatic stretching | Increase |
| 8 | 1542 vw | Amide II, ν(C-N) | Decrease |
| 9 | 1450 m | δas(CH$_3$ of alanine) | Increase |
| 10 | 1373 b | Tyrosine vibration | Decrease |
| 11 | 1286 m | ν(C-N of primary amine) | Increase |
| 12 | 1240 w | -OH bending mode of tyrosine | Decrease |
| 13 | 1172 w | Ring CH bending mode of tyrosine | Decrease |

$^a$ vb: very broad; b: broad; s: strong; m: medium; w: weak; vw: very weak

$^b$ ν: stretching vibration; δas: asymmetric bending

## 3.2.8. Analysis of Peptide Film by HPLC-ESI and MALDI-TOF Mass Spectrometry

Disulfide bonding and the subsequent dimerization of YYACAYY seem to be critical for facet formation. Electrospray ionization (ESI) mass and matrix-assisted laser desorption/ionization (MALDI) mass spectrometry showed that the dimerization of YYACAYY occurred during film assembly (Fig. 26). We assigned the peak at 8.78 min as peptide monomer (purity: < 97%) which was confirmed by the mass data (915.9) before the peptide assembly (Fig. 26a). After peptide assembly at the air/water interface, a new peak at 10.88 min appeared, which was assigned as peptide dimer by the mass data (1830.5) (Fig. 26b). This result indicates that disulfide bond exists in the peptide films. After the peptide assembly at air/water interface, we could observe the dimerized peaks of YYACAYY as well, which is the evidence for crosslinking by cysteins. To confirm the existence of disulfide-bridge in the peptide film, we added dithiothreitol (DTT) solution to the peptide film, and found that the dimer peaks disappeared (Fig. 26c). From these results we confirm that the disulfide bridges are essential for the formation of peptide 2D structures.
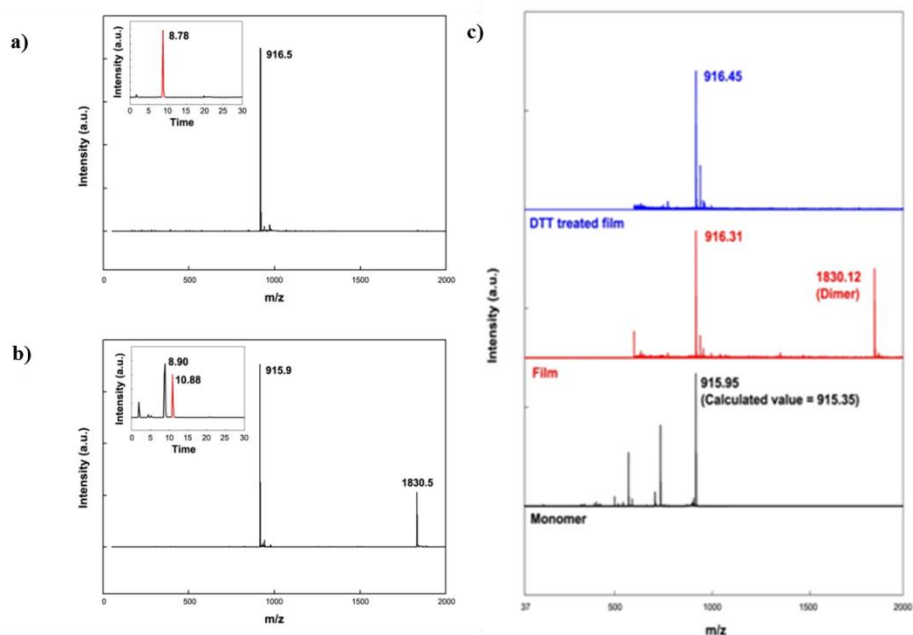
**Figure 26. The HPLC-ESI and MALDI-TOF mass data of YYACAYY monomer and peptide film.** a) HPLC-ESI mass data of YYACAYY monomer. b) HPLC-ESI mass data of YYACAYY dimer. c) MALDI-TOF mass data of YYACAYY film after DTT treatment.

### 3.2.9. Analysis Peptide Film by Raman Spectroscopy

Raman spectra confirmed that this dimerization was due to disulfide bonding between two cysteines. The Raman spectra of monomeric peptides (black line) and films (blue line) were shown in Figure 25. A signal at 2568 cm$^{-1}$ (the –SH stretching vibration), which was observed in the peptide solution before assembly, disappeared after film formation, and a new signal appeared at 503 cm$^{-1}$, which corresponds to the S–S stretching frequency (Fig. 27 and Table 3). Tyrosine peaks are indicated with a star (*). The peak at 503 cm$^{-1}$ and 2568 cm$^{-1}$ indicates disulfide (-S-S-) and sulfhydryl (-SH) group respectively.
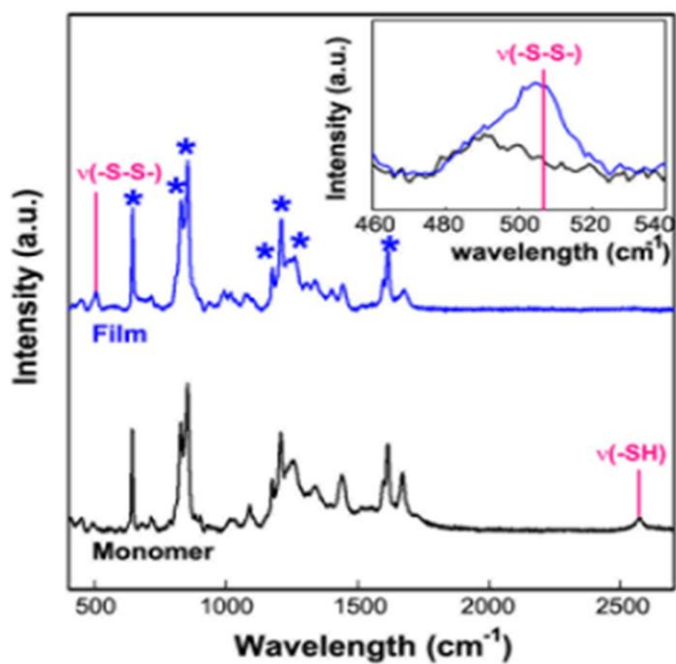
**Figure 27. Raman spectra of YYACAYY monomer and peptide films.** The Raman signal over the range of 460-540 cm$^{-1}$ is enlarged (inset).

**Table 3. Assignments of the Bands observed in the Raman Specta[134].**

| No. | Wavenumber (cm$^{-1}$) | Vibrational assignments[a] | Spectral transition during film formation |
|---|---|---|---|
| 1 | 447, 450 | $\nu$(H-bonded OH of phenyl) | - |
| 2 | 504 | $\nu$(S-S of Cys-Cys, disulfide bond) | Increase |
| 3 | 642 | Tyr | - |
| 4 | 715 | Tyr | - |
| 5 | 827, 852 | Tyr, $\nu$(Tyr ring breathing) | - |
| 6 | 1073, 1088 | $\nu$(C-C, C-N, C-O) | - |
| 7 | 1174 | Tyr | - |
| 8 | 1205, 1207 | Tyr | - |
| 9 | 1247, 1259 | Amide Ⅲ, random , $\nu$(Tyr ring-O stretching) | - |
| 10 | 1338, 1341 | CH$_2$ deformation | - |
| 11 | 1439, 1442 | CH$_2$, CH$_3$ deformation | - |
| 12 | 1594, 1596 | $\nu$(NH$_3^+$ bending) | - |
| 13 | 1612, 1613 | Tyr ring stretching | - |
| 14 | 1669, | Amide I, $\beta$-sheet | - |
| 15 | 1676 | Amide I,random, $\beta$-space | |
| 16 | 2570 | $\nu$(-SH of cystein) | Decrease |

[a] $\nu$: stretching vibration

### 3.2.10. The Importance of Dimerization on Facet Formation

The evidence for disulfide bond formation can be found from the disassociation of dimers into monomers with the addition of dithiothreitol (DTT). Various concentration of β-mercaptoethanol was added to the peptide solution (1.1 mM) and the reaction times of facet formation to reach 2 mm in diameter were compared. The kinetic data clearly showed that the addition of β-mercaptoethanol decreased the kinetics of the facet formation in concentration dependant manner. The fact that β-mercaptoethanol addition decreased the faceting kinetics demonstrates the importance of disulfide bonding in assembly (Fig. 28). From experimental results with cysteine-replaced sequences, such as YYAEAYY and YYAKAYY, we verified that disulfide bonding is essential for peptide film formation and subsequent faceting. Although YYAEAYY and YYAKAYY can form much thinner films than YYACAYY, these motifs never produce a facet. We also added DMSO to the peptide as an oxidant to induce disulfide bonds formation. YYACAYY was dissolved and stored in DMSO for 3 days to generate dimerization. After DMSO was removed by lyophilizer, fully dimerized YYACAYY peptide was obtained as a powder form, which was confirmed by HPLC and Raman spectroscopy (Fig. 29). The YYACAYY dimmer was mixed with YYACAYY monomer in ratios of 1:9 to 9:1. We observed that the facet formation started to occur from the ratio of 5:5 and the rates were accelerated as the dimer ratio was increased (Fig. 30). These results suggest that disulfide bridges are involved in film thickening and thus, provide sufficient mechanical strength to overcome the high surface tension of water droplet.
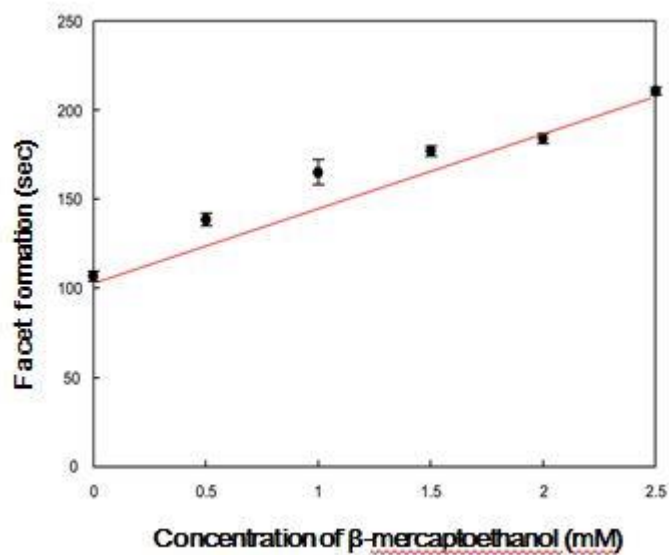
**Figure 28. The effect of reducing agent on facet formation.** Various concentrations of β-mercaptoethanol was added in to the peptide solution (1.1 mM). The data were collected from at least three experiments.
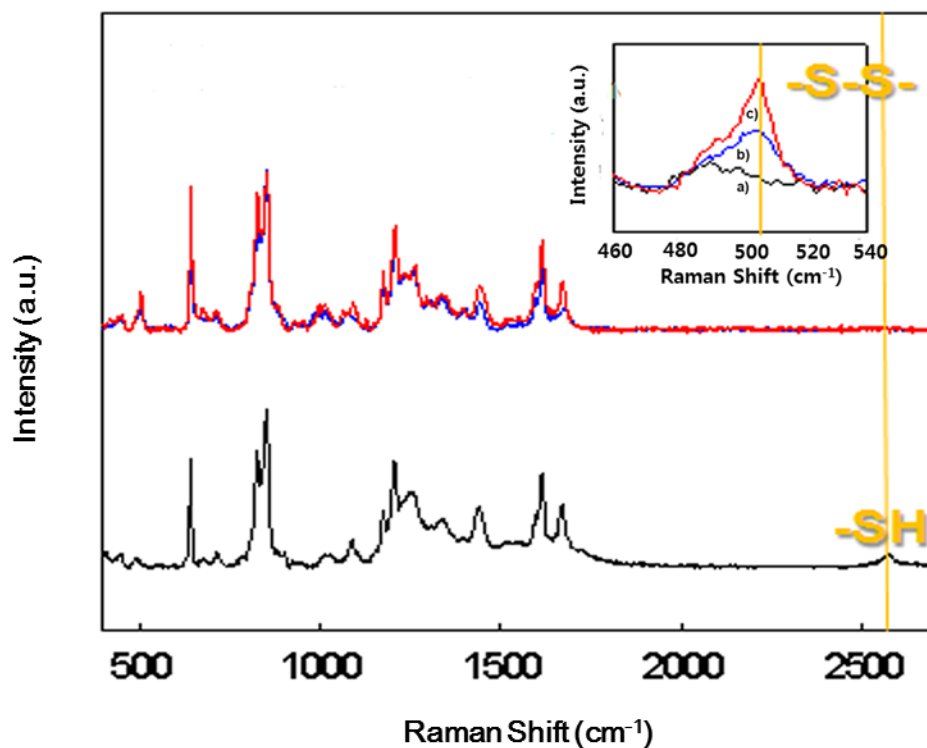
**Figure 29. Raman spectra of YYACYY monomer and the dimer.** The sharp disulfide peak at 502 $cm^{-1}$ was confirmed by adding DMSO as oxidant. a) YYACAYY peptide monomer, b) Faceted YYACAYY peptide, c) DMSO oxidaized YYACAYY peptide dimer.
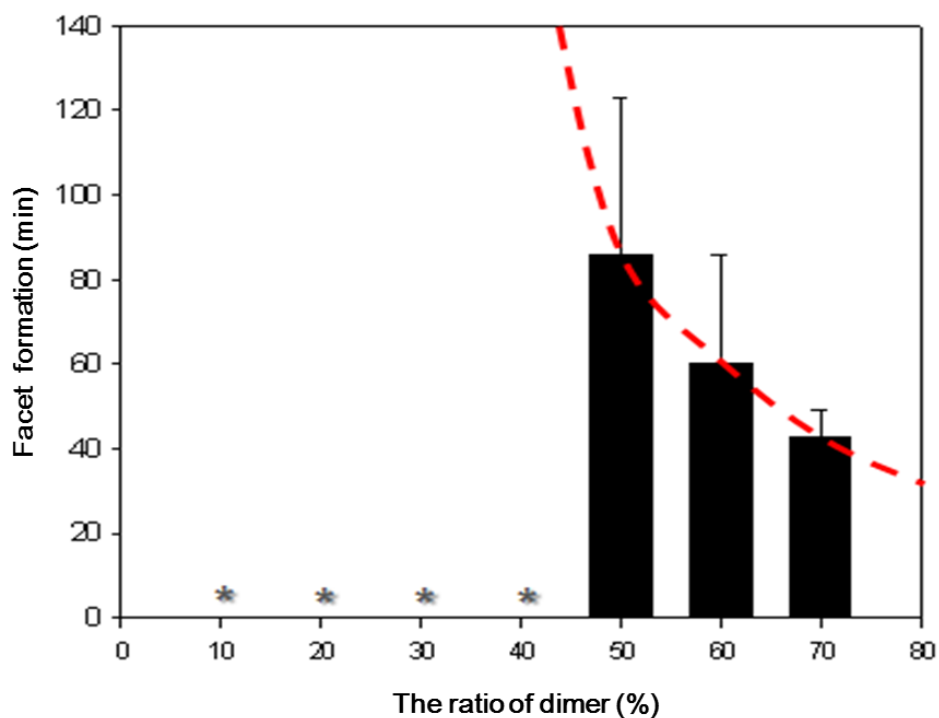
**Figure 30. Kinetics of facet formation with mixture of YYACAYY monomer
and dimer.** The facet did not form until the dimer existed above 50% (*).
The kinetics for facet formation was accerlerated as the dimer ratio was
increased.

### 3.2.11. X-ray Diffraction Analysis of Peptides Film

Assembled films were collected and dried as a powder for X-ray diffraction (XRD) analysis shows that the peptide film is crystalline (Fig. 31), although the film is not a single crystal, an exact crystal structure could not be determined at the atomic level. The large, intense peak at 13.5 Å appears to be the result of the layer thickness, which is close to the typical 14.0 Å that is also observed for the thinnest layer in the AFM analysis. The enlarged XRD pattern in the 2θ range of 13-56 is displayed in inset. A structural analysis was carried out by making comparisons with previously known protein spacings and matching those data with our folding computations. The diffraction at 6.8 Å may correspond to the distance of $C^{\alpha}$-$C^{\alpha'}$, the distance between cysteine residues of the YYACAYY dimer bridged by a disulfide bond ($C^{\alpha}$-$CH_2$-S-S-$CH_2$-$C^{\alpha'}$). The 4.8 Å spacing may indicate the intermolecular distance between two YYACAYY molecules, and this value is similar to the distance of the edge-to-face configuration (4.9 Å) between π-clouds of tyrosine-tyrosine systems in proteins[135]. The 3.4 Å spacing is the diameter of an α-helical strand along the backbone direction.
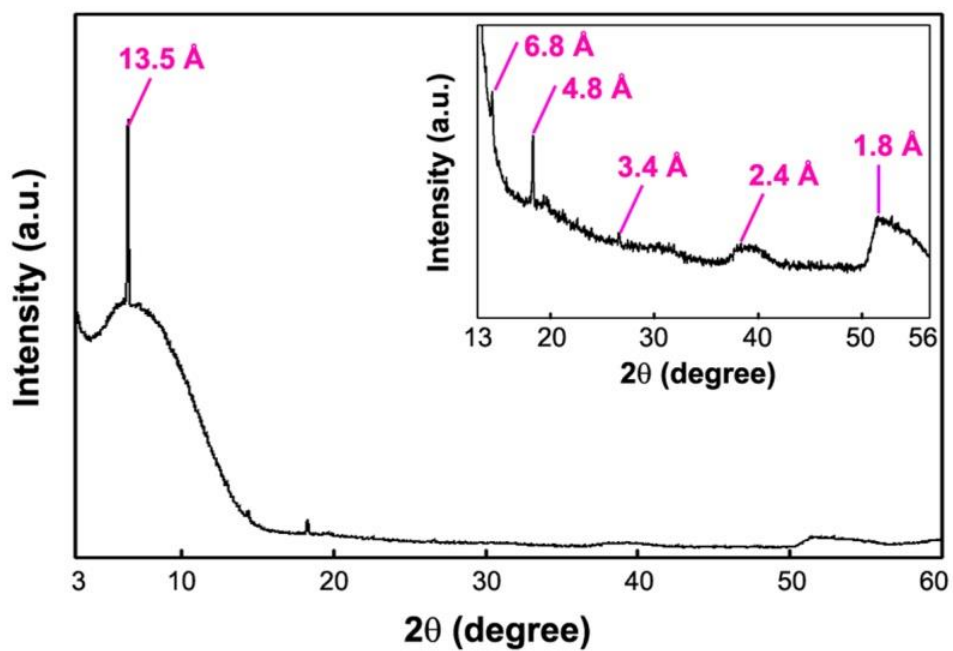
**Figure 31. X-ray diffraction analysis of YYACAYY peptide film.** The 4.8Å corresponds to the distance of edge to face π-π stacking. 2.4 Å and 1.8 Å corresponds to the distance of hydrogen bonds.

### 3.2.12. Molecular Mechanism Study for Peptide Film Formation

Along with π-π interactions between tyrosines and disulfide bond formation between cysteines, the intrachain structure of the peptide plays an important role in assembly. The folding details and underlying molecular mechanism were investigated using the CHARMm force field in Discovery Studio (Accelrys Inc.). A computational study on YYACAYY showed that the helical structure is the most stable conformer. In the simulated structure, the four phenolic ring groups were located on one side, and the hydrophilic cysteine was on the other side (Fig. 32b). Such folding symmetry is likely to cause peptides to float at the air/water interface. According to the simulation data, the helical structure of each monomer was maintained even after forming YYACAYY dimer (Fig. 32c). The height of each dimer was approximately 1.4 nm (Tyr2 to Tyr6′) (Fig 32c and Fig. 33). This value was close to the smallest thickness (1.4 nm) observed in the AFM analysis, strongly suggesting that the dimers acted as building blocks. Additionally, the observed 6.8, 4.8 and 3.4 Å spacings observed through X-ray diffraction were visualized in the simulated structure (Figs. 33 and 34). One interesting feature of the simulated dimer structure is the symmetric arrangement of eight tyrosine groups along the vertical and lateral directions (Fig. 32c). The direction in which Tyr2 and Tyr6 point is almost perpendicular to that of Tyr1 and Tyr7, and Tyr1 and Tyr7 are aligned with an orientation that adopts edge-to-face π-π interactions with neighboring dimers (Fig. 34). In addition, when we added 150 mM sodium chloride (NaCl) to the peptide solution to reduce the Coulomb interaction between the peptides in solution, the

facet formed at a similar or even faster rate. Taken together, we believe that this edge-to-face interaction is a more dominant factor than the electrostatic interaction in 2D peptide film formation. To determine the effect of terminal groups, we replaced the C-terminus with an amide or acetylated the N-terminus. In both cases even though the facet was still formed, the kinetics became slower.
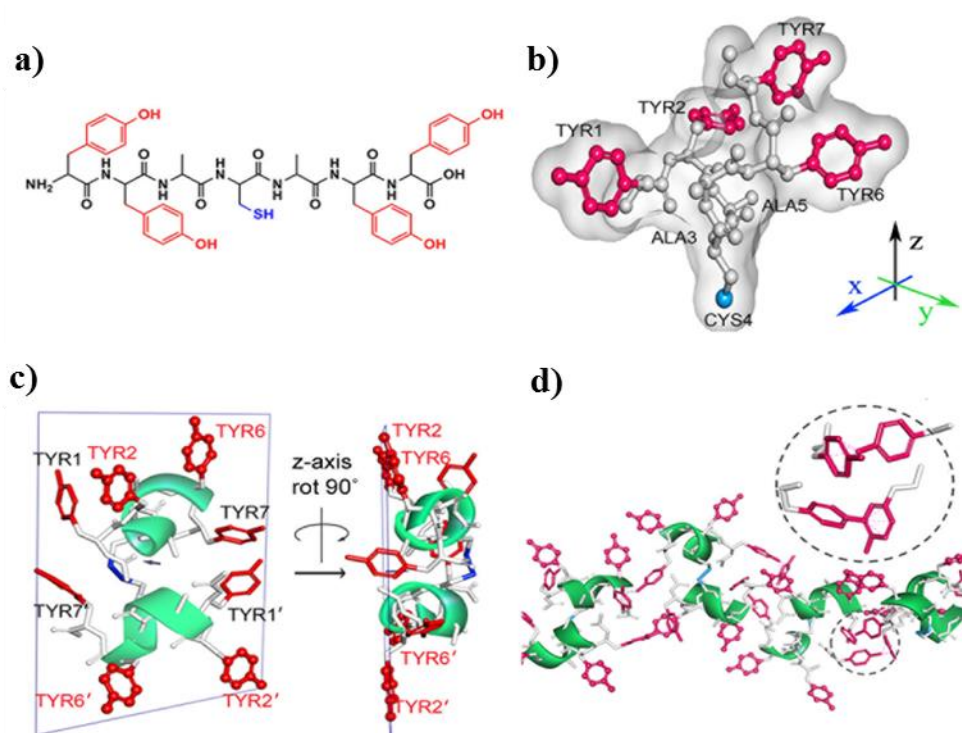
**Figure 32. Computational study of the YYACAYY structure and assembly mechanism**. a) Molecular structure of YYACAYY peptide. b) The structure of YYACAYY peptide after 500-ps molecular dynamics of lowest energy level. c) Dimerization of two YYACAYY momoners. d) Lateral π-π stacking of YYACAYY peptide.

As shown in Figure 32c, the plane of two Tyr2s (Tyr2s and Tyr2s') and two Tyr6s (Tyr6s and Tyr6s') is located perpendicularly to the plane of Tyr1s (Tyr1s and Tyr1s') and Tyr7s (Tyr7s and Tyr7s'). The neighboring four dimers are associated by tyrosine-mediated π-π stacking interactions, resulting in a continuous structure of stacked nanosheets. The portion shown in dotted lines was magnified for a closer view of the edge-to-face interaction of Tyr1 and Tyr7. Tyr2 and Tyr6 are represented by a ball-and-stick model (Fig. 32d). Laterally packed double dimers are shown in Figure 33. In the XRD data, the peak at 13.4 Å indicates the height of the dimer, which is close to the height of thinnest sheet observed by AFM. The peak at 6.8 Å indicates the distance from the $C^{\alpha}$ of cysteine in the upper peptide to the $C^{\alpha}$ of cysteine in the lower peptide, which is the spacing between the two helical strands in the dimer. The diffraction at 3.4 Å is the diameter of the α-helical strand.

To understand how the peptides are laterally associated during the film formation, the geometry of the neighboring two dimers (YYACAYY – YYACAYY) was analyzed in detail in figure 34. Helical folding is shown in green and tyrosine residue in red. The blue color indicates the disulfide bonding in the dimers. Each monomer was named with A, B, C and D. When the first dimer (left, A B) packed closely to the second dimer (right C D), Tyr7 in the monomer A can be associated through face to edge interaction with Tyr1 in the monomer C. It applies the same with Tyr1' in the monomer B and Tyr7' in the monomer D. Tyr2 and Tyr6 are shown by a ball-and-stick model (Fig. 34).
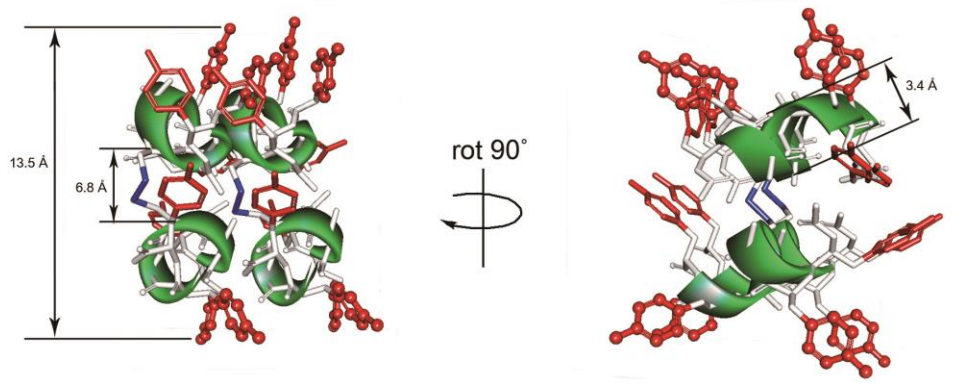
**Figure 33. Illustrative image of diffraction patterns of associated YYACAYY dimer obtained from XRD data.**
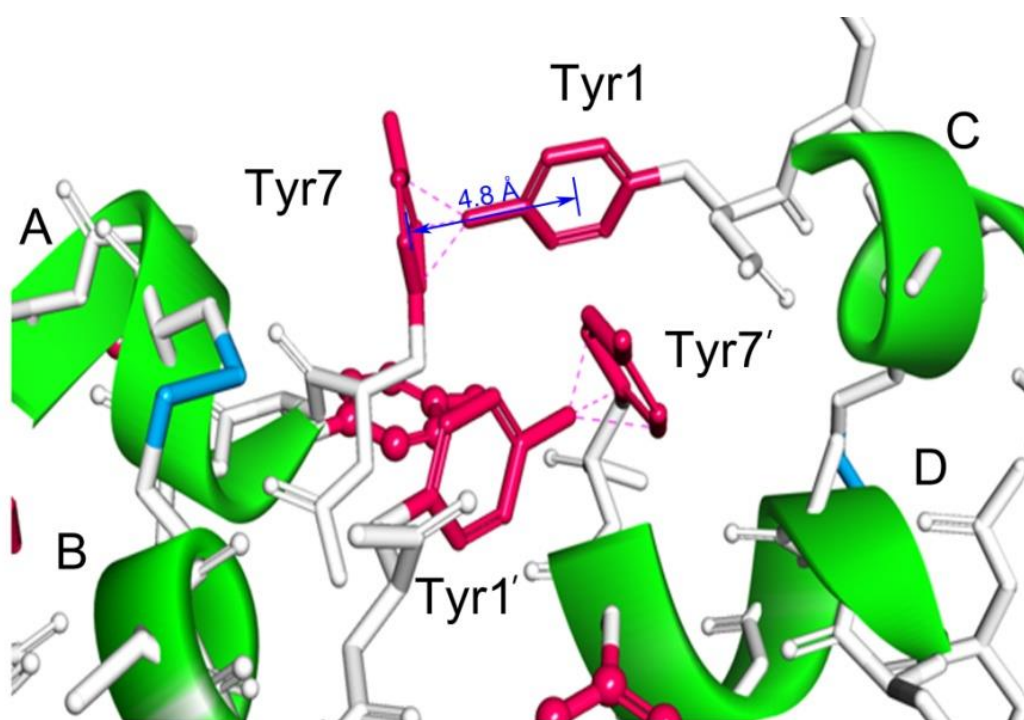
**Figure 34. Detailed structure of laterally associated YYACAYY peptides.**

The computational detail shows that the intramolecular hydrogen bonding between Cys4(HN)-Tyr1(O), Ala5(HN)-Tyr1(O), Tyr6(HN)-Tyr2(O) and Tyr7(NH)-Ala3(O) were 2.477, 1.911, 1.973 and 1.805 Å, respectively, which are similar to the spacings of 2.4 and 1.8 Å that were observed as broad peaks in the XRD spectra (Fig. 35). These distances are close to the spacings of 2.4 and 1.8 Å that were observed by X-ray diffraction. Simultaneously, peptides that are organized into a monolayer form disulfide bonds and construct a thin bilayer of 1.4 nm, and the at the relatively oxygen-rich interfac. A sulfhydryl (-SH) group, which is actually not very active for dimerization at a pH of 5, can be cross-linked by a disulfide bridge at the interface as a result of the proximity effect and the oxidative environment[136]. This dimerization creates an additional hydrophobic interface because the tyrosines at the bottom of the peptide bilayer inevitably face toward the water. Such an unfavorable situation induces the floating of peptides from the bulk solution to this hydrophobic surface. Then, the hydrophobic interaction and disulfide-bridged dimers create the next bilayers below the first layer. This repeated dimerization and stacking results in the growth of the film and leads to the propagation of faceting (Fig. 36). Likewise, the closed packed peptide scaffolds were assembled at air/water interface (Fig. 37). At air/water interface, the peptide monomers have a tendency to form a amphiphilic helical conformation. These amphiphilic helical peptides can float and closely pack each other on the air/water interface. The relatively oxygen-rich environment at the air/water interface facilitates disulfide bond formation. At the same time, the fibril formation was occurred in the bulk phase (Fig. 38).

In summary, we can conclude the mechanism of faceted film formation as follows

(1) YYACAYY has amphipathic conformation at air/water interface. They float and closely pack each other on the air/water interface.

(2) They are assembled into the peptide rafts at various positions on the surface of droplet and locally deform the topology of a water droplet. The differential evaporation of water molecules on curved interface results in a convection flow in the droplet, which moves peptide rafts to the top of the droplet.

(3) The peptide rafts move to the top of the droplet and their association and assembly initiate the film formation.

(4) The relatively oxygen-rich environment at the air/water interface facilitates disulfide bond formation.

(5) Then, the hydrophobic interaction and disulfide-bridged dimers create the next bilayers below the first layer. This repeated dimerization and stacking results in the vertical growth and lead to thick peptide film formation. The faceting a water droplet is achieved by the horizontal and vertical growth of the film at the top position.
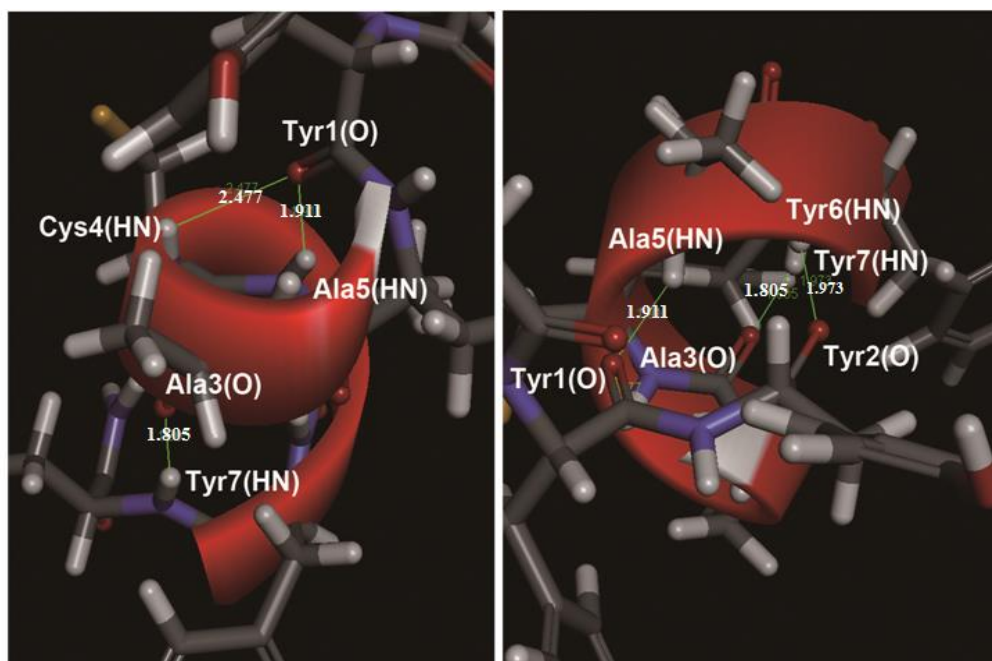
**Figure 35. Illustrative image of the hydrogen bonding distances within the peptide.**
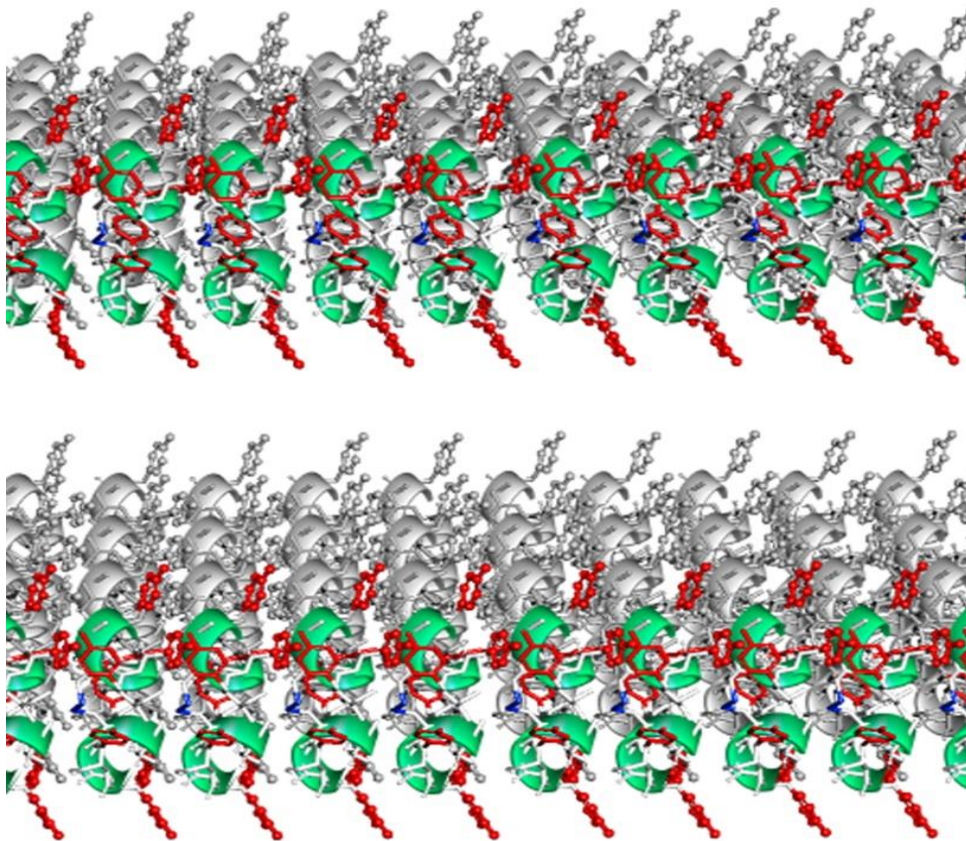
**Figure 36. Illustrative image of the overall structure of faceted film.**
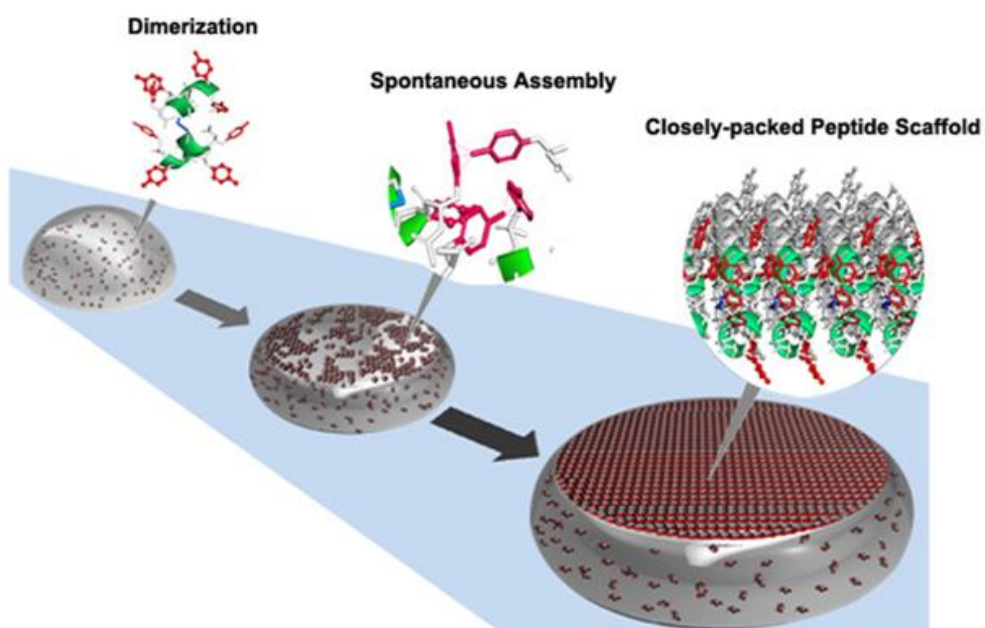
**Figure 37. Illustrative image of the overall scheme of faceted film formation.**
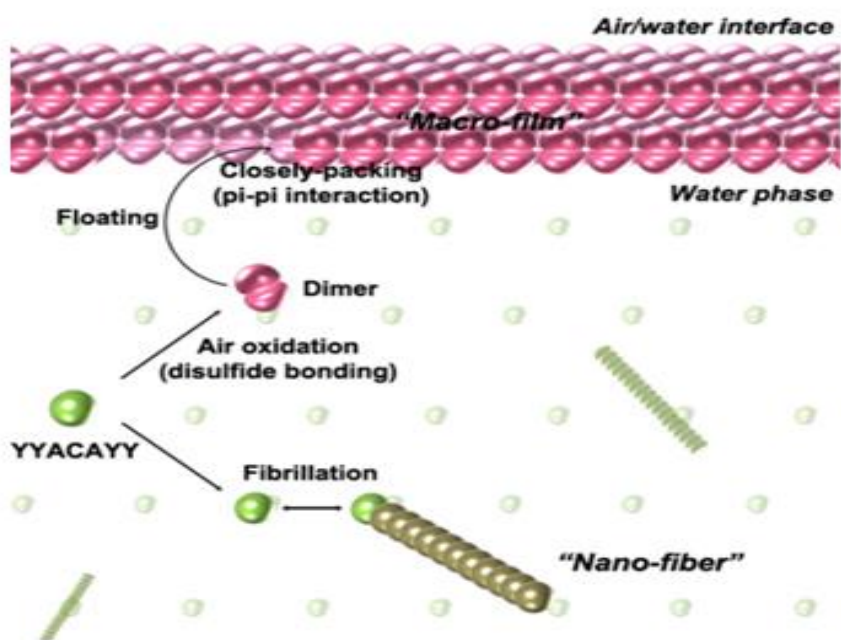
**Figure 38. Illustrative image of the overall mechanism of faceted film formation at air/water interface.**

### 3.2.13. Computational Study on the Conformation of Tyrosine Contaning Peptides

In an effort to link the macroscopic observations with the peptide sequences, we classified the assembled structures of seventeen peptides listed in Table 1 and identified the key motifs and geometries as morphology determinants. The sequences that did not form facets were classified into three groups: 1) YY, YYY, YYYY and YYAYY which do not float, 2) YCY and CYY, which float but did not form films, and 3) YYAEAYY and YYAKAYY, which float and form thin films. The assembly behavior can be understood at the molecular level by computational analysis. The four sequences that belong to the first group have only hydrophobic side chains. The second two sequences have spatially segregated hydrophobic and hydrophilic parts and are therefore able to float. However, the two tyrosine groups might not be in an adequate arrangement for lateral association. Molecular simulations show that YYAEAYY and YYAKAYY possess the amphiphilicity and folding is also favorable for tyrosine-mediated lateral interactions. However, because they don't have cysteine, the faceting did not occur. (Simulated data in Appendix)

### 3.2.14. Electrochemical Properties of Peptide Film

One potential application of tyrosine containing peptide film is to use as a redox active scaffold for developing an enzyme mimetic catalyst. We explored the possibility of whether tyrosine radicals generated in our peptide film were able to trigger or enhance the chemical reaction in a manner similar to that observed in many other biological systems. Therefore, we expected our peptide film to be a unique platform, as it is based on tyrosine units that allow easy interfacing with any underlying electrode and systematic study of the ordering and neighboring sequence effect. Figure 39a shows a cyclic voltammetry (CV) polarization curve for the YYACAYY film on FTO glass in 0.1 M NaCl electrolyte. The cyclic voltammetry curve (Fig. 39a) indicates that tyrosyl radicals can be easily generated from our peptide film by applying a potential of 0.9 V (versus NHE). Electrochemical oxidation of tyrosine (Tyr $\rightarrow$ Tyr●) resulted in a broad peak (*), with a maximum current at 0.9 V (versus NHE). To explore the possibility of using tyrosyl radicals in the film, we chose oxidative polymerization of pyrrole as a model reaction. Polypyrrole can be synthesized by applying a potential greater than 1.0 V or by using an oxidant, such as Fe(III) ions. Although polymerization can be initiated at approximately 0.9 V, according to previous reports[137], the rate at this potential is too slow to obtain macroscopic polypyrrole deposition. Indeed, as shown in blue line (Fig. 39b), our results confirmed that 0.9 V bulk electrolysis produced a negligible amount of polypyrrole deposition on a fluorine doped tin oxide (FTO) substrate. In contrast, when a constant potential of 0.9 V was applied to the YYACAYY film on

the FTO, the current density drastically increased to 68 μA after 300 sec and the black polypyrrole film was deposited continuously. Moreover, the YYACAYY peptide film on the FTO substrate was able to mediate the electron transfer from the pyrrole to the electrode and to lower the energy barrier for oxidative polymerization. The current density profiles of the YYACAYY peptide film and tyrosine monomer deposited on FTO substrates during bulk electrolysis are shown in Figure 39b. After 30 min of electrolysis, remarkably different kinetics in polypyrrole formation was observed, which was confirmed by the color change on the substrate.
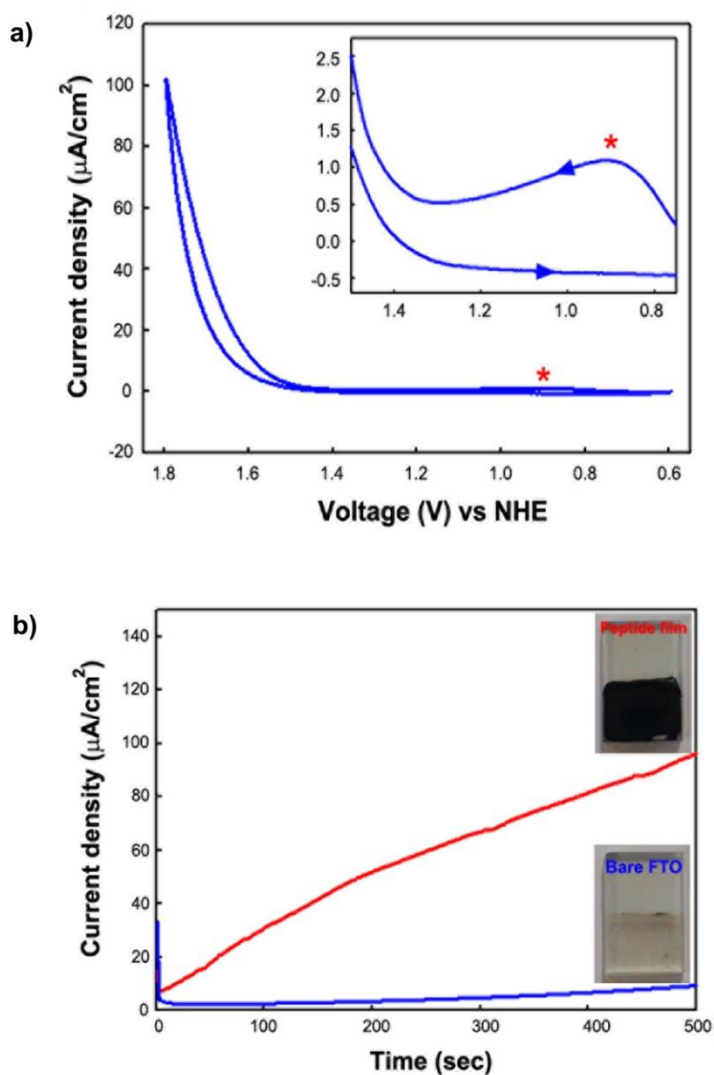
**Figure 39. Cyclic voltammetry (CV) polarization curve a), and current density profiles b) of the YYACAYY peptide film (red) and tyrosine monomer (blue).** The condition for bulk electrolysis of pyrrole (5mM) was 0.9 V in 0.1 M NaCl. The inset in b) shows the color change on the electrode when polypyrrole film was formed.

### 3.2.15. Electro Oxidative Properties of Peptide Film

Based on our study on the electrochemically driven tyrosyl radical generation, we designed an experiment to mimic an enzyme system, such as the above mentioned galactose oxidase, in which the radical is generated by a valence change of the copper(II) ion without applying any additional potential. We found significantly different activities of copper(II) ions to oxidize pyrrole into polypyrrole in the presence of the YYACAYY film. For the experiment, a peptide film was assembled in 4 mM copper (II) chloride aqueous solution and then exposed to pyrrole vapor. A black polypyrrole film gradually formed on top of the peptide film, and after an overnight reaction, a free-standing hybrid film of polypyrroles on peptides was obtained (Fig. 40). In contrast, neither copper (II) chloride aqueous solution nor copper (II) chloride aqueous solution with tyrosine monomer produced a polypyrrole film, even after a few days. These results show that the YYACAYY film allows the copper (II) ions to easily oxidize pyrrole, likely by tyrosyl radical mediated electron transfer. The fact that the polypyrrole film formed only at the air/peptide interface also supports the observation that electrons are transferred from vaporized pyrroles to copper (II) ions in solution through the YYACAYY film. We believe that the catalytic activity and selectivity can be further improved by the combination of the peptide sequence design and the structural alternations based on the YYACAYY platform. When the YYACAYY peptide was completely dissolved in 10 mM HEPES (pH 7.4) by brief sonication for 10 min. The peptide film and facet formation was more accelerated compare to the free standing peptide solution

in 50 mM HEPS buffer. When we remove the peptide film from this system, the kinetics of polypyrrole formation was decreased. Therefore, we assume that tyrosine peptide assembly is important for polypyrrole formation. We observed that the large polypyrrole/peptide film was suspended stably on air/water interface. The film assembled on the surface of water was able to induce the polymerization of pyrrole, which reached the air/peptide interface as a vapor in a closed system (vapor pressure 7 mmHg). The schematics of the proposed mechanism involving copper (II) ion reduction, tyrosyl radical generation and pyrrole oxidation is shown in figure 40. The copper (II) ion reduction in water spontaneously induced the formation of tyrosyl radical (Tyr●) without any additional oxidant or applied potential. We assume that Tyr● generates sulfhydryl radical from cysteine radical(Cys●), and this sulfhydryl radical initiates polymerization of pyrrole (Py) on YYACAYY peptide film scaffold. It is because when we exchange cysteine residue to histidine (YYAHAYY) or alanine (YYAYY), polymerization of pyrrole did not occur.
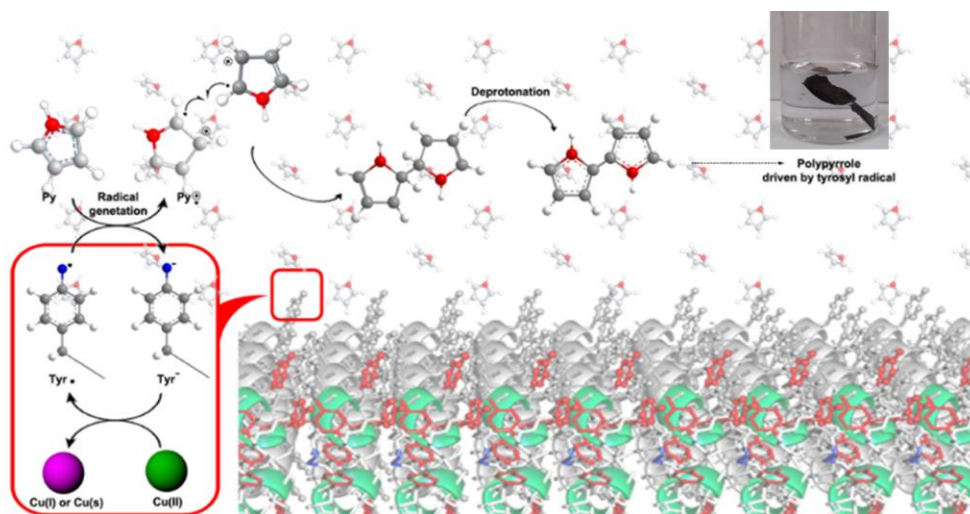
**Figure 40. Suggested mechanism of polymerization of pyrrole on redox active YYACAYY peptide film.**

## 3.3 Tyrosine Peptide–Polypyrrole Supported Palladium Catalyst

### 3.3.1. Preparation of Tyrsine Peptide–Polypyrrole Supported Palladium(II) Catalyst (Tyr peptide@PPy@Pd Catalyst)

The tyrosine peptide (YYACAYY) was completely dissolved in 10mM HEPES buffer (pH 7.4) by brief sonication for 10 min and heating at 90°C for 30 min in a closed system. After heating process, palladium(II) ion (sodium tetrachloropalladate(II) hydrate, 2-4 equiv.) was addd directly to the peptide solution. The peptide solution containing palladium ion was placed on a siliconized glass surface (Hampton Research, HR3-231) using a pipette. And, 1ml of neat pyrrole monomer drop was placed near the peptide-palladium ion solution. On the surface of peptide solution pyrrole monomer started to polymerize in few minutes. We can observe the peptide drop was slightly covered by polypyrrole. After 2 hours, the polypyrrole coated peptide film containing palladium nanoparticle was collected and washed by water to obtain Tyr peptide-polypyrrole supported palladium (Tyr peptide@PPy@Pd Catalyst) catalysts. We found that the Tyr peptide@PPy@Pd catalysts exhibited good catalytic activity even with small amount of the catalyst (0.2~1.5 mmol%) in C-C cross-coupling reaction with aryl boroic acid in water at 50°C. Thus we systematically tested the activity of Tyr peptide@PPy@Pd catalyst for Suzuki coupling reaction which was chosen as one of representative cross-coupling reactions (Fig. 41).

**Tyrosine-Pd(II) Hybrid 2D Scaffold**

HEPES Buffer: 10mM
YYACAYY: 2mM
Palladium: 0.1 mmol %

Incubation on a chamber

Pyrrole monomer

Pyrrole monomer

Polypyrrole-supported tyrosine mediated Pd catalyst Coated on Surface

washing & collecting

**Tyr-Pd Catalyst**
Tyrosine-Pd immobilized on Polypyrrole sheets

**Homogeneous Tyrosine induced Pd nanoparticles**
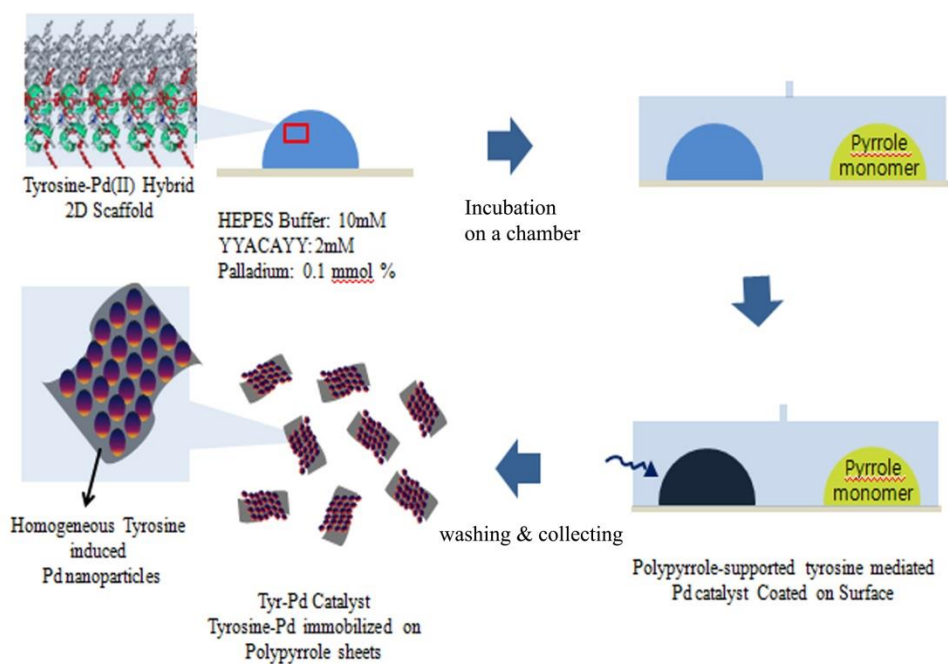
**Figure 41. Schematics of the preparation of Tyr peptide@PPy@Pd catalyst.**

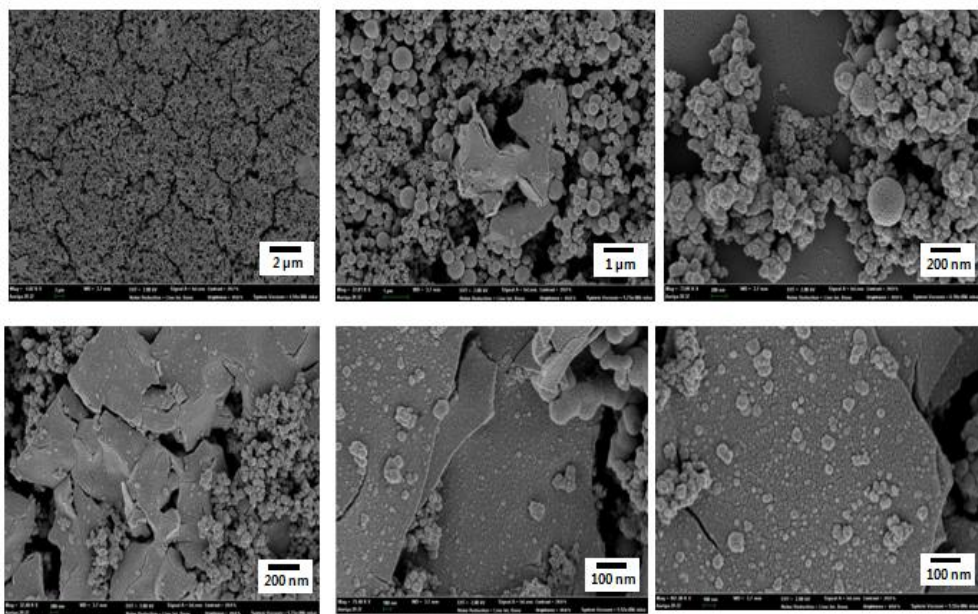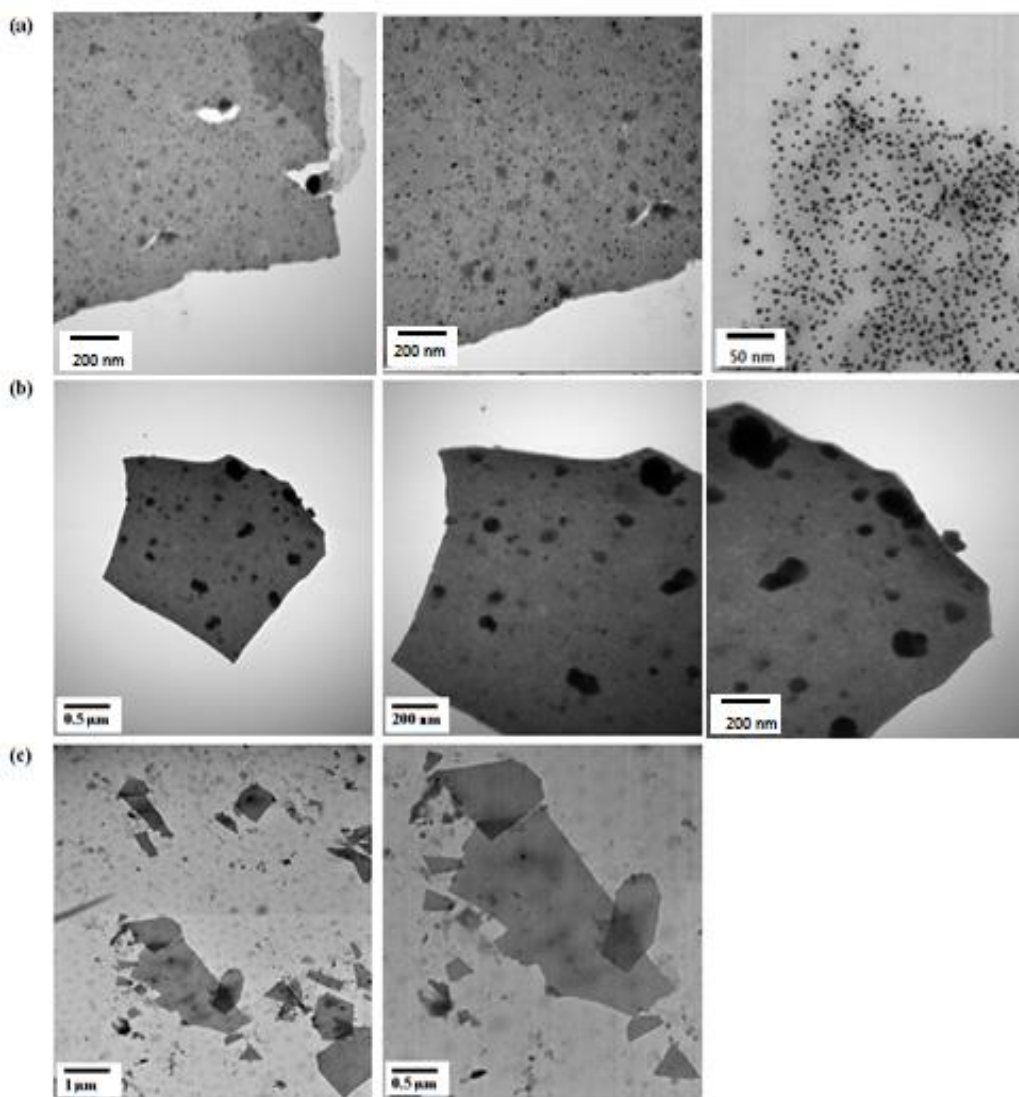**3.3.2. Characteristics of Tyrosine Peptide−Polypyrrole supported Palladium(II)**

   **Catalyst**

The tyrosine peptide−polypyrrole supported palladium catalysts (Tyr Peptide@PPy@Pd catalyst) were analyzed by FE-SEM to observe the surface morphology. The FE-SEM images exhibited clear surface morphology of the Tyr Peptide@PPy@Pd catalyst without any physical damages during the synthesis (Fig. 42). We can observed that homogenous Pd nanoparticles (4~5 nm) were immobilized evenly on polypyrrole sheets. When the tyrosine peptide was not used during fabricating process of the Pd catalysts, the particle size distribution of palladium nanoparticles were not homogenous, and the attached palladium nanoparticles were easily fall off after the first C-C coupling reaction (Fig. 43). From this, we can conclude that tyrosine peptide might help palladium nanoparticles to be attached on polypyrrole supports. The existence of Pd on the polypyrrole sheets was verified by the detection of Cl and Pd atoms from EDX analysis. The existence of S atom was also identified from EDX spectra (Fig. 44a). The oxidation states of Pd nanoparticles in the Tyr Peptide@PPy@Pd catalyst were determined by XPS. The Pd peak at 336.8 eV corresponds to (Pd $3d_{5/2}$, Pd $3d_{3/2}$), and the one at 342.5 eV corresponds to Pd(II)[138,139] (Figure 44b) (The reference data profile is the Appendix). The amount of immobilized Pd on the PPy-Tyr-Pd catalyst quantified by ICP-AES was 0.34 mmol/g.

**Figure 42.** Field emission scanning electron microscopic (FE-SEM) images of Tyr peptide@PPy@Pd catalysts.

**Figure 43. Transmission election microscopic (TEM) images of Tyr Peptide-polypyrrole supported palladium catalyst.** a) Images of Tyr Peptide@PPy@Pd catalysts before the C-C coupling reaction; b) Images of PPy@Pd catalysts before the C-C coupling reaction; c) Images of PPy@Pd catalysts after the C-C coupling reaction.
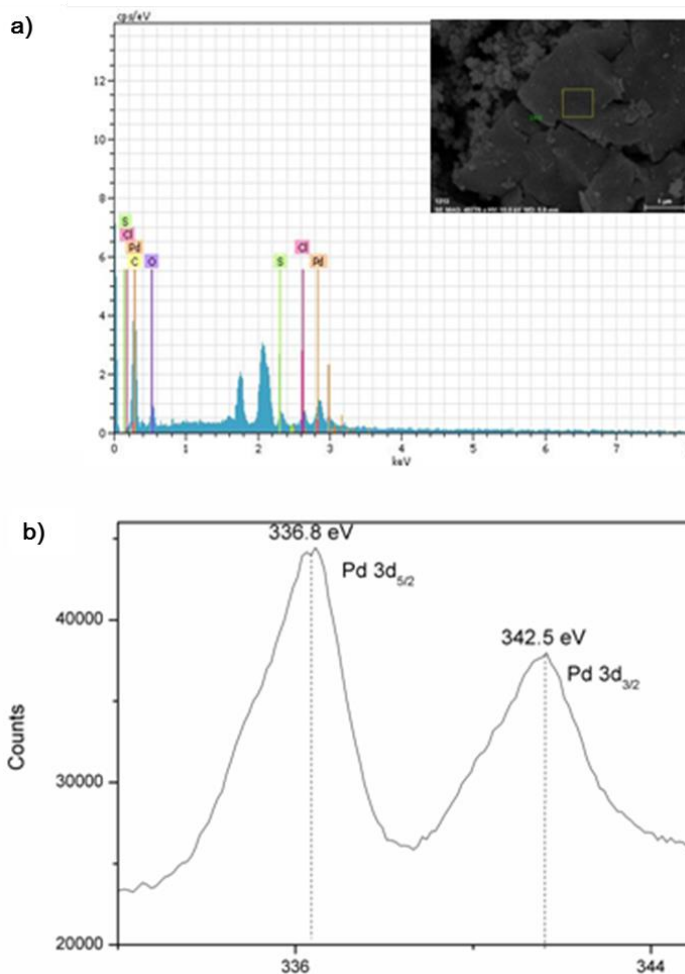
**Figure 44. EDX and XPS data of Tyr peptide@PPy@Pd catalyst.** a) EDX data of Tyr Peptide@PPy@Pd catalyst. b) XPS data of Tyr Peptide@PPy@Pd catalyst. The peak of 336.8 eV corresponds to (Pd $3d_{5/2}$, Pd $3d_{3/2}$), and the one at 342.5 eV corresponds to Pd(II) .

### 3.3.3. Catalytic Properties of Tyrsine Peptide–Polypyrrole Supported Palladium(II) Catalyst
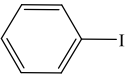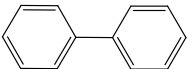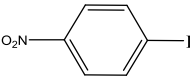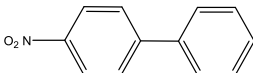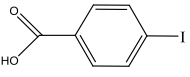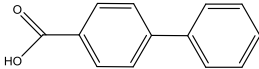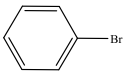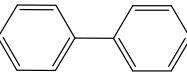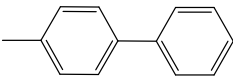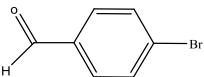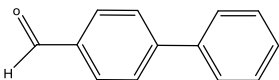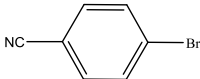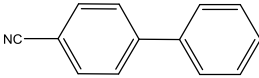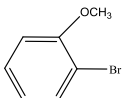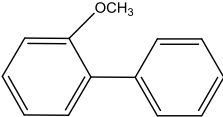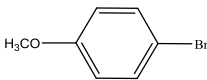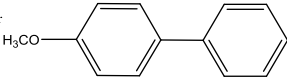
Suzuki coupling reaction of aryl halides with arylboronic acid with Tyr Peptide@PPy@Pd catalyst (1.5 mol%) was performed in water or 10% DMSO/water at 50$^\circ$C (Fig. 45). In coupling reaction of aryl iodides and activated aryl bromides with aryl boronic acid, biphenyl products were obtained in 4 hours with high isolate yields of over 90%. However, palladium nanoparticles catalysts supported on polypyrrole without YYACAYY peptide gave poor catalytic activity compare to Tyr Peptide@PPy@Pd catalyst. The C-C couplings of aryl chlorides are highly desirable due to their easy availability. However, they are much difficult to be coupled than aryl iodides and bromides. In our case, even deactivated aryl chlorides proceeded C-C cross-coupling reaction by Tyr Peptide@PPy@Pd catalyst in high yield (90%) at 80 ℃ in water. (entry 13~19, Table 4)
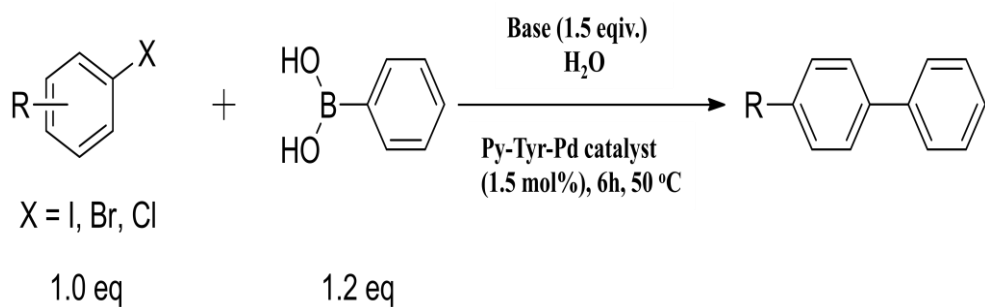
**Figure 45. Suzuki coupling reaction in the presence of Tyr peptide-polypyrrole supported palladium Catalyst (Tyr peptide@PPy@Pd Catalyst).**

**Table 4. Suzuki Coupling Reaction in the Presence of Tyr peptide@PPy@Pd Catalyst. Conditions:** Aryl halides (1 mmol), phenylboronic acid (1.2 mmol), Tyr peptide@PPy@Pd (1.5 mol%), Triethylamine (1.5 mmol), in $H_2O$ at 50 ℃

| Entry | Time(h) | Substrate | Product | Isolated Yield (%) |
|-------|---------|-----------|---------|--------------------|
| 1 | 2 |  |  | 94 |
| 2 | 2 |  |  | 97 |
| 3 | 2 |  |  | 97 |
| 4 | 2 |  |  | 93 |
| 5 | 4 |  |  | 98 |
| 6 | 4 |  |  | 96 |
| 7 | 8 |  |  | 91 |
| 8 | 8 |  |  | 67 |
| 9 | 8 |  |  | 98 |

**Table 4. Suzuki Coupling Reaction in the Presence of Tyr peptide@PPy@Pd Catalyst. Conditions. (Continued)**

| | | | | |
|---|---|---|---|---|
| 10 | 12 | | | 87 |
| 11 | 8 | | | 95 |
| 12 | 4 | | | 99 |
| 13 | 4 | | | 98 |
| 14 | 4 | | | 99 |
| 15 | 4 | | | 99 |
| 16 | 8 | | | 94 |
| 17 | 8 | | | 91 |
| 18 | 12 | | | 93 |
| 19 | 12 | | | 96 |

Aryl halides (1 mmol), phenylboronic acid (1.2 mmol), Tyr peptide@PPy@Pd (1.5 mol%), Triethylamine (1.5 mmol), in $H_2O$ at 50 ℃

### 3.3.5. Reuseability of Tyrsine Peptide–Polypyrrole Supported Palladium(II) Catalyst

One of the advantages of heterogeneous catalyst is that the catalyst can be easily isolated and reused. To evaluate the reusability of Tyr Peptide@PPy@Pd Catalyst, the recovered catalysts were reused in Suzuki coupling reaction of 4-bromobenzene with phenylboronic acid in water. The catalytic activities of Tyr Peptide@PPy@Pd catalyst remained constant after second cycle until fifth cycle, maintaining good catalytic activity. After each cycle of the reaction, Tyr Peptide@PPy@Pd catalyst was analyzed by ICP-AES to measure the amount of Pd loading on the catalyst. The ICP-AES results showed that Pd leaching was not serious during the coupling reactions, maintaining Pd loading of 0.28–0.34 mmol/g after each cycle. Based on these results, we can conclude Tyr Peptide@PPy@Pd catalyst is a potent catalyst in successive Suzuki coupling reactions in water without significant Pd leaching up to fifth cycle. (Table 5)

**Table 5. Reuseability Test of Tyrsine Peptide–Polypyrrole Supported Palladium(II) Catalyst**

| Catalyst | Yield (%)[b] | | | | |
|---|---|---|---|---|---|
| | 1st cycle | 2nd cycle | 3rd cycle | 4th cycle | 5th cycle |
| **PPy-Tyr-Pd Catalyst** | 99 | 87 | 85 | 75 | 81 |

# 4. Conclusion

We have prepared the tyrosine containing peptide film that can provide a platform for the construction of functionally controllable 2D nanostructures, and identified specific peptide sequences, YYCYY and YYACAYY, that can afford densely packed 2D film structure at air/water interface. The resulting 2D peptide film can withstand the surface tension of water and modify the intrinsic curvature of water droplet. The atomic force microscopy (AFM) analysis along the film edges shows an evidence of film stacking of multiple nano sheets, whose minimum thickness is 1.4 nm. From the mechanism study by computational simulation, sequence-dependent tyrosine based peptide self-assembly presented highlights the role of peptide folding in molecular packing and the importance of specific amino acids in organization behaviors. We confirm the dimerization of YYACAYY by disulfide bond played a key role in 2D peptide assembly. Our findings provide new insight into self-assembled peptide interfaces through dynamic curvature control and site-selective functionalization. The tyrosine based peptide film served as a redox active scaffold for developing an enzyme mimetic catalyst. From the results of oxidative pyrrole polymerization on tyrosine peptide film, we conclude that the tyrosine radicals (Tyr●) were easily generated from peptide film and able to trigger or enhance the chemical reaction in a manner similar to that observed in various biological systems. We also found that tyrosine peptide film induced the homogeneous palladium nanoparticles formation. Finally, this tyrosine peptide–polypyrrole supported

palladium nanoparticles (Tyr Peptide@PPy@Pd Catalyst) gave good catalytic activity for Suzuki cross-coupling reaction in water, and was reusable more than five times. The catalyst even activated aryl chlorides in Suzuki coupling reaction which could not be performed with most heterogeneous palladium catalysts .

# 5. References

1.  Mann, S., Shenton, W., Li, M., Connolly, S. & Fitzmaurice, D. Biologically programmed nanoparticle assembly. *Adv, Mater.* **12**, 147-150 (2000).

2.  Niemeyer, C. M. Nanoparticles, proteins, and nucleic acids: biotechnology meets materials science. *Angew. Chem. Int. Ed.* **40**, 4128-4158 (2001).

3.  Rong, J., Niu, Z., Lee, L. A. & Wang, Q. Self-assembly of viral particles. *Current Opinion in Colloid & Interface Science* **16**, 441-450 (2011).

4.  Meldrum, F. C., Wade, V. J., Nimmo, D. L., Heywood, B. R. & Mann, S. Synthesis of inorganic nanophase materials in supramolecular protein cages. *Nature* **349**, 684-687 (1991).

5.  Shenton, W., Mann, S., Cölfen, H., Bacher, A. & Fischer, M. Synthesis of nanophase iron oxide in lumazine synthase capsids. *Angew. Chem. Int. Ed.* **40**, 442-445 (2001).

6.  Kuang, X. *et al.* Assembly of a metal–organic framework by sextuple intercatenation of discrete adamantane-like cages. *Nat. Chem.* **2**, 461-465 (2010).

7.  Palmore, G. T. R., Bertschy, H., Bergens, S. H. & Whiteside, G. M. A methanol/dioxygen biofuel cell that uses NAD(+)-dependent dehydrogenases as catalysts: Application of an electro-enzymatic method to regenerate nicotinamide adenine dinucleotide at low overpotentials. *J. Electroanal. Chem.* **443**, 155-161 (1998).

8.      Mukherjee, D., May, M., Vaughn, M., Bruce, B. D. & Khomami, B. Controlling the Morphology of Photosystem I Assembly on Thiol-Activated Au Substrates. *Langmuir* **26**, 16048-16054 (2010).

9.      Selkoe, D. J. Folding proteins in fatal ways. *Nature* **426**, 900-904 (2003).

10.     Chiti, F. & Dobson, C. M. Protein misfolding, functional amyloid, and human disease. *Annu. Rev. Biochem.* **75**, 333-366 (2006).

11.     Pepys, M. B. Amyloidosis. *Annu. Rev. Med.* **57**, 223-241 (2006).

12.     Sawaya, M. R. *et al.* Atomic structures of amyloid cross-β spines reveal varied steric zippers. . *Nature* **447**, 453-457 (2007).

13.     Sachse, C., Fändrich, M. & Grigorieff, N. Paired β-sheet structure of an Aβ(1-40) amyloid fibril revealed by electron microscopy. *Proc. Natl. Acad. Sci. U.S.A.* **105**, 7462-7466 (2008).

14.     Chimon, S. *et al.* Evidence of fibril-like β-sheet structures in a neurotoxic amyloid intermediate of Alzheimer's β-amyloid. *Nat. Struct. Mol. Biol.* **105**, 7462-7466 (2008).

15.     LeVine, H. Quantification of beta-sheet amyloid fibril structures with thioflavin T. *Meth. Enzymol.* **309**, 274-284 (1999).

16.     Sunde, M. *et al.* Common core structure of amyloid fibrils by synchrotron X-ray diffraction. . *J. Mol. Biol.* **273**, 729-739 (1997).

17.     Klunk, W. E., Jacob, R. F. & Manson, R. P. Quantifying amyloid by congo red spectral assay. *Methods Enzyol.* **309**, 285-305 (1999).

18.     Anfinsen, C. B. Principles that govern the folding of protein chains. *Science*

**181**, 223-230 (1973).

19. Hruby, V. J., Li, G., HaskellLuevano, C. & Shenderovich, M. Design of peptides, proteins, and peptidomimetics in chi space. *Biopolymers* **43**, 219-266 (1997).

20. Ghadiri, M. R., Granja, J. R. & Buehler, L. K. Artificial transmembrane ion channels from self-assembling peptide nanotubes. *Nature* **369**, 301-304 (1994).

21. Reches, M. & Gazit, E. Casting metal nanowires withing discrete self-assembled peptide nanotubes. *Science* **300**, 625-627 (2003).

22. Hartgerink, J. D., Beniash, E. & Stupp, S. I. Self-assembly and mineralization of peptide-amphiphile nanofibers. *Science* **294**, 1684-1688 (2001).

23. Aggeli, A. *et al.* Hierarchical self-assembly of chiral rod-like molecules as a model for peptide beta-sheet tape, ribbons, fibrils, and fibers. *Proc. Natl. Acad. Sci. USA* **98**, 11857-11862 (2001).

24. Zhang, S., Holmes, T., Lockshin, C. & Rich, A. Spontaneous assembly of a self-complementary oligopeptide to form a stable macroscopic membrane. *Proc. Natl. Acad. Sci. USA* **90**, 3334-3338 (1993).

25. Nam, K. T. *et al.* Free-floating ultrathin two-dimensional crystals from sequence-specific peptoid polymers. *Nat. Mater.* **9**, 454-460 (2010).

26. Rapaport, H. *et al.* Assembly of triple-stranded b-sheet peptides at interfaces. *J. Am. Chem. Soc.* **124**, 9342-9343 (2002).

27. Han, T. H. *et al.* Highly entangled hollow TiO2 nanoribbons templating diphenylalanine assembly. *J. Mater. Chem.* **19**, 3512-3516 (2009).

28. Kisiday, J. *et al.* Self-assembling peptide hydrogel fosters chondrocyte extracellular matrix production and cell division: Implications for cartilage tissue repair. *Proc. Natl. Acad. Sci. USA* **99**, 9996-10001 (2002).

29. Chung, W.-J. *et al.* Biomimetic self-templating supramolecular structures. *Nature* **478**, 364-368 (2011).

30. Caplan, M. R., Schwartzfarb, E. M., Zhang, S., Kamm, R. D. & Lauffenburger, D. A. Control of self-assembling oligopeptide matrix formation through systematic variation of amino acid sequence. *Biomaterials* **23**, 219-227 (2002).

31. Zhang, S. Fabrication of novel biomaterials through molecular self-assembly. *Nat. Biotechnol.* **21**, 1171-1178 (2003).

32. Yokoi, H., Kinoshita, T. & Zhang, S. Dynamic reassembly of peptide RADA16 nanofiber scaffold. *Proc. Natl Acad. Sci. U.S.A.* **102**, 8414-8419 (2005).

33. Marini, D. M., Hwang, W., Lauffenberger, D. A., Zhang, S. & Kamm, R. D. Interparticle coupling effects on plasmon resonances of nanogold particles. *Nano Lett.* **2**, 295-299 (2002).

34. Matsumura, S., Uemura, S. & Mihara, H. Fabrication of nanofibers with uniform morphology by self-assembly of designed peptides. *Chem. Eur. J.* **10**, 2789-2794 (2004).

35. Wagner, D. E. *et al.* Toward the development of peptide nanofilaments and nanoropes as smart materials. *Proc. Natl Acad. Sci. U.S.A.* **104**, 10853-10858 (2005).

36. Fishwick, C. W. F. *et al.* Structures of helical β-tapes and twisted ribbons: the role of side-chain interactions on twist and bend behavior. *Nano Lett.* **3**, 1475-1479 (2003).

37. Maltzahn, G. v., Vauthey, S., Santoso, S. & Zhang, S. Positively charged surfactant-like peptides self-assemble into nanostructures. *Langmuir* **19**, 4332-4337 (2003).

38. Ryu, J. & Park, C. B. High-Temperature Self-Assembly of Peptides into Vertically Well-Aligned Nanowires by Aniline Vapor. *Adv, Mater.* **20**, 3754-3758 (2008).

39. Ryu, J. & Park, C. B. Synthesis of Diphenylalanine/Polyaniline Core/Shell Conducting Nanowires by Peptide Self-Assembly. *Angew. Chem. Int. Ed.* **48**, 4820-4823 (2009).

40. Reches, M. & Gazit, E. Casting metal nanowires within discrete self-assembled peptide nanotubes. *Science* **300**, 625-627 (2003).

41. Niu, L., Chen, X., Allen, S. & Tendler, S. J. B. Using the bending beam model to estimate the elasticity of diphenylalanine nanotubes. *Langmuir* **23**, 7443-7446 (2007).

42. Yemini, M., Reches, M., Rishpon, J. & Gazit, E. Novel electrochemical biosensing platform using self-assembled peptide nanotubes. *Nano Lett.* **5**,

183-186 (2005).

43.     Ryu, J., Lim, S. Y. & Park, C. B. Photoluminescent peptide nanotubes. *Adv,
        Mater.* **21**, 1577 (2009).

44.     Kim, S. W. *et al.* Fabrication and electrochemical characterization of TiO2
        three-dimensional nanonetwork based on peptide assembly. *ACS Nano* **3**,
        1085-1090 (2009).

45.     Yan, X. *et al.* Self-assembly of peptide-based colloids containing lipophilic
        nanocrystals. *Small* **4**, 1687-1693 (2008).

46.     Yan, X., Cui, Y., He, Q., Wang, K. & Li, J. Organogels based on self-
        assembly of diphenylalanine peptide and their application to immobilize
        quantum dots. *Chem. Mater.* **20**, 1522-1526 (2008).

47.     Zhu, P., Yan, X., Su, Y., Yang, Y. & Li, J. Solvent-induced structural
        transition of self-assembled dipeptide: from organogels to microcrystals.
        *Chem. Eur. J.* **16**, 3176-3183 (2010).

48.     Toledano, S., Williams, R. J., Jayawarna, V. & Ulijn, R. V. Enzyme-
        triggered self-assembly of peptide hydrogels via reversed hydrolysis. *J. Am.
        Chem. Soc.* **128**, 1070-1071 (2006).

49.     Smith, A. M. *et al.* Fmoc-Diphenylalanine Self Assembles to a Hydrogel via
        a Novel Architecture Based on π–π Interlocked β-Sheets. *Adv, Mater.* **20**,
        37-41 (2008).

50.     Görbitz, C. H. The structure of nanotubes formed by diphenylalanine, the
        core recognition motif of Alzheimer's β-amyloid polypeptide. *Chem.*

*Commun*, 2332-2334 (2006).

51.     Park, J. S., Han, T. H., Oh, J. K. & Kim, S. O. Size-Dependent Isotropic/Nematic Phase Transition Behavior of Liquid Crystalline Peptide Nanowires. *Macromol. Chem. Phys.* **210**, 1283-1290 (2009).

52.     Adler-Abramovich, L. *et al.* Self-assembled arrays of peptide nanotubes by vapour deposition. *Nat. Nanotechnol.* **4**, 849-854 (2009).

53.     Carny, O., Shalev, D. E. & Gazit, E. Fabrication of coaxial metal nanocables using a self-assembled peptide nanotube scaffold. *Nano Lett.* **6**, 1594 (2006).

54.     Kim, J. *et al.* Role of water in directing diphenylalanine assembly into nanotubes and nanowires. *Adv, Mater.* **22**, 583-587 (2010).

55.     Hamill, S. J., Cota, E., Chothia, C. & Clarke, J. Conservation of folding and stability within a protein family: The tyrosine corner as an evolutionary cul-de-sac. *J. Mol. Biol.* **295**, 641-649 (2000).

56.     McConnell, I., Li, G. & Brudvig, G. W. Energy conversion in natural and artificial photosynthesis. *Chem. Biol.* **17**, 434-447 (2010).

57.     Hammarstrom, L. & Styring, S. Proton-coupled electron transfer of tyrosines in photosystem II and model systems for artificial photosynthesis: The role of a redox-active link between catalyst and photosensitizer. *Energy Environ. Sci.* **4**, 2379-2388 (2011).

58.     Elvin, C. M. *et al.* Synthesis and properties of crosslinked recombinant pro-resilin. *Nature* **437**, 999-1002 (2005).

111

59.    Tilley, K. A. *et al.* Tyrosine cross-links: Molecular basis of gluten structure and function. *J. Agric. Food Chem.* **49**, 2627-2632 (2001).

60.    Moore, R., Clark, W. D., Kingsley, R. S. & Vodopich, D. *Botany. Wm. C. Brown:New York* (1995).

61.    Xie, L. & Donk, W. A. v. d. Homemade cofactors: Self-processing in galactose oxidase. *Proc. Natl Acad. Sci. U.S.A.* **98**, 12863-12865 (2001).

62.    Cotruvo, J. A. & Stubbe, J. Class I ribonucleotide reductases: Metallocofactor assembly and repair in vitro and in vivo. *Annu. Rev. Biochem.* **80**, 733-767 (2011).

63.    Stubbe, J., Nocera, D. G., Yee, C. S. & Chang, M. C. Y. Radical initiation in the class I ribonucleotide reductase: Long-range proton-coupled electron transfer? *Chem. Rev.* **103**, 2167-2201 (2003).

64.    Firbank, S. J. *et al.* Crystal structure of the precursor of galactose oxidase: An unusual self-processing enzyme. *Proc. Natl Acad. Sci. USA* **98**, 12932-12937 (2001).

65.    Rogers, M. S. *et al.* The stacking tryptophan of galactose oxidase: A second-coordination sphere residue that has profound effects on tyrosyl radical behavior and enzyme catalysis. *Biochemistry* **46**, 4606-4618 (2007).

66.    Whittaker, J. W. Free radical catalysis by galactose oxidase. *Chem. Rev.* **103**, 2347-2363 (2003).

67.    Rogers, M. S. & Dooley, D. M. Copper-tyrosyl radical enzymes. *Curr. Opin. Chem. Biol.* **7**, 189-196 (2003).

68. Firbank, S. J. *et al.* Crystal structure of the precursor of galactose oxidase: An unusual self-processing enzyme. *Proc. Natl Acad. Sci. U.S.A.* **98**, 12932-12937 (2001).

69. Ito, N., Phillips, S. E. V., Yadav, K. D. S. & Knowles, P. F. Crystal-structure of a free radical enzyme: Galactose oxidase. *J. Mol. Biol.* **238**, 794-814 (1994).

70. Rogers, M. S. *et al.* The stacking tryptophan of galactose oxidase: A second-coordination sphere residue that has profound effects on tyrosyl radical behavior and enyme catalyst. *Biochemistry* **46**, 4606-4618 (2007).

71. Janes, S. M. *et al.* A new redox cofactor in eukaryotic enzymes: 6-hydroxydopa at the active site of bovine serum amine oxidase. *Science* **248**, 981-987 (1990).

72. Ostermeier, C., Harrenga, A., Ermler, U. & Michel, H. Structure at 2.7 Å resolution of the Paracoccus denitrificans two-subunit cytochrome c oxidase complexed with an antibody FV fragment. *Proc. Natl Acad. Sci. U.S.A.* **94**, 10547-10553 (1997).

73. Yoshikawa, S. *et al.* Redox-coupled crystal structural changes in bovine heart cytochrome c oxidase. *Science* **280**, 1723-1729 (1998).

74. Bravo, J. *et al.* Identification of a novel bond between a histidine and the essential tyrosine in catalase HPII of Escherichia coli. *Protein Sci.* **6**, 1016-1023 (1997).

75. Wang, S. X. *et al.* A crosslinked cofactor in lysyl oxidase: redox function

for amino acid side chains. *Science* **273**, 1078-1084 (1996).

76.    Kang, S. *et al.* Removal of Intact β2-Microglobulin at Neutral pH by Using Seed-Conjugated Polymer Beads Prepared with β2-Microglobulin-derived Peptide (58-67). *Biotechnol. Prog.* **27**, 521-529 (2011).

77.    Phan-Huu, C., Keller, N., Charbonniere, L. J., Ziessei, R. & Ledoux, M. J. Carbon nanofiber supported palladium catalyst for liquid-phase reactions. An active and selective catalyst for hydrogenation of C=C bonds. *Chem. Commun*, 1871-1872 (2000).

78.    Luksirikul, P., Tedsree, K., Moloney., M. G., Green, M. L. H. & Tsang, S. C. E. Electron Promotion by Surface Functional Groups of Single Wall Carbon Nanotubes to Overlying Metal Particles in a Fuel-Cell Catalyst. *Angew. Chem. Int. Ed.* **124**, 7104-7107 (2012).

79.    Pan, X. & Bao, X. The effects of confinement inside carbon nanotubes on catalysis. *Acc. Chem. Res.* **44**, 553-562 (2011).

80.    Shao, L. *et al.* The Role of Palladium Dynamics in the Surface Catalysis of Coupling Reactions. *Angew. Chem. Int. Ed.* **52**, 2114-2117 (2013).

81.    Schwarz, J. *et al.* Polymer-Supported Carbene Complexes of Palladium: Well-Defined, Air-Stable, Recyclable Catalysts for the Heck Reaction. *Chem. Eur. J.* **6**, 1773-1780 (2000).

82.    Steel, P. G. & Teasdale, C. W. T. Polymer supported palladium N-heterocyclic carbene complexes: long lived recyclable catalysts for cross coupling reactions. *Tetrahedron Lett.* **45**, 8977-8980 (2004).

83. Lu, J. & Toy, P. H. Organic polymer supports for synthesis and for reagent and catalyst immobilization. *Chem. Rev.* **109**, 815-838 (2009).

84. Clark, J. H., Macquarrie, D. J. & Mubofu, E. B. Preparation of a novel silica-supported palladium catalyst and its use in the Heck reaction. *Green Chem.* **2**, 53-56 (2000).

85. Crudden, C. M., Sateech, M. & Lewis, R. Mercaptopropyl-modified mesoporous silica: A remarkable support for the preparation of a reusable, heterogeneous palladium catalyst for coupling reactions. *J. Am. Chem. Soc.* **127**, 10045-10050 (2005).

86. Fihri, A., Cha, D., Bouhrara, M., Almana, N. & Polshettiwar, V. Fibrous Nano-Silica (KCC-1)-Supported Palladium Catalyst: Suzuki Coupling Reactions Under Sustainable Conditions. *Chem. Sus. Chem.* **5**, 85-89 (2012).

87. Yamaguchi, K., Matsushita, M. & Mizuno, N. Efficient hydration of nitriles to amides in water, catalyzed by ruthenium hydroxide supported on alumina. *Angew. Chem. Int. Ed.* **116**, 1602-1606 (2004).

88. Kwon, M. S. *et al.* Palladium nanoparticles entrapped in aluminum hydroxide: dual catalyst for alkene hydrogenation and aerobic alcohol oxidation. *Org. Lett.* **7**, 1077-1079 (2005).

89. Oishi, T., Katayama, T., Yamaguchi, K. & Mizuno, N. Heterogeneously Catalyzed Efficient Alkyne–Alkyne Homocoupling by Supported Copper Hydroxide on Titanium Oxide. *Chem. Eur. J.* **15**, 7539-7542 (2009).

90. He, J., Kim, J. W., Yamaguchi, K. & Mizuno, N. Efficient Catalytic

Synthesis of Tertiary and Secondary Amines from Alcohols and Urea. *Angew. Chem. Int. Ed.* **121**, 10072-10075 (2009).

91. Li, Y., Das, S., Zhou, S., Junge, K. & Beller, M. General and selective copper-catalyzed reduction of tertiary and secondary phosphine oxides: convenient synthesis ofphosphines. *J. Am. Chem. Soc.* **134**, 9727-9732 (2012).

92. Gorbanev, Y. Y., Kegnaes, S., Hanning, C. W., Hansen, T. W. & Riisager, A. Acetic Acid Formation by Selective Aerobic Oxidation of Aqueous Ethanol over Heterogeneous Ruthenium Catalysts. *ACS Catal.* **2**, 604-612 (2012).

93. Littke, A. F. & Fu, G. C. Palladium-catalyzed coupling reactions of aryl chlorides. *Angew. Chem. Int. Ed.* **41**, 4176-4211 (2002).

94. Yuan, B., Pan, Y., Li, Y., Yin, B. & Jiang, H. A highly active heterogeneous palladium catalyst for the suzuki–miyaura and ullmann coupling reactions of aryl chlorides in aqueous media. *Angew. Chem. Int. Ed.* **49**, 4054-4058 (2010).

95. Botella, L. & Najera, C. A convenient oxime-carbapalladacycle-catalyzed suzuki cross-coupling of aryl chlorides in water *Angew. Chem. Int. Ed.* **41**, 179-181 (2002).

96. Jin, M. J. & Lee, D. H. A practical heterogeneous catalyst for the suzuki, sonogashira, and stille coupling reactions of unreactive aryl chlorides. *Angew. Chem. Int. Ed.* **122**, 1137-1140 (2010).

97. Gallon, B. J., Kojima, R. W., Kaner, R. B. & Diaconescu, P. L. Palladium

nanoparticles supported on polyaniline nanofibers as a semi-heterogeneous catalyst in water. *Angew. Chem. Int. Ed.* **46**, 7251-7254 (2007).

98. Lee, D. H., Kwon, Y. J. & Jin, M. J. Highly active palladium catalyst for the sonogashira coupling reaction of unreactive aryl chlorides. *Adv. Synth. Catal.* **353**, 3090-9094 (2011).

99. Dujardin, E., Peet, C., Stubbs, G., Culver, J. N. & Mann, S. Organization of metallic nanoparticles using tobacco mosaic virus templates. *Nano Lett.* **3**, 413-417 (2003).

100. Lichtenstein, B. R. *et al.* Engineering oxidoreductase: Marquette proteins designed from scratch. *Biochem. Soc. Trans.* **40**, 561-566 (2012).

101. Chakraborty, S. *et al.* Design of a three-helix bundle capable of binding heavy metal in a triscysteine environment. *Angew. Chem. Int. Ed.* **50**, 2049-2053 (2011).

102. Korendovych, I. V., Senes, A., Kim, Y. H., Lear, J. D. & Fry, H. C. De novo design and molecular assembly of a transmembrane diporphyrin-binding protein complex. *J. Am. Chem. Soc.* **132**, 15516-15518 (2010).

103. Maglio, O. *et al.* Artificial di-iron proteins: solution characterization of four helix bundles contatining two distinct types of inter-helical loops. *J. Biol. Inorg. Chem* **10**, 539-549 (2005).

104. Salgado, E. N., Radford, R. J. & Tezcan, F. A. Metal-directed protein self-assembly. *Acc. Chem. Res.* **43**, 661-672 (2010).

105. Jones, A. K., Lichtenstein, B. R., Dutta, A., Gordon, G. & Dutton, P. L.

Synthetic hydrogenases: Incorporation of an iron carbonyl thiolate into a designed peptide. *J. Am. Chem. Soc.* **129**, 14844-14845 (2007).

106.    Ball, Z. Designing enzyme-like catalysts: Rhodium(II) metallopeptide case study. *Acc. Chem. Res.* **46**, 560-570 (2012).

107.    Pacardo, D. B. & Knecht, M. R. Exploring the mechanism of stille C-C coupling via peptide-capped Pd nanoparticles results in low temperature reagent selectivity. *Catal. Sci. Technol.* **3**, 745-753 (2013).

108.    Sethi, M., Pacardo, D. R. & Knecht, M. R. Biological surface effects of metallic nanomaterials for applications in assembly and catalysis. *Langmuir* **26**, 15121-15134 (2010).

109.    Pacardo, D. B., Sethi, M., Jones, S. E., Naik, R. R. & Knecht, M. R. Biomimetic synthesis of Pd nanocatalysts for the stille coupling reaction. *ACS Nano* **3**, 1288-1296 (2009).

110.    Ryoo, H. I., Lee, J. S., Park, C. B. & Kim, D. P. A microfluidic system incorporated with peptide/Pd nanowires for heterogeneous catalytic reactions. *Lab. Chip* **11**, 378-380 (2011).

111.    Vaddula, B. R., Saha, A., J, L. & Varma, R. S. A simple and facile Heck-type arylation of alkenes with diaryliodonium salts using magnetically recoverable Pd-catalyst. *Green Chem.* **14**, 2133-2136 (2012).

112.    Han, T. *et al.* Bionanosphere Lithography via Hierarchical Peptide Self-Assembly of Aromatic Triphenylalanine. *Small* **6**, 945-951 (2010).

113.    MacKintosh, F. C. & Lubensky, T. C. Orientational order, topology, and

vesicle shapes. *Phys. Rev. Lett.* **67**, 1169-1172 (1991).

114. Bowick, M. J. & Giomi, L. Two-dimensional matter: Order, curvature and defects. *Adv. Phys.* **58**, 449-563 (2009).

115. Bausch, A. R. *et al.* Grain boundary scars and spherical cystallography. *Science* **299**, 1716-1718 (2003).

116. Bowick, M. J., Giomi, L., Shin, H. & Thomas, C. K. Bubble-raft model for a paraboloidal crystal. *Phys. Rev. E* **77**, 1-5 (2008).

117. Irvine, W. T. M., Vitelli, V. & Chaikin, P. M. Pleats in crystals on curved surfaces. *Nature* **468**, 947-951 (2010).

118. Subramaniam, A. B., Abkarian, M. & Stone, H. A. Controlled assembly of jammed colloidal shells on fluid droplets. *Nat. Mater.* **4**, 553-556 (2005).

119. King, H., Schroll, R. D., Davidovitch, B. & Menon, N. Elastic sheet on a liquid drop reveals wrinkling and crumpling as distinct symmetry-breaking instabilities. *Proc. Natl. Acad. Sci. USA* **109**, 9716-9720 (2012).

120. Reddy, V. S., Natchiar, S. K., Stewart, P. L. & Nemerow, G. R. Crystal structure of human adenovirus at 3.5 angstrom resolution. *Science* **329**, 1071-1075 (2010).

121. Szilvay, G. R. *et al.* Self-assembled hydrophobin protein films at the air−water interface: Structural analysis and molecular engineering. *Biochemistry* **46**, 2345-2354 (2007).

122. Xing, X. *et al.* Morphology of nematic and smectic vesicles. *Proc. Natl. Acad. Sci. USA* **109**, 5202-5206 (2012).

123.    Mejia, A. F. *et al.* Surface-controlled shape design of discotic micro-particles. *Soft Matter* **6**, 4885-4894 (2010).

124.    Oswald, P. & Lejcek, L. Faceting and stability of smectic A droplets on a solid substrate. *Eur. Phys. J. E* **19**, 441-452 (2006).

125.    Beychok, S. & Fasman, G. D. Circular dichroism of poly-L-tyrosine. *Biochemistry* **3**, 1675-1678 (1964).

126.    Reid, R. E. *Peptide and protein drug analysis*. (Dekker, 2000).

127.    Siddiqui, S. A., Pandey, A. K., Dwivedi, A., Jain, S. & Misra, N. Comparative conformational, structural and vibrational study on the molecular structure of tyrosine and L-DOPA using density functional theory. *J. Chem. Pharm. Res.* **2**, 835-850 (2010).

128.    Szymanski, H. A. & Erickson, R. E. Infrad band handbook. *IPlenum Press, New York* (1970).

129.    Aulisa, L., Dong, H. & Hartgerink, J. D. Self-assembly of multidomain peptide: Sequence variation allows control over cross-linking and viscoelasticity. *Biomacromolecules* **10**, 2694-2698 (2009).

130.    Gremlich, H. U. Infrared and Raman spectroscopy of biological materials. *Marcel Dekker* **24** (2001).

131.    Sarker, N. H. *et al.* Biomimetic growth of gallic acid-ZnO hybrid assemblies and their applications. *J. Nanopart. Res.* **14**, 1-12 (2012).

132.    DeLange, F. *et al.* Tyrosine structural changes detected during the photoactivation of rhodopsin. *J. Biol. Chem.* **273**, 23735-23739 (1998).

133. Schnitzer, M. I., Monreal, C. M., Jandi, G., Leinweber, P. & Fransharm, P. B. The conversion of chicken manure to biooil by fast pyrolysis II. Analysis of chicken manure, biooils, and char by curie-point pyrolysis-gas chromatography/mass spectrometry (Cp Py-GC/MS). *J. Environ. Sci. Health B* **42**, 79-95 (2007).

134. Maiti, N. C., Apetri, M. M., Zagorski, M. G., Carey, P. R. & Anderson, V. E. Raman spectroscopic characterization of secondary structure in natively unfolded proteins: alpha-synuclein. *J. Am. Chem. Soc.* **126**, 2399-2408 (2004).

135. Chelli, R., Gervasio, F. L., Procacci, P. & Schettino, V. Stacking and T-shape competition in aromatic-aromatic amino acid interactions. *J. Am. Chem. Soc.* **124**, 6133-6143 (2002).

136. Li, X. & Liu, D. R. DNA-templated organic synthesis: Nature's strategy for controlling chemical reactivity applied to synthetic molecules. *Angew. Chem. Int. Ed.* **43**, 4848-4870 (2004).

137. Asavapiriyanont, S., Chandler, G. K., Gunawardena, G. A. & Pletcher, D. The electrodeposition of polypyrrole films from aqueous-solutions. *J. Electroanal. Chem.* **177**, 229-244 (1984).

138. Wanger, C. D., Riggs, W. M., Davis, L. E., Moulder, J. F. & E.Muilenberg, G. Handbook of X-ray Photoelectron Spectroscopy *Perkin-Elmer Corp* **3**, v-v (1981).

139. Rademann, J., Barth, M., Brock, R., Egelhaaf, H. J. & Jung, G. Spatially

Resolved Single Bead Analysis: Homogeneity, Diffusion, and Adsorption in Cross-Linked Polystyrene. *Chemistry-a European Journal* **7**, 3884-3889 (2001).
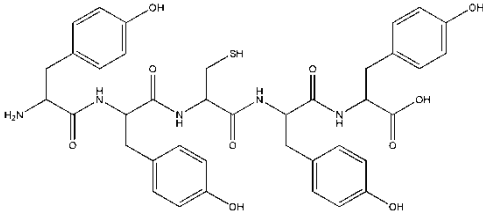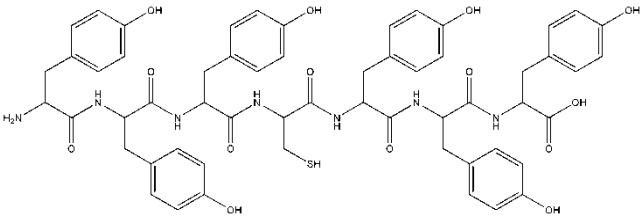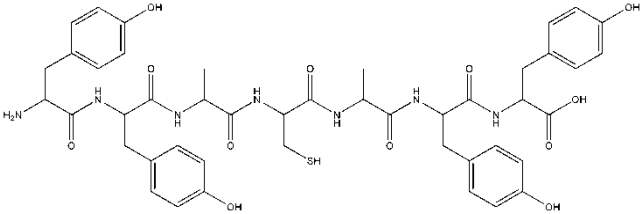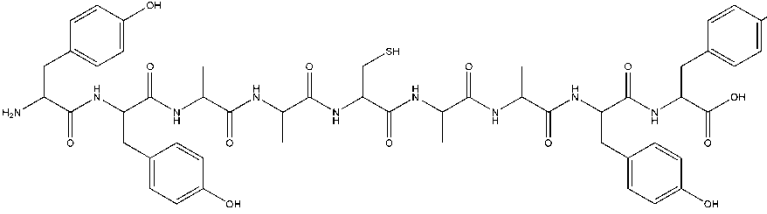
# 6. Appendix

**Appendix 1. Binding Energy Profiles of Various Metal Complexes in XPS**

| | 3d$_{5/2}$ Binding Energy (eV) | | | | | |
|---|---|---|---|---|---|---|
| | 335 | 336 | 337 | 338 | 339 | 340 |
| Pd | ▮ | | | | | |
| Pd$_2$Si | | | ▮ | | | |
| Pd$_3$Si | | ▮ | | | | |
| Halides | | | ▬▬▬ | | | |
| PdO | | ▮ | | | | |
| PdO$_2$ | | | | ▮ | | |
| K$_2$PdCl$_4$ | | | | ▮ | | |
| K$_2$PdBr$_4$ | | | ▮ | | | |
| Pd(OAc)$_2$ | | | | | ▮ | |
| Pd(SPh)$_2$ | | | | ▮ | | |

# Appendix   2. The Structures of the Synthesized Peptides

| Sequence | Structure |
|---|---|
| [1]YYCYY |  |
| [2]YYYCYYY |  |
| [3]YYACAYY |  |
| [4]YYAACAAYY |  |

# Appendix  2. The Structures of the Synthesized Peptides (Continued)

<sup>5</sup>YYGCGYY
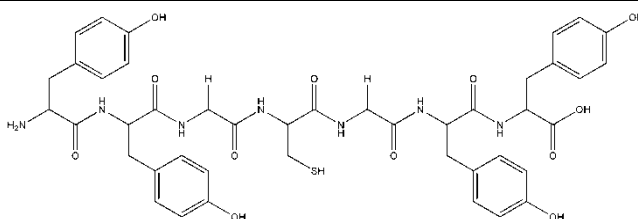


<sup>6</sup>YFCFY
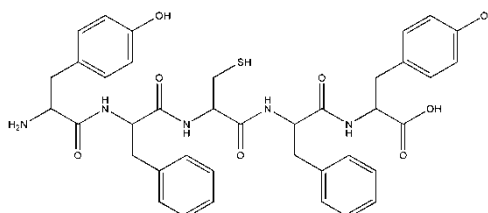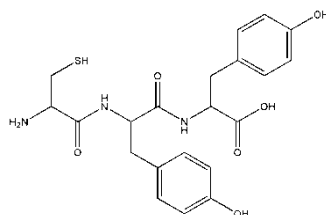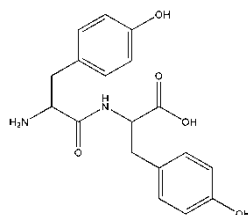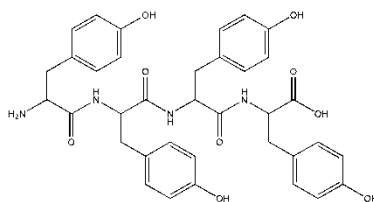


<sup>7</sup>FYCYF
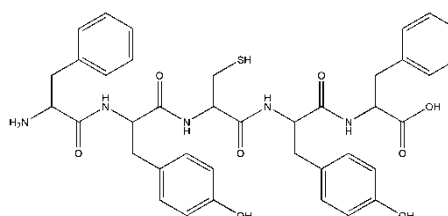


<sup>8</sup>FFCFF



\+
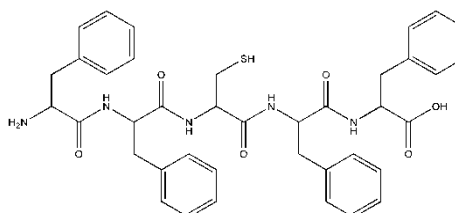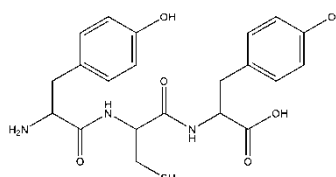
$^{10}$CYY
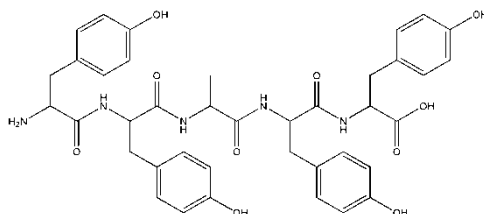


$^{11}$YY



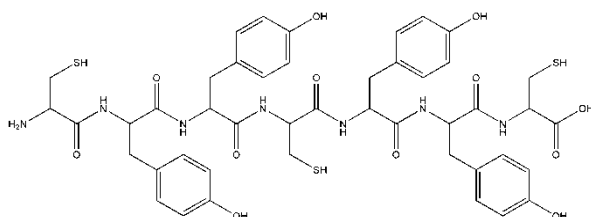$^{12}$YYY
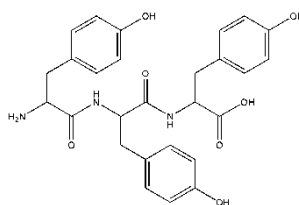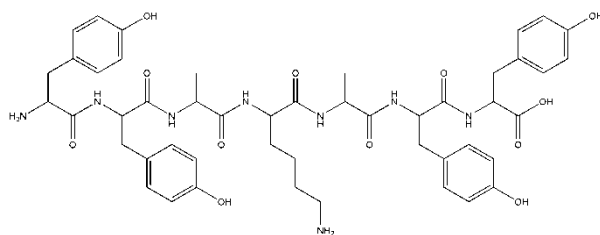


$^{13}$YYYY



$^{14}$YYAYY

# Appendix   2. The Structures of the Synthesized Peptides (Continued)
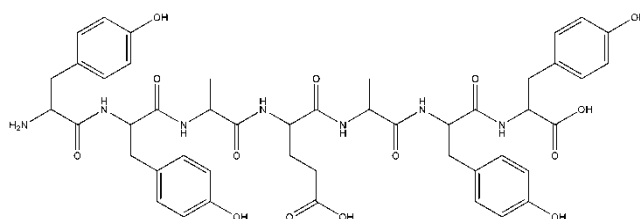


$^{15}$CYYCYYC



$^{16}$YYAKAYY



$^{17}$YYAEAYY

# 요 약

단백질과 펩타이드는 자기조립을 통해 다양한 3차원 구조체를 형성하며, 자연계에서 중요한 역할을 하고 있다. 최근에는 이런 단백질과 펩타이드 자기조립 성질을 이용하여 다양한 나노 또는 마이크로 구조체들을 형성시켜 각종 분야에 응용하려는 연구들이 진행되고 있다. 자연계에서 타이로신은 펩타이드 또는 단백질들을 가교시켜 기계적 물성을 증대시키는데 이용되고 있고, 광합성에서는 전자 전달체의 역할을 하고, 효소 시스템에서는 다양한 화학반응에 촉매로 이용되고 있다. 본 논문에서는 다양한 타이로신 함유 펩타이드 유도체들을 합성하였고, 이를 공기/물 계면에서 자기조립시켜 필름형태의 나노 구조체를 형성시키는 연구를 하였다. 그 중에서도 특히, 그동안 어렵다고 알려진 2차원 구조체를 형성시킬 수 있는 타이로신 기반의 펩타이드(YYCYY, YYACAYY)를 개발하였고, 물과 공기사이에서 자기조립시켜, 필름으로 성장하는 것을 확인하였다. 이렇게 형성된 타이로신 기반의 펩타이드 필름의 한장당 단위 두께는 1.4 나노미터로, 시간이 지남에 따라 필름 층들이 쌓여가며 두꺼운 필름으로 성장하는 것을 확인하였다. 또한 이러한 타이로신 기반 펩타이드들이 어떻게 대면적화 될 수 있는지에 대한 메커니즘을 TEM, AFM, XRD, FT-IR, CD, Raman, Mass Spectroscopy등의 다양한 분석 방법 및

컴퓨터 시뮬레이션을 통해 제시하였다. 즉, 펩타이드가 공기/물 계면에서 나선접힘을 통해 소수성기인 타이로신들이 한쪽에 몰리게되고, 친수성기인 시스테인기가 그 반대쪽에 위치함에 따라 양친매성 특성을 갖게 되어 물위로 떠오르게 됨을 확인하였다. 이후 용존산소에 의해 시스테인끼리의 디설파이드 결합을 이루어 펩타이드 이합체가 형성되고, 이러한 이합체들이 파이-파이 결합을 통해 자라나 한 면을 이루게 되고, 이러한 현상이 반복적으로 일어나 펩타이드 면들이 계속 쌓이게 되면서, 물의 표면장력을 이길만큼의 강한 필름(facet)이 형성되는 것을 확인할 수 있었다. 또한 이렇게 형성 된 타이로신 펩타이드 필름은 다양한 금속들(구리, 철, 팔라듐 등등)과 상호작용을 하여 타이로신 라디칼을 쉽게 형성시키며, 산화환원 반응을 용이하게 진행시켜주는 촉매 작용을 할 수 있음을 발견하였다. 즉, 물과 공기 사이 계면에서 형성된 타이로신 펩타이드 필름 위에서 전도성 고분자의 단량체로 잘 알려진 피롤이 폴리피롤 고분자 필름으로 계면에서 쉽게 중합됨을 확인하였다. 또한, 타이로신 펩타이드 필름 위에서는 금이나 팔라듐과 같은 금속이온들의 환원이 잘 일어나는 것도 확인할 수 있었다. 즉, YYACAYY 펩타이드에 팔라듐(II) 금속 이온을 함께 첨가하여 필름을 형성시키고, 그위에서 피롤을 중합해 본 결과, 펩타이드 필름-폴리피롤 표면에 팔라듐 나노입자들이 균일하게 고정화됨을 확인 할 수 있었다. 그리고 이렇게 타이로신 펩타이드-폴리피롤에 고정화된 팔라듐 나노입자(Tyr Peptide@PPy@Pd NP)를 이용하

여 물에서 Suzuki 반응을 일으킨 결과, 교차 짝지음 반응 촉매로서 매우 좋은 효율을 보이는 것을 확인하였다. 또한 그동안에 반응이 어렵다고 알려진 아릴클로라이드의 교차 짝지음 반응에서도 50도 물에서 매우 좋은 촉매 활성을 보임을 확인하였다. 이처럼 타이로신 펩타이드-폴리피롤에 고정화된 팔라듐 촉매는 반응성이 매우 우수하고 재사용이 가능하기 때문에 향후, 정밀화학 분야에 응용이 매우 클 것으로 기대된다.

# 감사의 글

　제 나이 35이라는 이르지 않은 나이에 학생이라는 신분을 뒤로하고 박사라는 신분으로 사회로 나아가게 되었습니다. 지금에 와서 학창시절을 돌이켜보면 참으로 많은 일들이 있었던 것 같습니다. 즐거웠던 기억들도 있고, 그 당시에는 힘들고 어려워서 포기하고 싶다고 생각되었던 일들도 많았지만, 지금은 그 힘들었던 일들을 모두 지나가고, 이겨 낼 수 있었기에 이제는 추억으로 그려집니다. 지금 다시 생각해보면 그럴때마다 제 주변에서 저를 도와주신 많은 분들이 계신 것 같습니다. 그분들로 인해 제가 지금의 자리에 서 있을 수 있었습니다.

　우선 매우 많이 부족한 저에게 늘 조언해주시고, 지도해주시면서 자신감을 심어주신 이윤식 교수님께 정말 감사의 말씀 드리고 싶습니다. 언제나 교수님의 교훈들을 잊지 않고 사회에 나아가 많은 기여를 할 수 있도록 노력하겠습니다. 그리고, 그 동안 많은 가르침을 주신 서울대학교 화학생물공학부 교수님들께도 감사드리고 싶습니다. 특히, 졸업하는 마지막까지 아낌없는 지도를 해주신, 남기태 교수님, 백승렬 교수님, 김병기 교수님, 이상엽 교수님께 정말 감사의 말씀 전하고 싶습니다.

　그리고 지금의 유기합성 실험실을 있게 해주신 많은 선배님들과 후배님들 그리고 동기 및 동문님들에게도 감사의 말씀 전하며, 언제나 하시는 일들 모두 잘 되시길 바라겠습니다. 그 동안 실험실에서 정말 행복했고, 앞으로도 제가 필요한 자리라면 언제든지 달려가도록 하겠습니다.

　또한 제가 쓰러지려 할 때마다 옆에서 끌어주고 일으켜 주며 지금도 제 옆을 든든히 지켜주는 친구들과 대학, 대학원 동문들에게도 감사의 말씀 드리겠습니다. 하시는 일들 모두 잘 되실 거라 확신합니다.

그리고, 지금까지 저를 믿고, 아낌없이 후원해주신 아버지 어머니, 지원이, 할머니 두 분과 고인이 되신 할아버지 두분 및 모든 일가 친척들, 박사학위 중에 새로운 가족이 된 희영이, 장인어른, 장모님, 큰처남, 그리고 현재 두 명의 아이들 윤아, 지금 뱃속의 아기에게도 모두 감사의 말씀 드립니다. 힘들때나 즐거울때나 늘 함께 있었고, 언제나 가족들로 인해 힘과 용기를 가질 수 있었습니다. 특히 저를 이 자리에 있게 해주신 나의 아버지 고 장윤호 박사님, 당신이 있기에 제가 있고, 당신 때문에 행복했습니다. 언제 다시 이 보답을 할 수 있을지 모르겠지만, 너무 감사했고, 너무 자랑스럽고, 다시 만날 날을 기약하도록 하겠습니다. 그리고 지금의 우리 가족들이 언제나 행복했으면 하는 것이 제 작은 바램입니다. 앞으로도 제가 성장하는 모습 지켜봐 주시길 바라겠습니다. 제 이름 장형석이라는 큰 뜻이 부끄럽지 않도록 하겠습니다.

이 분들뿐만 아니라 저를 도와주신 많은 분들에게도 진심으로 감사의 말씀 드리겠습니다. 항상 건강하시고, 행복하시며, 하느님의 사랑이 함께 하시길 바라겠습니다.

마지막으로 하나뿐이신 여호와 하느님께 이 모든 영광을 돌리며 이 논문을 마치겠습니다.

감사합니다.

2013년 7월 31일

장형석 올림-